

NORSAR

ROYAL NORWEGIAN COUNCIL FOR SCIENTIFIC AND INDUSTRIAL RESEARCH

NORSAR Scientific Report No. 1-85/86

FINAL TECHNICAL SUMMARY

1 April - 30 September 1985

L. B. Loughran (ed.)

Kjeller, December 1985



APPROVED FOR PUBLIC RELEASE, DISTRIBUTION UNLIMITED



~~UNCLASSIFIED~~
SECURITY CLASSIFICATION OF THIS PAGE

REPORT DOCUMENTATION PAGE

1a. REPORT SECURITY CLASSIFICATION UNCLASSIFIED		1b. RESTRICTIVE MARKINGS NOT APPLICABLE		
2a. SECURITY CLASSIFICATION AUTHORITY NOT APPLICABLE		3. DISTRIBUTION/AVAILABILITY OF REPORT APPROVED FOR PUBLIC RELEASE DISTRIBUTION UNLIMITED		
2b. DECLASSIFICATION/DOWNGRADING SCHEDULE NOT APPLICABLE				
4. PERFORMING ORGANIZATION REPORT NUMBER(S) SCIENTIFIC REPORT 1-85/86		5. MONITORING ORGANIZATION REPORT NUMBER(S) SCIENTIFIC REPORT 1-85/86		
6a. NAME OF PERFORMING ORGANIZATION NTNF/NORSAR	6b. OFFICE SYMBOL <i>(If applicable)</i>	7a. NAME OF MONITORING ORGANIZATION HQ AFTAC/TGX		
6c. ADDRESS (City, State and ZIP Code) POST BOX 51 N-2007 KJELLER, NORWAY		7b. ADDRESS (City, State and ZIP Code) PATRICK AFB, FL 32925-6471		
8a. NAME OF FUNDING/SPONSORING ORGANIZATION DEFENSE ADVANCED RESEARCH PROJECTS AGENCY	8b. OFFICE SYMBOL <i>(If applicable)</i>	9. PROCUREMENT INSTRUMENT IDENTIFICATION NUMBER CONTRACT NO. F08606-84-C-0002-P00002		
8c. ADDRESS (City, State and ZIP Code) ARLINGTON, VA 22209		10. SOURCE OF FUNDING NOS.		
		PROGRAM ELEMENT NO. R&D	PROJECT NO. NORSAR PHASE 3	TASK NO. SOW TASK 5.0
11. TITLE (Include Security Classification) FINAL TECHNICAL SUMMARY 1 APR-30 SEP 85 (UNCLASSIFIED)				
12. PERSONAL AUTHOR(S) L.B. LOUGHRAN (ED.)				
13a. TYPE OF REPORT SCIENTIFIC SUMMARY	13b. TIME COVERED FROM 1 APR 85 TO 30 SEP 85	14. DATE OF REPORT (Yr., Mo., Day) DEC 85	15. PAGE COUNT 132	
16. SUPPLEMENTARY NOTATION NOT APPLICABLE				
17. COSATI CODES		18. SUBJECT TERMS (Continue on reverse if necessary and identify by block number) NORSAR, NORWEGIAN SEISMIC ARRAY		
FIELD	GROUP			SUB. GR.
19. ABSTRACT (Continue on reverse if necessary and identify by block number) This Final Technical Report describes the operation, maintenance and research activities at the Norwegian Seismic Array (NORSAR) for the period 1 April - 30 September 1985. It supplements the three Semiannual Technical Summaries previously submitted during the contract period, which has covered 1 October 1983 - 30 September 1985.				
20. DISTRIBUTION/AVAILABILITY OF ABSTRACT UNCLASSIFIED/UNLIMITED <input checked="" type="checkbox"/> SAME AS RPT. <input type="checkbox"/> DTIC USERS <input type="checkbox"/>		21. ABSTRACT SECURITY CLASSIFICATION UNCLASSIFIED		
22a. NAME OF RESPONSIBLE INDIVIDUAL CAPT JAMES A. ROBB		22b. TELEPHONE NUMBER <i>(Include Area Code)</i> ((305) 494-7665	22c. OFFICE SYMBOL AFTAC/TGX	

(continued next page)

UNCLASSIFIED

19. (cont.)

The NORSAR Detection Processing system has been operated through the period 1 April - 30 September 1985 with an average uptime of 98.2 per cent. Most of the downtime has been caused by disk failure at the central recording computer. A total of 2133 seismic events have been reported by NORSAR in the period. The performance of the continuous alarm system and the automatic bulletin transfer by telex to AFTAC have been satisfactory. After a redesign of the system, all detection and event processing is now conducted on one single IBM 4341 computer, which has allowed for more efficient and flexible operation.

Using a data base of about 170 NORSAR-recorded seismic events at regional distances during the past 15 years, a detailed map of propagation characteristics of short period regional seismic phases has been compiled. Lg shows efficient propagation out to about 20 degrees at 1 Hz and 10 degrees at 4 Hz over continental shield paths (e.g., to the east of the array), whereas Sn is the dominant secondary phase for paths that cross significant tectonic features like graben structures and continental margins. The relative amplitudes of P, Sn and Lg are strongly frequency dependent; thus Lg is relatively strong at low frequencies (around 1 Hz), whereas both P and Sn have higher dominant frequencies.

The NORESS on-line detection and location performance have been evaluated both for regional and teleseismic events. A case study of 132 Western Norway/North Sea events (mainly in the distance range 300-600 km) has indicated a detection threshold of M_L 1.5-2.0 for NORESS. The NORESS epicentral solutions are in most cases consistent with those provided by the Western Norway seismic network. For one site where a large number of known explosions (36) were processed, the average NORESS location error was 10 km. Occasional larger errors are due to problems in the automatic phase determination at NORESS (e.g., Pg identified as Pn, Sn identified as Lg).

A statistical study of NORESS detections during April-September 1985 (excluding time periods with transmission line problems) has shown an average of about 100 detections per day, of which about 20 per cent are teleseismic P phases, about 25 per cent regional P phases and the remaining 55 per cent have slow phase velocities (< 6 km/s) corresponding to secondary phases or possibly noise detections. Most of the regional phases are detected during local day time, and correspond to quarry blasts and other local explosions. The majority of P phases are detected using conventional beams, whereas incoherent (envelope) beams are very efficient in detecting secondary phases.

A comparison of NORESS and NORSAR has shown that, for the six-month period April-September 1985, NORESS detected 84.5 per cent of the teleseismic events reported in the NORSAR monthly bulletin (only days when both systems were operational were considered). The excellent teleseismic capability of NORESS is further confirmed by many P-phases detected at NORESS but not reported by NORSAR. NORESS estimates of

UNCLASSIFIED

UNCLASSIFIED

19. (cont.)

phase velocities and azimuths are, however, not as accurate as those provided by NORSAR. The median differences in NORSAR-NORESS estimated azimuth is 12 degrees (based on 1376 common events), which, based on comparisons with PDE solutions, is mainly attributed to uncertainty in the NORESS estimates.

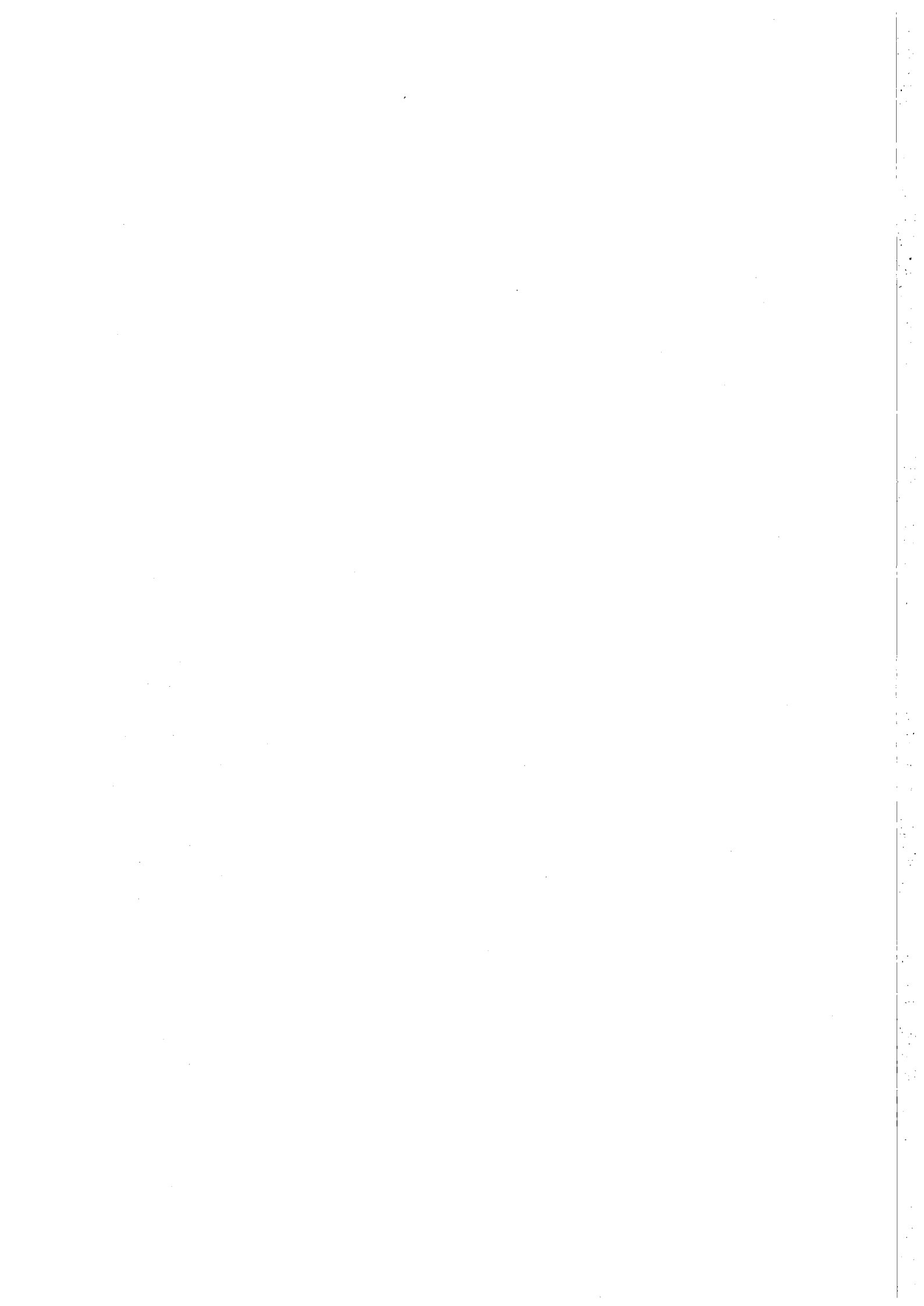
A study of P-wave spectra recorded at NORESS has been initiated. For intermediate and low magnitude Eurasian explosions signal energy well above the noise level can be observed for frequencies up to about 10 Hz, even at teleseismic distances. For detection purposes, the SNR (at the single-sensor level) is usually best in the 2-4 Hz band, and the beam SNR is further improved by selecting appropriate sub-geometries of NORESS for beamforming.

An efficient method for the calculation of ellipticity corrections has been developed, and the calculations compare well to results published elsewhere. Attenuation of seismic energy from local events in southern Norway has been studied using the coda decay method as well as spectral ratios. The Q values are found to be comparable to values published for the Canadian Shield at high frequencies (12-15 Hz), but are more strongly frequency dependent than Canadian Shield values.

Various signal analysis schemes (three-component analysis, f-k analysis and semblance) have been tested on NORESS data from a presumed explosion in Western Russia and have been found to produce consistent and reasonable results for the P wavetrain. The f-k method has the advantage of providing efficient scanning of the whole wavefield space. The semblance technique is very robust, but requires a priori information on azimuth for easy use in an automated mode. 3-component results are also rather stable when based on beam traces from 4 stations.

A study of P-wave coda scattering using NORSAR and NORESS data has indicated sources of Pg scattering mainly to the north and east, with a clustering that appears to coincide roughly with major tectonic boundaries. For Pn similar results are found, but the scattering sources appear to be more dispersed in this case.

UNCLASSIFIED



AFTAC Project Authorization : T/4141/B/PMP
ARPA Order No. : 4138
Program Code No. : OF10
Name of Contractor : Royal Norwegian Council
for Scientific and
Industrial Research
Effective Date of Contract : 1 October 1983
Contract Expiration Date : 30 September 1985
Project Manager : Frode Ringdal (02) 71 69 15
Title of Work : The Norwegian Seismic Array
(NORSAR) Phase 3
Amount of Contract : \$ 1,469,447.69
Contract Period Covered by the Report : 1 Apr - 30 Sep 1985

The views and conclusions contained in this document are those of the authors and should not be interpreted as necessarily representing the official policies, either expressed or implied, of the Defense Research Projects Agency, the Air Force Technical Applications Center or the U.S. Government.

This research was supported by the Advanced Research Projects Agency of the Department of Defense and was monitored by AFTAC, Patrick AFB, FL 32925, under contract no. F08606-84-C-0002-P00002.

NORSAR Contribution No. 362

TABLE OF CONTENTS

	<u>Page</u>
I. SUMMARY	1
II. OPERATION OF ALL SYSTEMS	3
II.1 Detection Processor operation	3
II.2 Array communication	8
III. ARRAY PERFORMANCE	12
IV. IMPROVEMENTS AND MODIFICATIONS	13
V. MAINTENANCE ACTIVITIES	16
V.1 Activities in the field and at the Maintenance Center	16
V.2 Improvements and modifications	18
V.3 Array status	19
VI. DOCUMENTATION DEVELOPED	20
VII. SUMMARY OF TECHNICAL REPORTS/PAPERS PREPARED	21
VII.1 Propagation characteristics of regional phases recorded at NORSAR	21
VII.2 Evaluation of NORESS real time processing performance: Case study for 132 Western Norway/ North Sea events	30
VII.3 Initial results from NORESS detection processing	40
VII.4 NORESS-NORSAR processing system comparison	52
VII.5 P-wave spectra from NORESS recordings	62
VII.6 The calculation of ellipticity corrections	72
VII.7 Attenuation of seismic energy from local events in southern Norway	76
VII.8 A new technique for 3-component seismogram analysis	86
VII.9 NORESS regional event records - wavefield decomposition schemes	98
VII.10 P-wave coda -- scattering research	119
APPENDIX A: NORESS data tape format	123



I. SUMMARY

This Final Technical Report describes the operation, maintenance and research activities at the Norwegian Seismic Array (NORSAR) for the period 1 April - 30 September 1985. It supplements the three Semiannual Technical Summaries previously submitted during the contract period, which has covered 1 October 1983 - 30 September 1985.

The uptime of the NORSAR online detection processor system has averaged 98.2 per cent, during April-September 1985, which is the same as for the previous half-year period. Disk problems in August contributed strongly to a downtime of 4.4%. The array communications system for 02C has been frequently affected during the period, and subarrays 02B, 03C and 04C also occasionally showed high error figures. Subarray 06C resumed operation in July and now has an acceptable performance. A total of 2133 events were reported in this period, giving a daily average of 11.7 events.

During this period the system design has been changed, so that the entire system including data acquisition, detection processing, event processing and plotting is now performed by only one IBM 4341 computer. This change will facilitate both operation and maintenance in the future.

Much of the field staff's work during April and May concerned preparations for the official NORESS opening, which took place in June. During the months of July-September the field maintenance center was moved from Stange to Hamar. In the reporting period, field maintenance work was divided fairly evenly between NORSAR and NORESS.

The research activity is summarized in section VII. Section VII.1 discusses propagation characteristics of regional phases recorded at NORSAR. Section VII.2 contains an evaluation of NORESS real time processing performance with a discussion of a case study for 132 Western Norway/ North Sea events. Section VII.3 presents the initial results from NORESS detection processing, while Section VII.4 contains a comparison of the NORESS and NORSAR processing systems. Section VII.5 presents a study of P-wave spectra from NORESS recordings. Section VII.6 presents a computational

method for the calculation of ellipticity corrections. Section VII.7 presents a study of the attenuation of seismic energy from local events in southern Norway. In section VII.8 a new technique for 3-component seismogram analysis is presented, while Section VII.9 discusses wavefield decomposition schemes based on NORESS regional event records. Section VII.10 contains a discussion of the on-going efforts to determine the nature of the teleseismic P coda seen on short period seismograms.

II. OPERATION OF ALL SYSTEMS

II.1 Detection Processor (DP) Operation

There have been 92 breaks in the otherwise continuous operation of the NORSAR online system within the current 6-month reporting interval. The uptime percentage for the period is 98.2, which is the same as for the previous half-year period.

Fig. II.1.1 and the accompanying Table II.1.1 both show the daily DP downtime for the days between 1 April and 30 September 1985. The monthly recording times and percentages are given in Table II.1.2.

The breaks are grouped as follows:

a)	Computer hardware failure	11
b)	Stops related to programming work or error	6
c)	Hardware maintenance stops	27
d)	Power merges and power breaks	6
e)	TOD correction	29
f)	Communication line failures	13

The total downtime for the period was 77 hours and 44 minutes. The mean-time-between-failure (MTBF) was 2.0 days, as compared to 1.4 for the previous period.

J. Torstveit

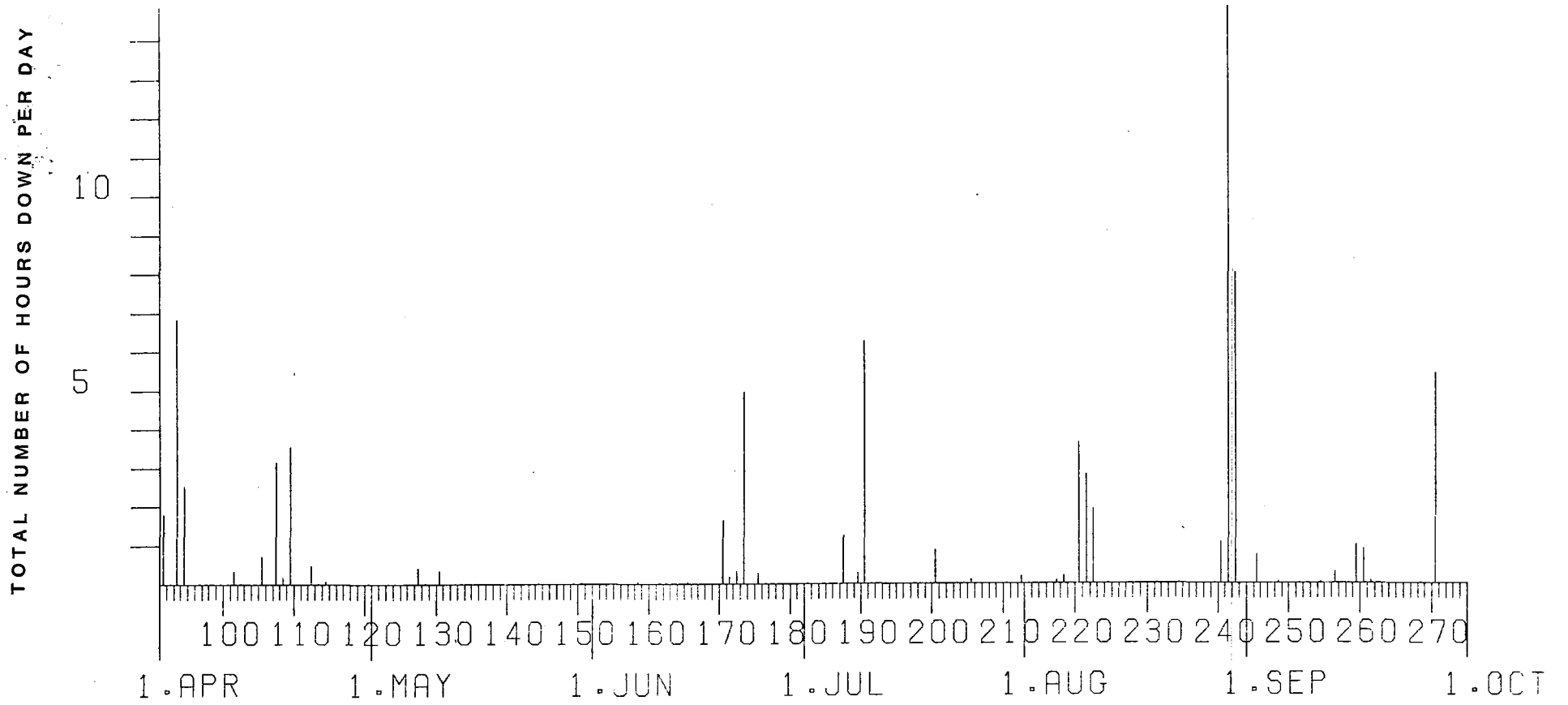


Fig. II.1.1 Detection Processor downtime in the period 1 April - 30 September 1985.

LIST OF BREAKS IN DP PROCESSING THE LAST HALF-YEAR

DAY	START	STJP	COMMENTS.....	DAY	START	STJP	COMMENTS.....				
91	11	28	12	3	DISK SERVICE	161	9	53	9	54	LINE FAILURE
91	12	12	13	24	DISK SERVICE	162	6	1	6	2	TOD RETARED 25MS
92	6	1	6	2	TOD RETARED 24MS	165	6	1	6	3	TOD RETARED 27MS
93	9	6	15	55	DISK SERVICE	170	6	34	6	52	DATA LOST IN COPYING
94	3	35	8	52	DISK SERVICE	170	16	54	18	13	DISK CONTROLLER
94	9	11	11	25	DISK SERVICE	171	12	54	12	59	LINE FAILURE
101	12	25	12	45	LINE FAILURE	171	12	54	12	59	LINE FAILURE
102	7	55	7	56	TOD RETADED 20MS	172	6	1	6	2	TOD RETARED 25MS
105	10	13	10	55	CPU SERVICE	172	13	25	13	43	POWER BREAK
107	6	1	6	2	TOD RETARED 20MS	173	4	34	7	35	POWER BREAK
107	6	7	6	8	TOD RETARED 10MS	173	10	9	12	3	POWER BREAK
107	7	22	8	44	DISK TEST	175	7	23	7	24	LINE FAILURE
107	9	5	10	44	DISK TEST	175	12	42	12	57	POWER BREAK
107	13	12	13	18	DISK TEST	182	10	31	10	32	TOD CORR. 1 LEAP SEC
108	9	17	9	22	DISK TEST	187	12	2	13	15	DISC CONTR. FAILURE
108	11	55	12	0	DISK TEST	189	23	44	24	0	POWER FAILURE
109	7	33	7	39	DISK TEST	190	0	0	6	13	POWER FAILURE
109	19	57	23	22	DISK FAILURE	190	6	51	6	52	TOD RETARED 150MS
112	6	11	6	15	DISK FAILURE	193	6	15	6	15	TOD RETARED 120MS
112	8	39	8	59	DISK FAILURE	197	12	0	12	1	TOD RETARED 76MS
112	10	49	10	53	DISK FAILURE	200	22	17	23	9	POWER FAILURE
113	6	1	6	2	TOD RETARED 25MS	203	7	53	7	54	LINE FAILURE
114	6	33	6	38	DISK SERVICE	204	6	2	6	3	TOD RETARED 35MS
120	6	1	6	2	TOD RETARED 45MS	205	6	30	6	34	LINE FAILURE
127	11	7	11	31	MEXOREX SERVICE 3496	205	10	53	10	54	LINE FAILURE
128	12	56	12	57	TOD RETARED 25MS	205	11	19	11	20	LINE FAILURE
130	10	13	10	17	DISK SERVICE	210	8	24	8	25	TOD RETARED 25MS
130	12	50	13	4	DISK SERVICE	212	7	4	7	14	LINE FAILURE
130	13	23	13	26	DISK SERVICE	217	6	1	6	5	TOD RETARED 25MS
133	7	26	7	27	TOD RETARED 25MS	218	11	55	12	7	SYSTEM WORK
134	13	14	13	15	LINE FAILURE	220	9	9	12	46	SYSTEM WORK
140	9	29	9	30	TOD RETARED 30MS	221	7	25	10	13	SYSTEM WORK
144	10	56	10	57	TOD RETARED 30MS	222	13	27	15	20	SYSTEM WORK
150	6	2	6	3	TOD RETARED 15MS	222	15	33	15	34	SYSTEM WORK
155	7	13	7	14	TOD RETARED 25MS	224	6	56	6	57	TOD RETARED 32MS
158	7	12	7	14	LINE FAILURE	231	6	42	6	43	TOD RETARED 32MS

1
5
1

Fig. II.1.1 Daily DP downtime in the period 1 April - 30 September 1985.
(Page 1 of 2)

LIST OF BREAKS IN DP PROCESSING THE LAST HALF-YEAR

DAY	START	STOP	COMMENTS.....
234	11 22	11 23	TOD RETARED 25MS
239	5 53	5 54	TOD RETARED 20MS
240	12 39	13 41	DISK SERVICE
240	13 47	13 48	DISK SERVICE
241	9 8	24 0	DISK FAILURE
242	0 0	6 3	DISK FAILURE
242	21 0	22 57	DISK FAILURE
245	6 35	6 41	LINE FAILURE
245	7 55	8 33	DISC SERVICE
248	6 1	6 3	TOD RETARED 44MS
252	7 0	7 1	LINE FAILURE
254	11 14	11 15	TOD RETARED 44MS
255	8 59	9 15	DISC CONT. FAILURE
259	7 25	7 28	DISC CONT. SERVICE
259	13 12	13 15	DISC CONT. SERVICE
259	23 8	24 0	DISC CONT. FAILURE
260	0 0	0 48	DISC CONT. FAILURE
260	10 33	10 35	DISC CONT. SERVICE
260	12 32	12 35	DISC CONT. SERVICE
261	11 38	11 39	DISC CONT. SERVICE
261	12 17	12 19	DISC CONT. SERVICE
262	6 1	6 2	TOD RETARED 26MS
268	6 35	6 35	LINE FAILURE
270	8 18	13 44	SERVICE MODCOMP

Table II.1.1 (cont.)

Month	DP uptime hours	DP uptime %	No. of DP breaks	No. of days with breaks	DP MTBF* (days)
APR	700.40	97.3	24	14	1.2
MAY	743.15	99.9	10	8	2.8
JUN	712.67	99.0	14	10	2.0
JUL	735.05	98.8	14	12	2.0
AUG	711.42	95.6	14	12	2.0
SEP	711.58	98.8	92	11	1.7
		98.2	92	67	2.0

* Mean-time-between-failures = total uptime/no. of up intervals.

Table II.1.2 Online system performance, 1 April - 30 September 1985.

II.2 Array communications

Table II.2.1 reflects the performance of the system throughout the reporting period. With reference to the table we can see that 02C has been frequently affected. 02B, 03C and 04C also occasionally showed high error figures.

06C resumed operation 12 July after having been connected to the PCM system between Rokosjøen telephone central and Hamar, and now has an acceptable performance.

Most the irregularities have been caused by faulty and/or damaged cables (02B, 02C, 03C, 04C), changes and/or expansion/reconfiguration at telestations (Lillehammer/02C), lightning (especially exposed 04C, 06C), Modcomp problems during resynchronizing sequences (especially when in connection with deteriorated line(s)), and power outages (04C).

Summary

- Apr 85 02C affected in connection with reconfiguration/
expansion at NTA/Lillehammer (between 1 and 12 Apr)
04C was down due to a bad communication line (9-12 Apr).
06C comm. system still experiencing problems.
In a letter to NTA, NORSAR recommended reconnection
to original line between Hamar and 06C.
- May 85 This was a relatively good period in spite of 02C out-
ages of 25%.
An attempt to strap the 06C NOKIA modems to external
synchronization did not improve the performance of that

subarray. In internal synchronization, spikes created unacceptable conditions.

Jun 85 Subarrays 01A, 01B, 02B and 03C nearly error free as they were in the previous two months.

02C was down 3,4-6,7 and 8-10 June, last outage 12 June.

04C was affected between 3 and 4 June as we were not able to resynchronize the system.

06C was still out of operation, awaiting reconnection to the original line.

Jul 85 Only three subarrays were nearly free from errors: 01A-02B.

02C-04C had high error figures.

06C was reconnected to the original line 12 July, after which remarkable improvement was observed.

The error source which caused the varying 02C performance was not stated by NTA this period; a bad connection or an intermittently operating item may have caused the frequent outages. Week 29 NTA technicians visited the CTV and were able to reinstate normal operation.

A faulty cable between Osmoen and the subarray 03C caused reduced performance (week 31).

Lightning caused power problem (week 28) at 04C.

Aug 85 In August NTA/Hamar started to repair a cable near Mesnalien, which also contained the 02C comm. cable. Almost simultaneously the same cable was damaged two other places, one was located near the CTV. This situation created, of course, special problems and

delayed the termination of the splicing job.

03C was down two-thirds of week 32, due to a cable of reduced quality; part of it was replaced.

02B was affected week 35, probably caused by a mistake by NTA/Hamar.

Lightning caused 04C isolation transformer damage 13 August, and consequently loss of power. Transformer was replaced 21 August and the subarray resumed operation.

Besides, synchronization problems affected the comm. system performance for 02C-06C.

In order to establish normal conditions it was necessary to stop and restart the communication machine (Modcomp) and/or manipulate isolation switches between the modems and the comm. machine, specially week 35. Such problems may arise in cases where the comm. machine is heavily loaded and tries to synchronize a comm. line with reduced quality.

Sep 85 Communication systems specially affected in September were 02B, 03C and 04C.

Subarray 02B lost power 29 September and remained inoperational the rest of the month.

03C was down between 2 and 6 September. In the same period 04C caused heavy Modcomp load (repeated resynchronization attempts) due to a cable fault near the CTV causing gradually reduced performance.

06C was also affected by synchronization problems (2 September).

O.A. Hansen

Sub- array	APR 85 (4) (1-28.4)	MAY 85 (5) (29.4-2.6)	JUN 85 (4) (3-30.6)	JUL 85 (5) (1.7-4.8)	AUG 85 (4) (5.8-1.9)	SEP 85 (4) (2-29.9)	Average $\frac{1}{2}$ yr
01A	0.004	0.002	0.003	0.005	0.003	0.008	0.004
01B	0.001	0.001	0.004	0.005	0.019	0.014	0.007
02B	0.003	0.001	0.008	0.005	*13.64	*21.45	5.85
02C	*25.45	*25.02	*7.19	*32.29	*11.62	0.024	16.93
03C	0.03	0.001	0.005	*15.75	*17.87	*16.53	8.36
04C	*42.80	*1.43	*6.25	*6.80	*14.52	*26.44	16.38
06C	*59.97	*100.0	*100.0	*18.99	*11.23	0.94	48.52
AVER	18.33	18.07	16.20	10.55	9.84	9.34	13.72
	02C,04C	02C,06C	02C,04C	02C-06C	02B-06c	02B,03C	02B-06C
Less	06C		06C			04C	
	0.010	0.21	0.005	0.002	0.011	0.246	0.006

* see item II.2 regarding figures with asterisks

Table II.2.1 Communications performance. Figures in per cent based on total transmitted frames/week (1 Apr - 30 Sep 1985).

III. ARRAY PERFORMANCE

III.1 Event Processor Operation

In Table III.1 some monthly statistics of the Event Processor operation are given:

	Teleseismic	Core Phases	Sum	Daily
APR 85	257	52	309	10.3
MAY 85	242	55	297	9.6
JUN 85	324	68	392	13.1
JUL 85	333	72	405	13.1
AUG 85	341	46	387	12.5
SEP 85	258	85	343	11.4
	1755	378	2133	11.7

Table III.1 Event Processor Statistics, April - September 1985.

B. Paulsen

IV. IMPROVEMENTS AND MODIFICATIONS

NORSAR on-line system using 4341 and MODCOMP Classic

We refer to the detection processor operation statistics for detailed information about uptime, communication and processing performance.

Processing system:

The NORSAR online system has previously been using two computers to do detection processing, generate event bulletins and plot events. The system design has now been changed so that everything from data acquisition to event plotting is achieved using only one IBM 4341 computer. It is easier for us to both maintain and operate the system when only one computer is involved.

The following functions are implemented on the NORSAR on-line computer:

Functions	Program
Communication with MODCOMP	(DPCOM)
Detection processing and storing of data	(DPDAQ)
Event processing, plotting	(DPEP)
Automatic preparation of bulletins	(AFTAC)

The computer used for these functions is an IBM Model 4341 L01. The average system load is about 28%. Thus, there is still computing power left even with the current full operation for implementing new processing algorithms.

Data from 06C

The 06C subarray, which for several years was used in experimental configurations related to NORESS developments, has now been reestablished in its original configuration, as part of the standard NORSAR array.

Data quality

From time to time we have communication line problems which give us a significant number of false detections. In the automatic bulletin transferred to AFTAC by telex, the number of DPX entries during such periods is very large. Also the automatic event lists (EPX) are affected, since the current processing system is not able to mask all such occurrences. We are working on improvements in regard to this problem.

ARPANET

The upgrade of our ARPANET connection is planned for completion during November 85. Our experience using ARPANET for NORESS bulletin transfer to the CSS is very good and will be even more flexible when the planned ARPANET host connection is established.

NORESS

A significant part of our research under the AFTAC contract is connected to studies of regional seismic phases, using data from the new NORESS array.

Appendix A gives a format description of NORESS data tapes. NORESS data are recorded 24 hours a day and all data are stored permanently. Data from NORESS are available from NORSAR on request.

R. Paulsen

V. MAINTENANCE ACTIVITIES

V.1 Activities in the field and at the Maintenance Center

Visits to the NORSAR array were in May and June limited to actions with high priority, as the preparations for the official opening of the NORESS array 3 June needed all resources available at the NMC.

In July, August and September normal maintenance work was resumed.

A great deal of time was also spent on planning/preparations in connection with moving to the new maintenance center in Hamar.

SP and LP instruments have routinely been remotely monitored from NDPC and LP seismometers adjusted whenever needed.

A summary of the activities performed during the period is given in Table V.1. For completeness, we list activities carried out at both the NORSAR and NORESS sites.

<u>Subarray/ area</u>	<u>Task</u>	<u>Date</u>
NORESS	A satellite transmitter amplifier (TWT) failed and was replaced immediately.	24 April
02C	An attempt to replace an RA-5 SP01 failed due to bad weather conditions.	25 April

Subarray/ area	Task	Date
NORESS/ NMC	In May and June most time was spent on pre- parations and planning in connection with the NORESS official opening 3 June and the move to the new NORSAR maintenance center in Hamar. Also in June the NMC staff assisted Sandia representatives in modifying equipment at the earth station (4-27).	May/June
NORESS	10 channels in the NORESS array were out of operation a few hours due to a short circuit in a junction box which was repaired by the NMC staff.	8 July
NORESS	NORESS earth station was down approx. 6 hours due to a high voltage transformer damaged by lightning. The NMC staff was engaged in getting the station operational again.	15 July
NORESS	Lightning caused power trouble and NMC engagement. The station was down for about 2 hours and 15 minutes.	23 July
NORESS	In connection with installation of new switches on High Voltage Transformer (31 July) the station was down for about 2 hours. NMC took part in the work.	31 July
06C	NMC staff collected former 06C experimental vaults and brought them to the center station.	July
01B	Visited and replaced RA-5 amplifier SP02,05. Also localized faulty cable (common for SP01, 05), and in addition a broken cable to SP02. Both cable faults caused by lightning.	5 August
01B	Repairs and cable splicing.	19,20,21 & 26 August
02C	Replaced both Remote Centering Devices on EW seismometer (LP). Bad comm. line localized.	13 August 14 August
03C	Replaced FP Remote Centering Device on Vertical and NS seismometers (LP).	14 August

Subarray/ area	Task	Date
04C	Power isolation transformer (NORSAR property) was damaged by lightning. NMC spent three days on this job (incl. demounting ex. 05C) and transport.	August
NORESS	NORESS central station was visited in connection with analyses of the A ₀ HF-channel spectrum.	August
02B (Telem.)	All 02B (Telemetry) stations have been visited, batteries and seismometer cables have been replaced.	September
NMC	Engagements in September have been concentrated on preparing equipment for a new experimental small array.	September

Table V.1 Activities in the field and at the NORSAR Maintenance Center, April - September 1985.

V.2 Improvements and modifications

No NORSAR equipment modification was carried out during the reporting period.

V.3 Array status

As of 30 September 1985 the following channels deviated from tolerances:

04C 01, 02, 03, 06 and 07

06C 03, 08

01A 01 8 Hz filter

02 8 Hz filter

04 Attenuated 30 dB.

Note that the deviations for 01A do not reflect errors, as these channels are used experimentally. The deviations at 04C and 06C will be corrected.

O.A. Hansen

VI. DOCUMENTATION DEVELOPED

Kennett, B.L.N. & S. Mykkeltveit (1984): Guided wave propagation in laterally varying media: II - Lg waves in northwestern Europe, Geophys. J.R. Astr. Soc., 79, 257-267

Kennett, B.L.N., S. Gregersen, S. Mykkeltveit & R. Newmark (1985): Mapping of crustal heterogeneity in the North Sea Basin via the propagation of Lg waves, Geophys. J.R. Astr. Soc., 83, 299-306

Loughran, L.B. (ed.): Semiannual Technical Summary, Oct 84 - Mar 85, NTN/NORSAR, Kjeller, Norway

Wessel, P. & E.S. Husebye (1985): The Oslo graben gravity high and taphrogenesis, submitted for publication

L.B. Loughran

VII. SUMMARY OF TECHNICAL REPORTS/PAPERS PREPARED

VII.1 Propagation characteristics of regional phases recorded at NORSAR

About 170 regional events recorded at NORSAR during the period 1971-1985 have been analyzed with respect to propagation characteristics for the phases Sn and Lg in particular. The motivation for our study was to obtain calibration data for the real time processing of data recorded on the new NORESS array. In addition, it is expected that such a study will shed some light on the general relationship between characteristics of regional seismic phases and large-scale geological features.

The event location algorithm of the current version of the NORESS online processing package (RONAPP) is based on the assumption that the largest secondary phase detected is Lg, propagating at a group velocity of 3.5 km/s. This assumption is valid for many propagation paths to regional distance from the NORSAR and NORESS arrays. There are, however, notable exceptions to this simplified picture, as illustrated in Fig. VII.1.1.

Data analysis procedure

For the 170 events in the data base, event files of appropriate lengths to include all phases of interest were copied from the tape archive. In order to minimize possible effects from the geology near the receiver site, the analysis was carried out on data from the same seismic channel (02B01) for nearly all events. Fig. VII.1.2 shows an example of the output resulting from the processing of events in our data base. The seismograms in this figure are shown for unfiltered data (top) and three band-pass filters. We needed criteria for picking phase onsets, which are independent of the human analyst's personal judgement. To this end, we computed and plotted the logarithm of the STA/LTA-ratio

for each trace. The STA/LTA-algorithm used here for a single sensor is equivalent to the one used in the detection procedure in the RONAPP processing package, where STA/LTA is computed for a number of beams. In this manner, our analysis ties in with the current automatic processing of NORESS data. For this study, we specified an STA/LTA threshold of 3.0 for acceptance of a signal as a true phase arrival. This level would correspond to a somewhat higher (and operationally acceptable) detection threshold for the real time array processing, due to the SNR gain offered by the array beamforming.

Now, our analysis procedure has been to go through 170 plots of the kind shown in Fig. VII.1.2 and characterize the arrivals in the S wavetrain for each of the three filter bands. The case of dominant Lg (over Sn) was subdivided into three different codes as follows:

- (1) Only Lg can be seen in the S wavetrain.
- (2) Lg is the dominating phase, but Sn can be discerned.
- (3) Lg is still the dominating phase, but Sn is not very much smaller.

An equivalent subdivision, also on a three-point scale, was adopted for the case of dominant Sn. Finally, a code was assigned to the case of comparable Lg and Sn amplitudes. Phases with corresponding group velocities in the interval 3.80-4.70 km/s were classified as Sn, with Lg corresponding to group velocities in the range 3.30-3.80 km/s.

Analysis results -- source area mapping

Fig. VII.1.3 shows the results derived from analysis of the data in our data base. In this figure, we assign the character of the S wavetrain as observed in the NORSAR seismometer record, to the

source area. We have confined ourselves to the use of three codes only in this figure -- corresponding to (1) dominant Lg, (2) comparable Lg and Sn and (3) dominant Sn. Areas with no events or for which the available data were inconclusive with respect to appropriate characterization of the S wavetrain appear unshaded in the figure. Color-coded maps including all 7 codes defined above have also been prepared. These maps offer more details and often show gradual transitions from dominating Lg to dominating Sn in certain directions. Several conclusions can be drawn from Fig. VII.1.3:

- For an area covering almost all of Norway, Sweden, Finland and the Baltic Sea, Lg is consistently the largest secondary phase for all three frequency bands.
- 1 Hz Lg-waves are clearly observed at NORSAR for sources in all of Poland and major parts of the western U.S.S.R. up to distances of about 20^o.
- Sn is the dominant phase for events from the U.K., Belgium, Iceland and the North Atlantic mid-ocean ridge, and for events located to the west of the escarpment of the Norwegian continental shelf.
- The maps tend to be richer in details for higher frequencies, with more pronounced boundaries between source regions.

Wave propagation characteristics related to tectonic features

The map of Fig. VII.1.4 shows the tectonic features that ten-
tatively could be related to the characteristics of propagation of regional phases in the area surrounding the NORSAR array. Indeed, we find a very close relationship between the tectonic

features and the character of the S wavetrain. By comparing the maps in Figs. VII.1.3 and VII.1.4 and bearing in mind also the significance of unshaded areas in Fig. VII.1.3, the following points can be made:

- Lg wave propagation is very efficient for propagation paths that are confined to continental shield type structures and not intersected by major tectonic units. In these directions, 1 Hz Lg waves propagate to 20° from the source, while at 4 Hz Lg is seen out to about 10° from NORSAR.
- No Lg is observed, or Sn dominates over Lg for propagation paths that cross significant tectonic features like graben structures and continental margins.
- Particularly at 4 Hz there is a close connection between some of the finer tectonic details and the propagation characteristics. Since Lg is a phase mostly composed of waves trapped in the crust, this phase is likely to be highly susceptible to changes in the crustal structure. This effect should be more pronounced at higher frequencies, i.e., for shorter wavelengths. At 4 Hz, even a feature like the Törnquist line seems to be an effective barrier to the propagation of Lg.

Implications for real time data processing

The basic assumption in RONAPP that for regional events, Lg is the strongest phase in the S wavetrain, is not valid throughout the area of interest. However, the maps in Fig. VII.1.3 will enable the analyst to assess the likelihood of a detected secondary phase being either Sn or Lg, when reviewing the results from the automatic event processing. On this basis, the epicentral distance estimate could be corrected, if necessary. In some

cases, the phase identification will still be ambiguous, and research is continuing towards developing further criteria.

A next step would be to utilize the regionalization contained in this contribution for an improvement of the real time processing. We think that the results from this study and knowlegde about the general seismicity pattern of the area together with the information already available from the detection processing (direction of arrival, signal frequency and possibly travel time differences between several arrivals in the S wavetrain), constitute a basis for such improvements. Eventually, this information may assist in an expert system's approach to regional array processing.

T. Kværna
S. Mykkeltveit

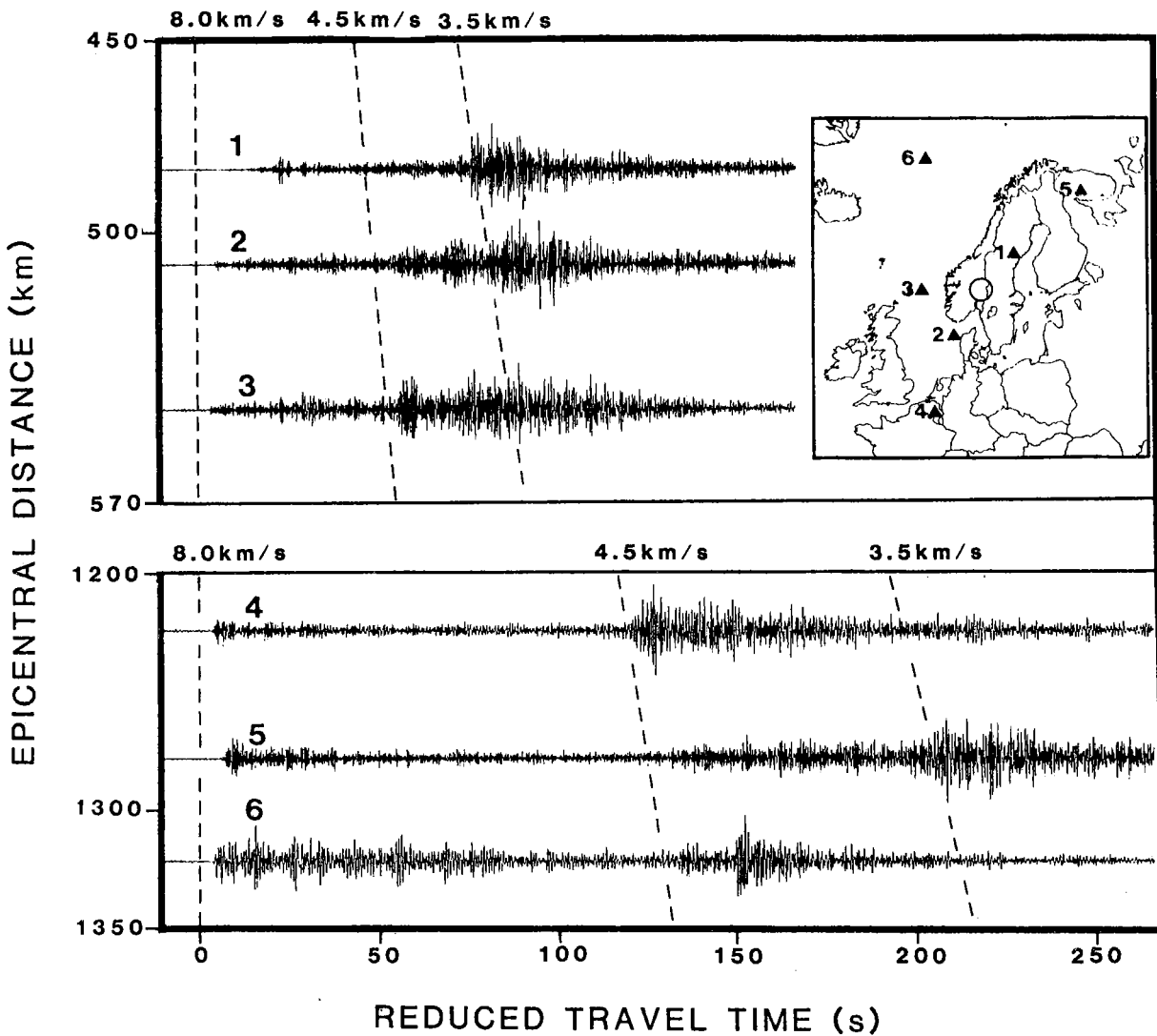


Fig. VII.1.1 Illustration of variation of relative importance of the phases Sn and Lg. The standard group velocities of 4.5 and 3.5 km/s, commonly assigned to Sn and Lg, respectively, are marked by dashed lines. The upper three traces cover the distance interval 480-550 km, while the lower three traces correspond to epicentral distances in the range 1225-1320 km. The location of the NORSAR array is denoted by a ring on the map, and the traces are from NORSAR seismometer 02B01. The data are bandpass filtered 1-5 Hz.

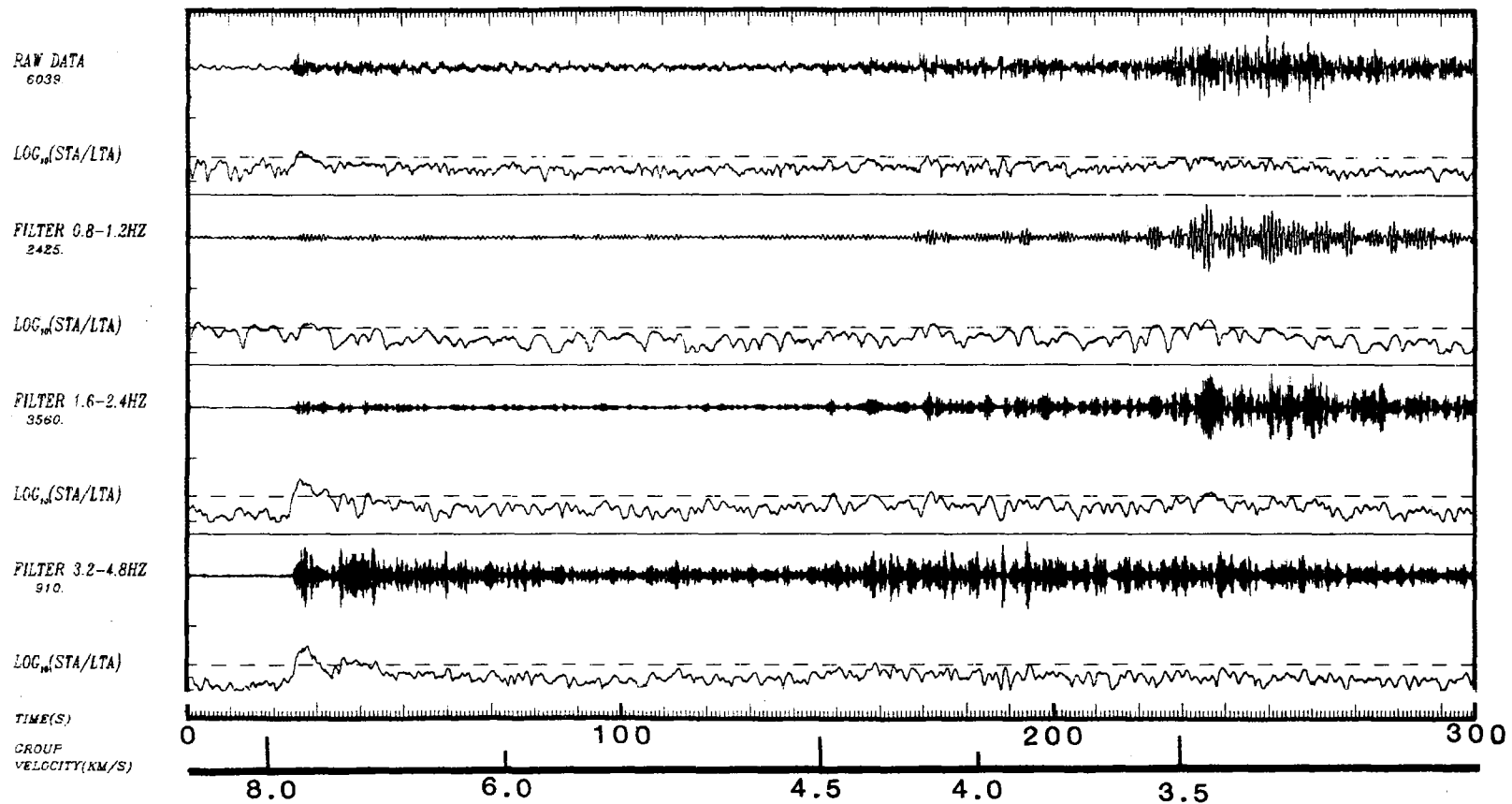


Fig. VII.1.2 Example of output from our processing of regional events. The four seismograms correspond to raw data (top) and three traces of bandpass-filtered data. For each trace, the logarithm of the STA/LTA-ratio is plotted beneath, and a threshold of 3.0 for STA/ LTA is indicated by a dashed line. For an event to be included in our data base, at least one arrival in the S wavetrain must exceed this threshold for at least one of the three filters. This event is also shown as event no. 5 in Fig. VII.1.1.

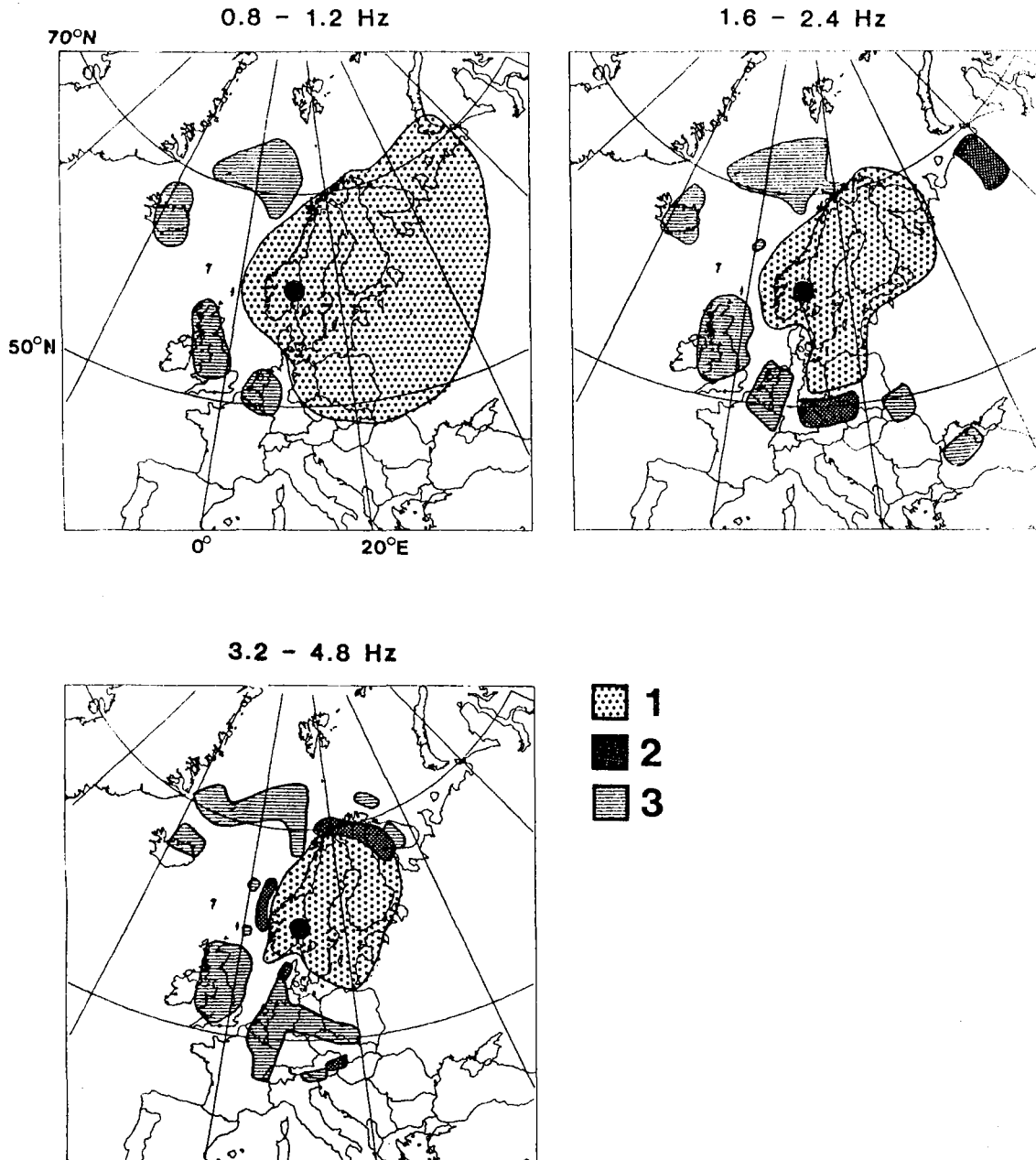


Fig. VII.1.3 Characterization of Lg versus Sn propagation efficiency, for the three different filter bands. The shading codes are as follows: (1) Lg dominant phase in the S wavetrain; (2) Lg and Sn comparable and (3) Sn dominant. Note that the codes are assigned to the source area, and all characterizations are related to seismograms as they appear on NORSAR (filled circle) seismometers.

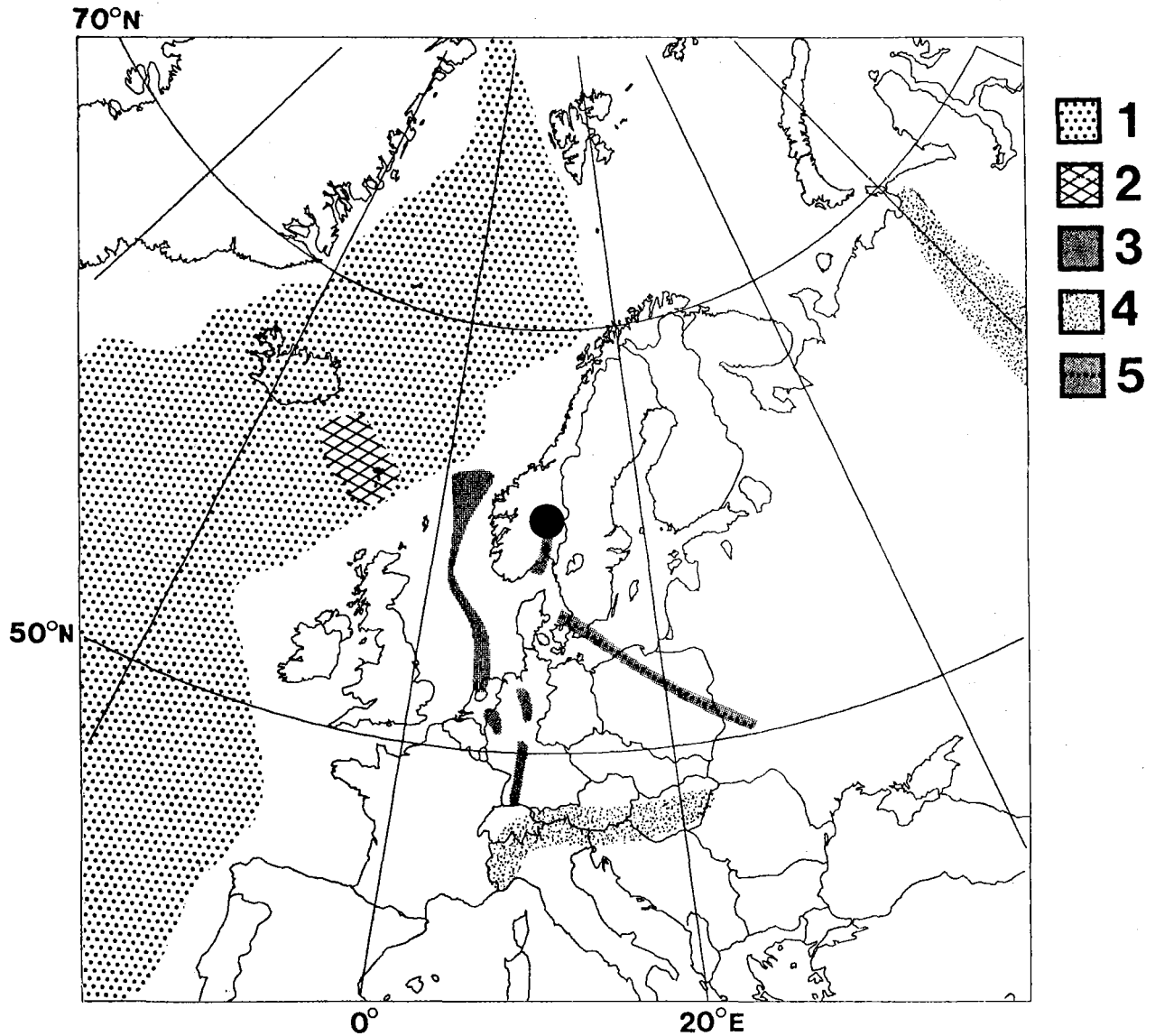


Fig. VII.1.4 Map showing geological features that are related to characteristics of propagation of regional phases to the NORSAR array. Shading codes are (1) Oceanic or oceanic type crust in the North Atlantic; (2) The Iceland-Faeroe Ridge; (3) Graben structures; (4) Major mountain belts; and (5) The Törnquist line. Unshaded areas (except in the Mediterranean region) are of continental type without significant orogenic features.

VII.2 Evaluation of NORESS real time processing performance:

Case study for 132 Western Norway/North Sea events

The performance of the real time processing of regional events detected and located by the NORESS array is currently being evaluated. For this evaluation it is crucial to be able to compile a data base of events that have been reliably located by another agency. Specifically, one would look for a region with a fair number of seismic events and also well covered by seismic stations. One such region within regional range from NORESS is Western Norway.

During the period April-September 1985 a total of 132 seismic events were detected and located by the RONAPP real time processing package for NORESS data, and also reported by the Western Norway Seismic Network. Fig. VII.2.1 shows the location of the NORESS array, the location of the six stations constituting the network, and the area (hatched) within which the seismic events occurred. These events are typically presumed earthquakes offshore and presumed explosions onshore. The magnitudes are in the range M_L 1.5-3.5, and the epicentral distances relative to NORESS range from 200 to nearly 700 km. 41 of the events were verified through reports as explosions and their locations are known. These explosions occurred at site 1 (3 events), site 2 (36 events) and site 3 (2 events). There is a concentration of events in the coastal area at around 60°N, in addition to the explosion site 2.

Data analysis

The real time processing of NORESS data produces standardized plots which provide the analyst with all essential information on the performance of the automatic event processor. Fig. VII.2.2 gives an example of such plots for one regional event. The location of a regional event results from consecutive detections of

P- and S-type arrivals (identified as P or S according to phase velocity) with a common azimuth. The range is estimated from the travel-time difference between the first P phase (usually Pn) and the strongest phase in the S wavetrain, which is assumed to be Lg, propagating at a constant group velocity of 3.5 km/s. RONAPP utilizes the bearing estimated for the Lg phase in the event location procedure.

Fig. VII.2.3 shows differences between P and Lg azimuths for all events in our data base. The median of the absolute values of these differences is 5 degrees. This is an estimate then of the consistency that should be expected among the azimuths automatically determined for the various phases, for the current choice of processing parameters. Our P and Lg azimuths were compared with those corresponding to the locations by the network. We found that for 47 events the Lg azimuth came closest to the "true" value. For 30 events the P azimuth was the better, and for the remaining 55 events, the P and Lg azimuth deviations from the true values were about the same.

Fig. VII.2.4 shows the differences between the ranges estimated by the NORESS online processing and the ones corresponding to the network solutions. As can be seen from this figure, there is a tendency by the NORESS event location procedure to underestimate the range for events in this region. In addition to the events included in Fig. VII.2.4 there are 35 events in the data base with known location at site 2 (Fig. VII.2.1), for which this range difference is between -10 and -20 km.

Bias sources and location improvements

Both systematic and random errors contribute to the deviations in event locations reported above. The location uncertainty of the network must be considered a random error in this context. The

network's average location errors for the explosions with known epicenters are as follows: 30 km for site 1, 10 km for site 2 and 7 km for site 3. For a number of the events in our data base, rather high RMS residuals associated with the network solutions indicate that Lg arrivals may have been mistaken for Sn in reading phase arrivals. This warrants a network relocation experiment for all events in our data base, taking advantage of the regionalization described in section VII.1 of this volume. We think that such a relocation experiment could result in improved network locations.

The frequency-wavenumber analysis leading to an estimate of the arrival azimuth is performed on a finite grid of 41 x 41 points in wavenumber space. This grid size limits the resolution to approximately 3° for the slower phases like Lg and typically 5° for regional P phases. An increase in the number of grid points or a restriction of the frequency-wavenumber analysis to a smaller part of the wavenumber space would increase the resolution power of the azimuth estimator.

The travel time model which is part of the event location algorithm in the RONAPP processing package is based on a uniform Moho depth of 40 km. This is appropriate for a majority of regional propagation paths to NORESS. For the events being studied here, however, a crustal thickness of 30 km in the source region and 35 km at the NORESS array would be adequate. Our location procedure assumes surface sources, while a number of the events in our data base are earthquakes, of unknown but probably intermediate crustal depth. With these changes in our travel time model, the automatically determined ranges would increase by

10 km for surface sources and by 15-20 km for 10-15 km deep earthquakes.

Careful inspection of the NORESS seismograms of our data base resulted in the following observations:

- For 31 events in the distance range 350-500 km we found reason to believe that the Pn phase had gone undetected. For these cases the P phase detected is mostly likely Pg. For most of these events, Pn can be discerned as a weak arrival preceding the much stronger Pg. The time difference is of the order of 3.5-5 sec, corresponding to an underestimation of epicentral distance of the order of 20-30 km. For 28 out of these 31 Pg arrivals, the phase velocity is in the range 6.5-7.5 km/s, which is considered very adequate for this phase. For the three remaining signals, the phase velocity exceed 8 km/s, which would normally be indicative of a Pn arrival. This result indicates a potential of automatically discriminating between Pn and Pg.
- For 9 events, the epicentral range was underestimated by more than 70 km. All of these cases are related to mistaking Sn for Lg, with Sn being the dominant secondary phase or the only secondary phase detected. With proper phase assignments, the ranges for these 9 events would have been correctly determined.
- The main reason for overestimating the range is late detection of the Lg phase.

Corrections along the lines indicated would lead to significant improvements in the range estimation for the Western Norway/North Sea events.

More generally, we think that the experience gained through this case study will result in substantial improvements in the performance of the online processing of regional events recorded on NORESS.

S. Mykkeltveit

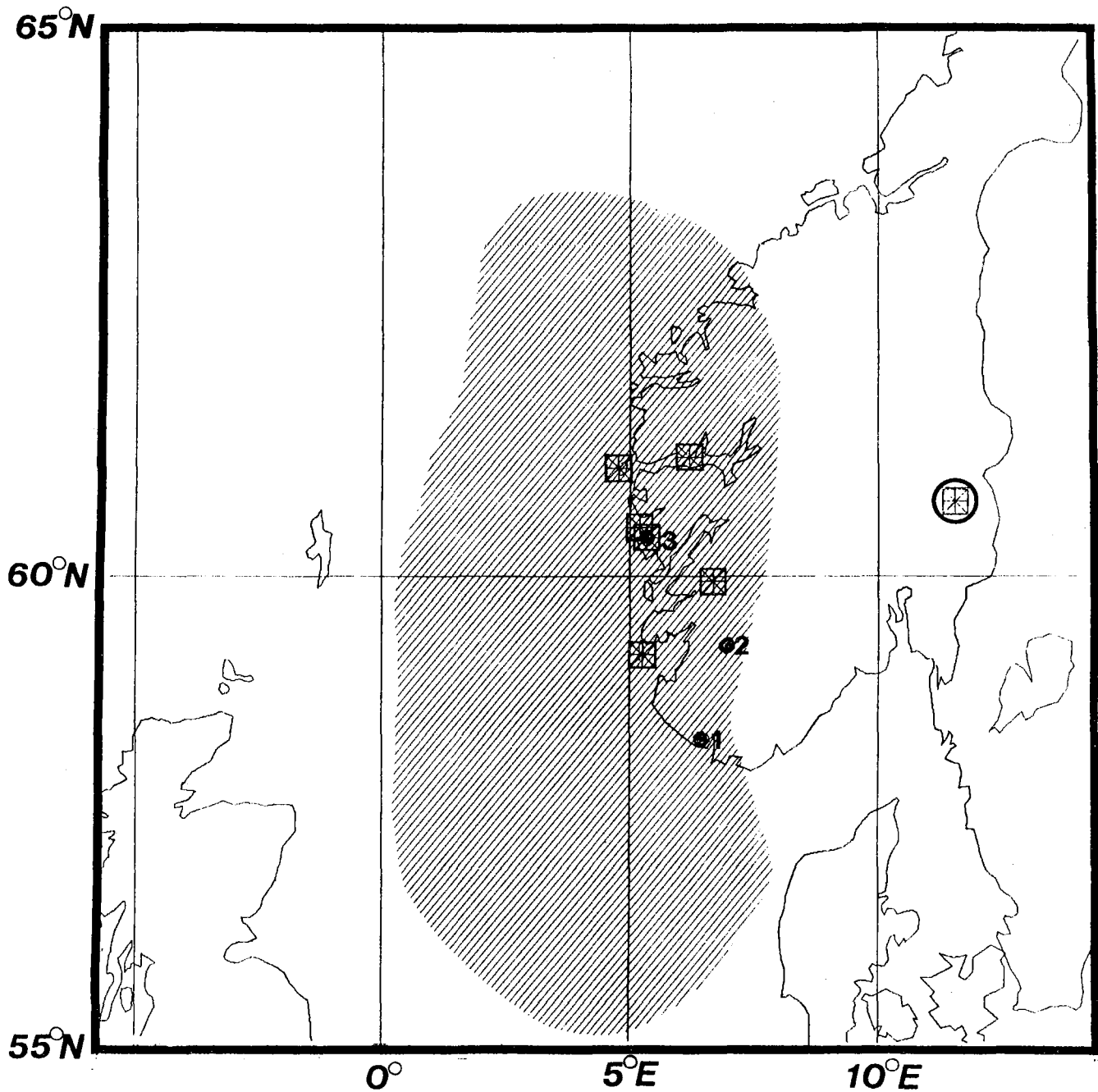


Fig. VII.2.1 Map showing the location of the NORESS array (encircled station symbol), the six stations of the Western Norway Seismic Network, the three locations ("1", "2" and "3") for reported explosions, and the source region (hatched) with the 132 seismic events in our data base. The location of some of the offshore earthquakes was constrained also by signals recorded on seismic stations to the west of the source area, i.e., on Shetland and in Scotland.

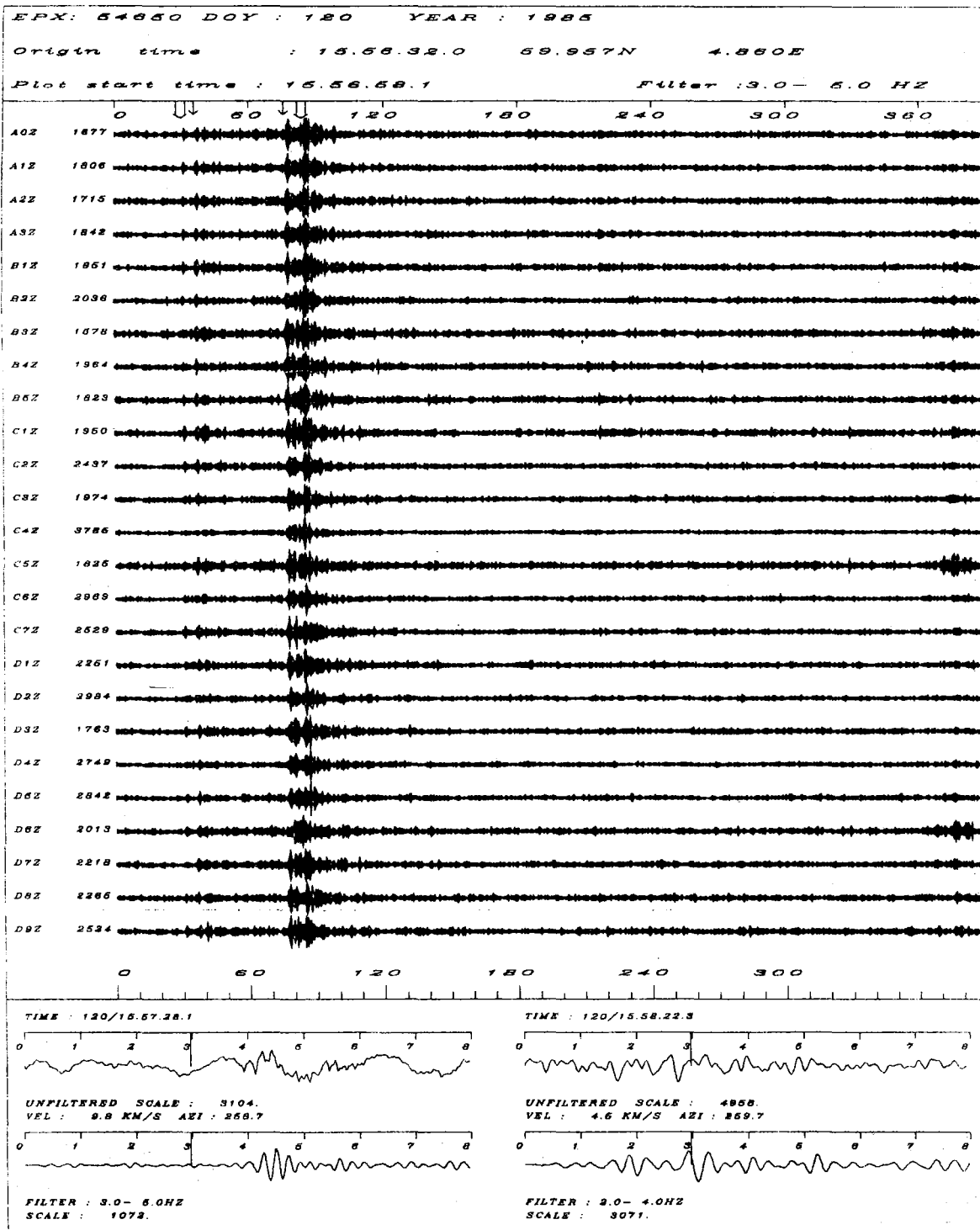


Fig. VII.2.2a Individual NORESS traces for one of the events in our data base. The panel covers $6\frac{1}{2}$ min of bandpass filtered records (3-5 Hz). The four arrows on top of the records indicate detections by the RONAPP real time processing package. The broad arrows correspond to Pn and Lg arrivals, which have been combined to locate the event at the geographical position given on top of the figure. The two additional detections correspond to Pg and Sn arrivals. P and Lg beams are shown in the bottom part of the figure.

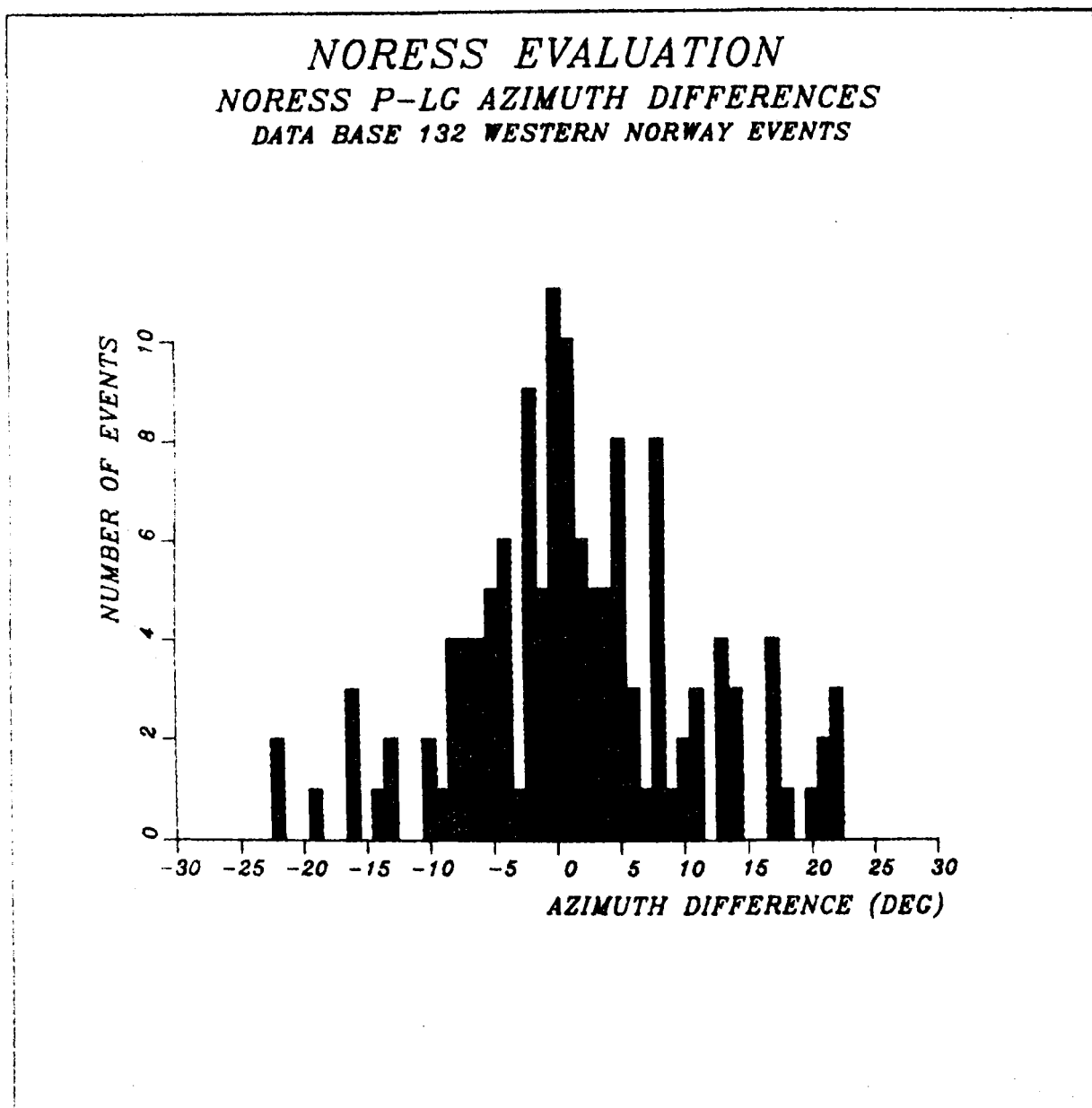


Fig. VII.2.3 The histogram shows the differences between the azimuths automatically estimated for the P and Lg phases by the routine, real time processing of NORESS data, for the 132 events in the data base.

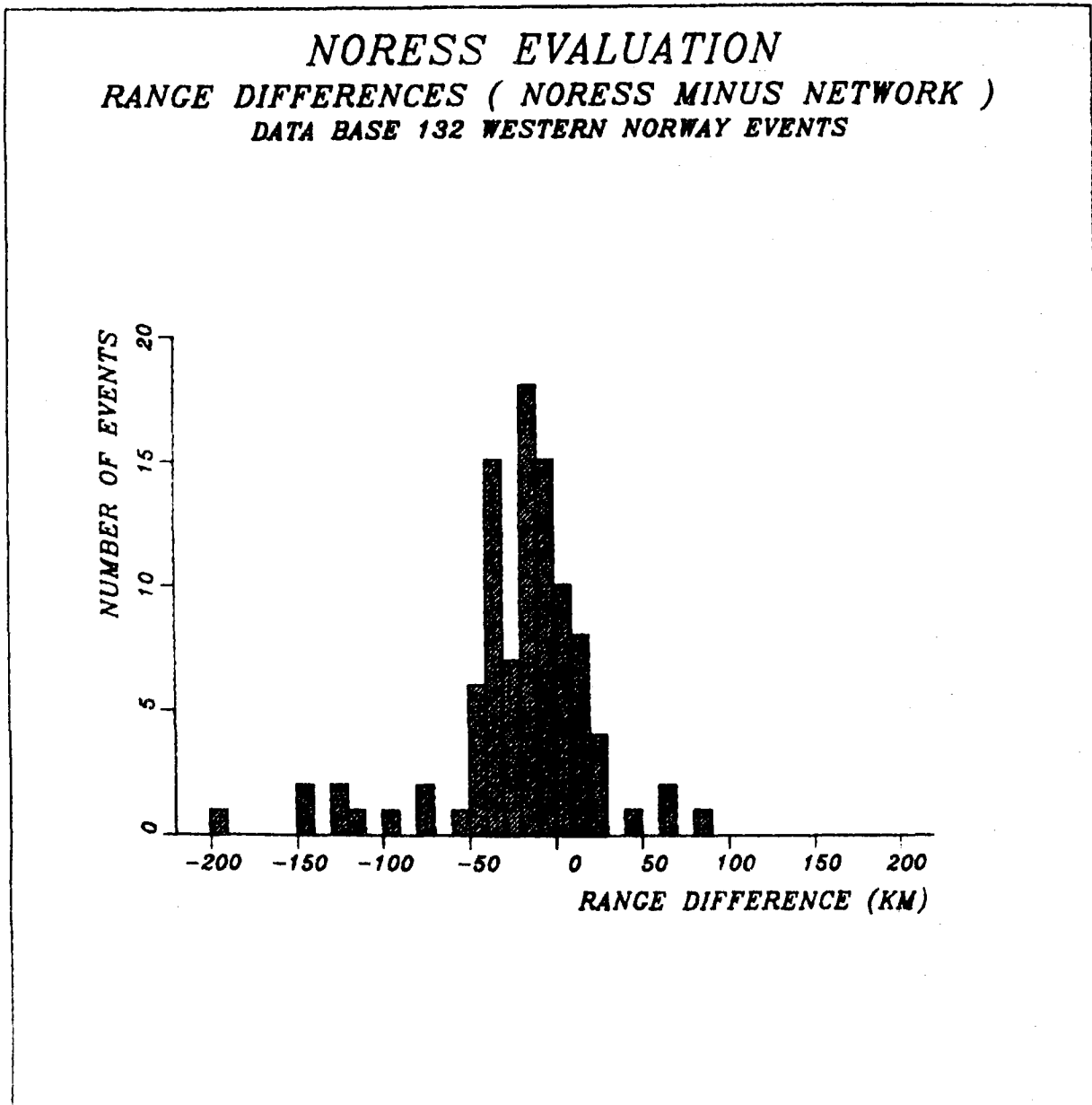


Fig. VII.2.4 The histogram shows the differences between the ranges estimated by the NORESS online processing and the ones corresponding to the network solutions, for the events in our data base. 35 events with known location at site 2 (Fig. VII.2.1), for which this difference was between -10 and -20 km, are not included in the figure.

VII.3 Initial results from NORESS detection processing

Since January 1985 data from the new small-aperture array NORESS in Norway have been processed in real time at the NORSAR data center at Kjeller. The data used in the detection processing comprise 25 SPZ channels, deployed over an area 3 km in aperture and sampled at 40 Hz rate. The detection algorithm (RONAPP) has been described by Mykkeltveit and Bungum (1984), and the current implementation consists of

- Digital narrow-band filtering using a set of Butterworth recursive bandpass filters
- Beamforming, using both conventional and incoherent (envelope) beams
- A linear STA/LTA detector applied to each beam
- Frequency-wavenumber analysis of detected signals
- Association of regional phases to aid in locating events.

In the reporting period (April-September 1985), the RONAPP system has been operated with a fixed beam deployment, as summarized in Table VII.3.1. This deployment, which at the current stage is to be considered experimental, has been based upon the desire to obtain a balance between teleseismic and regional phase detection, within the limits of the processing system capability. Briefly, the current deployment is described as follows:

Beams 1-7 and beam 17 are infinite-velocity conventional beams with filter bands ranging from 1-3 Hz (beam 1) to 8-16 Hz (beam 7). For each of these beams, a subset of the array has been selected as shown in the table. Generally, the low-frequency beams have been formed from the outer rings (C and D), whereas the highest frequency beams are based on the inner (A and B) rings. It has previously been found (Mykkeltveit et al, 1985) that selecting such frequency-dependent subgeometries leads to

increased SNR relative to utilizing all sensors of the array in the beamforming.

Beams 8-16 are steered beams of typical teleseismic velocity (14 km/s), and variable azimuths and filter bands. All of these beams are steered towards Eurasia (azimuth range 0-180 deg), with the intention of providing improved teleseismic detection of the high-frequency signals seen from this area.

Beams 18-20 are incoherent (envelope) beams, which have been formed by filtering individual sensor traces and then adding the absolute values of the filtered traces with no time shift involved. As shown by Ringdal et al (1975), such beams are especially well suited for detecting signals of low coherency across the array. This would, for NORESS, typically occur for high frequency secondary phases.

We comment that the RONAPP package is very flexible with respect to beam deployment, within the overall limitation of 20 beams. Currently, the heavy filtering load involved in forming incoherent beams limits the number of such beams to 3, otherwise, it would have been desirable to include more high-frequency beams of this type. The threshold setting in the current RONAPP system has been somewhat conservative, in order to avoid extensive f-k processing of noise detections. In the near future, attempts will be made to allow for lower SNR thresholds.

In the following, we present some initial statistics on NORESS on-line detection results. These are based on the time period April-September 1985, and cover only those intervals (about 75 per cent of total time) when no significant land line transmission problems were encountered. Such problems were responsible both for occasional system outage and periods of large number of spike detections. It is noted here that the

satellite transmission of NORESS data to the U.S. has been conducted with minimal disruption in the period, thus the reliability of the NORESS field system has been excellent throughout.

Fig. VII.3.1 shows NORESS detections distributed by time of day (GMT). The most noteworthy feature is the large increase in overall detection numbers during daytime hours (local time is 1-2 hours different from GMT). This is clearly attributable to mining explosions, road work, etc., and the figure shows that the number of detected local and regional P phases (velocity 6-12.5 km/s) increases in the same proportion as the total detection numbers during daytime hours. In contrast, the number of detections with teleseismic P-velocities (>12.5 km/s) remains nearly independent of time of day. With the current parameter setting, there has in average been 102 NORESS detections per data-day, of which 25 are of estimated velocity 6-12.5 km/s and 18 of velocity >12.5 km/s.

In Fig. VII.3.2, NORESS detections are plotted by beam number. Note that in this, as well as the other statistics, only the beam with largest SNR is counted for each detection, and that the RONAPP processor groups detections together if they are separated in time by less than 4 seconds. From the figure we see that most of the detections with teleseismic phase velocities occur on beams 1-5, whereas the incoherent beams (18-20) represent almost exclusively detections with phase velocities <6 km/s (typical for secondary phases). A significant number of detections with low and intermediate phase velocities also occur on the high-frequency infinite velocity beams 5-7.

The distribution of NORESS detections by estimated azimuth is shown in Fig. VII.3.3. The concentration of detections in the azimuth interval 90-120 degrees is mostly associated with mining activity in central Sweden and western Russia. With regard to detections of estimated teleseismic velocity, the large majority

is in the range 0-120 degrees, covering mostly Asia. It should be noted that both the azimuth and velocity estimates computed by RONAPP have a fair amount of uncertainty, which must be taken into consideration. This will be further discussed in subsection VII.4.

Fig. VII.3.4 shows incremental and cumulative recurrence statistics for NORESS detections as a function of SNR. Coherent and incoherent (envelope) detections are plotted separately. For coherent beam detections, $\log N$ (N = number of detections) increases approximately linearly with decreasing $\log(\text{SNR})$. On the other hand, the number of incoherent beam detections shows a sharp increase at low SNR values. This is partly because SNR of secondary phases almost always is very low, since the "noise" preceding such phases is the P-coda from the same event. However, preliminary review has also shown that the number of "noise" detections is significant for the envelope beams. Many of these have a very low apparent velocity (< 3 km/s), and procedures to eliminate such false alarms are currently being investigated.

In Fig. VII.3.5, we have subdivided the coherent beam detections into the three velocity intervals described earlier, and plotted separate recurrence statistics. For velocities < 6 km/s, the number of detections increases very sharply with decreasing SNR, again probably due to a predominance of low SNR secondary phases. (For coherent beams, there appears to be few instances of "noise" detections due to a conservative SNR setting.) The plots for intermediate and high velocity signals are similar, although the "slope" in the latter case is somewhat less steep. In either case, we do not see a sharp increase in the number of detections at low SNR, and this is consistent with the above assertion that

"noise" detections are essentially absent with the current RONAPP parameter setting.

In conclusion, the six-month period of RONAPP operation with fixed parameter setting has provided valuable statistical information which will now be used in incorporating improvements into the processing system. In parallel with this, results are now being obtained from a systematic review of NORESS bulletin output which has recently been initiated. Altogether, we plan, in the near future, to generate a new beam deployment, including possible lowering of the coherent beam SNR thresholds. The introduction of variable thresholds for incoherent beams (lower thresholds immediately following regional P detections) will be considered as a possibility to improve secondary phase detection, as will the possibility of masking "noise" detections with very slow phase velocities. Another planned refinement is to introduce a subroutine for faster f-k analysis, thus eliminating a serious bottleneck in the real-time processing, and to implement an interpolation procedure to obtain better precision in phase velocity and azimuth estimates than the current grid points allow. Finally, the regional signal characteristics discussed in subsections VII.7.1 and VII.7.2 will be taken into account in improving automatic phase association procedures.

F. Ringdal

References

- Mykkeltveit, S. & H. Bungum (1984): Processing of regional seismic events using data from small-aperture arrays, Bull. Seism. Soc. Am., 74, 2313-2333.

Mykkeltveit, S., D.B. Harris & T. Kværna (1985): Preliminary evaluation of event detection and location capability of the small aperture NORESS array, NORSAR Semiannual Technical Summary, 1 Oct 84 - 31 Mar 85, NORSAR, Kjeller, Norway

Ringdal, F., E.S. Husebye & A. Dahle (1975): P-wave envelope representation in event detection using array data, IN: Exploitation of Seismograph Networks (E.G. Beauchamp, ed.), Nordhoff-Leiden.

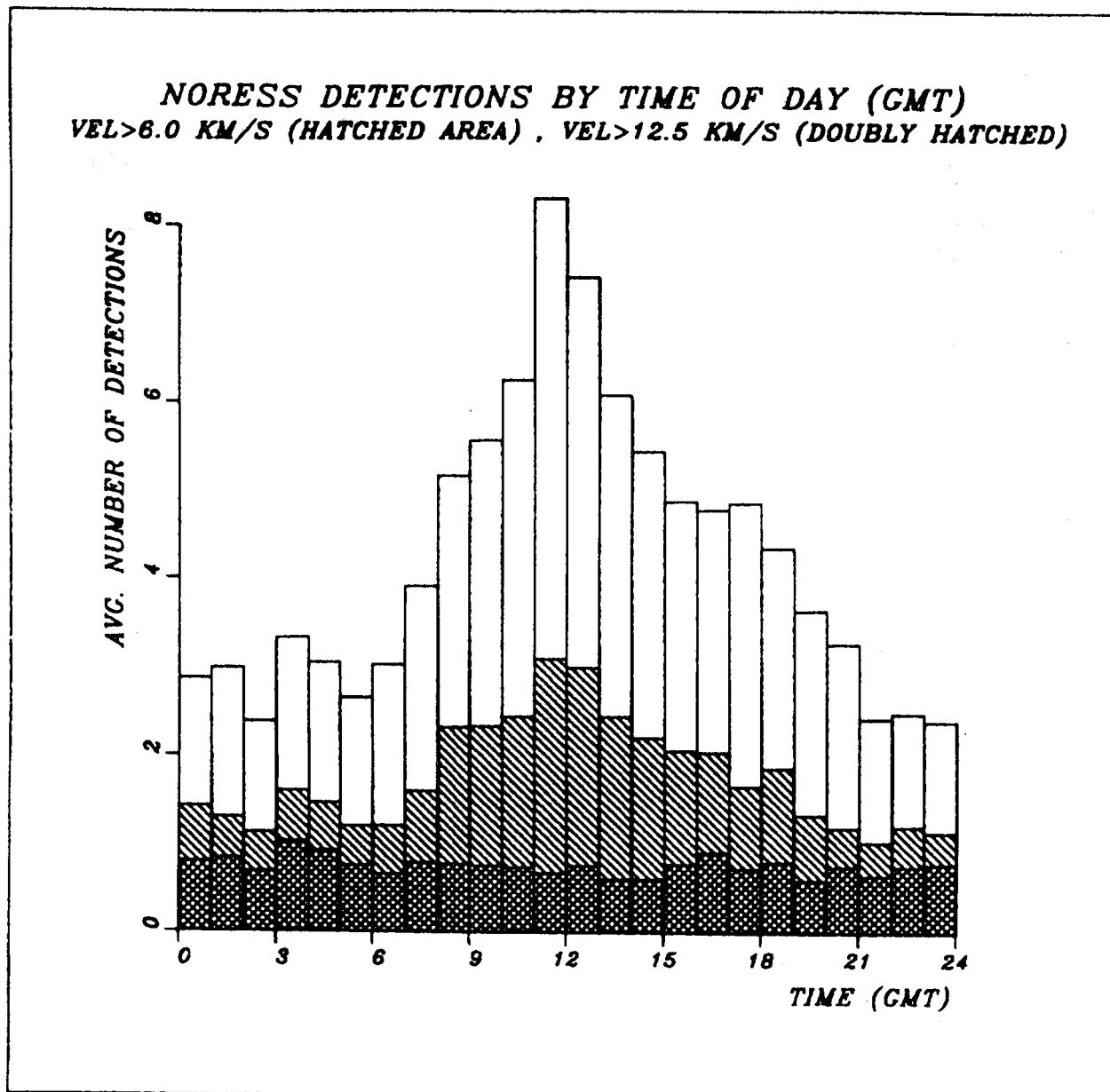


Fig. VII.3.1 Distribution of NORESS detections as a function of time of day (GMT). The average number of detections per hour is plotted, based on the time interval April-September 1985, with correction applied for system down times. The total heights of the columns correspond to all detections within the respective hours.

Unhatched areas: detections with estimated phase velocity < 6 km/s.

Singly hatched areas: detections with phase velocity between 6 and 12.5 km/s.

Doubly hatched areas: detections with phase velocity exceeding 12.5 km/s.

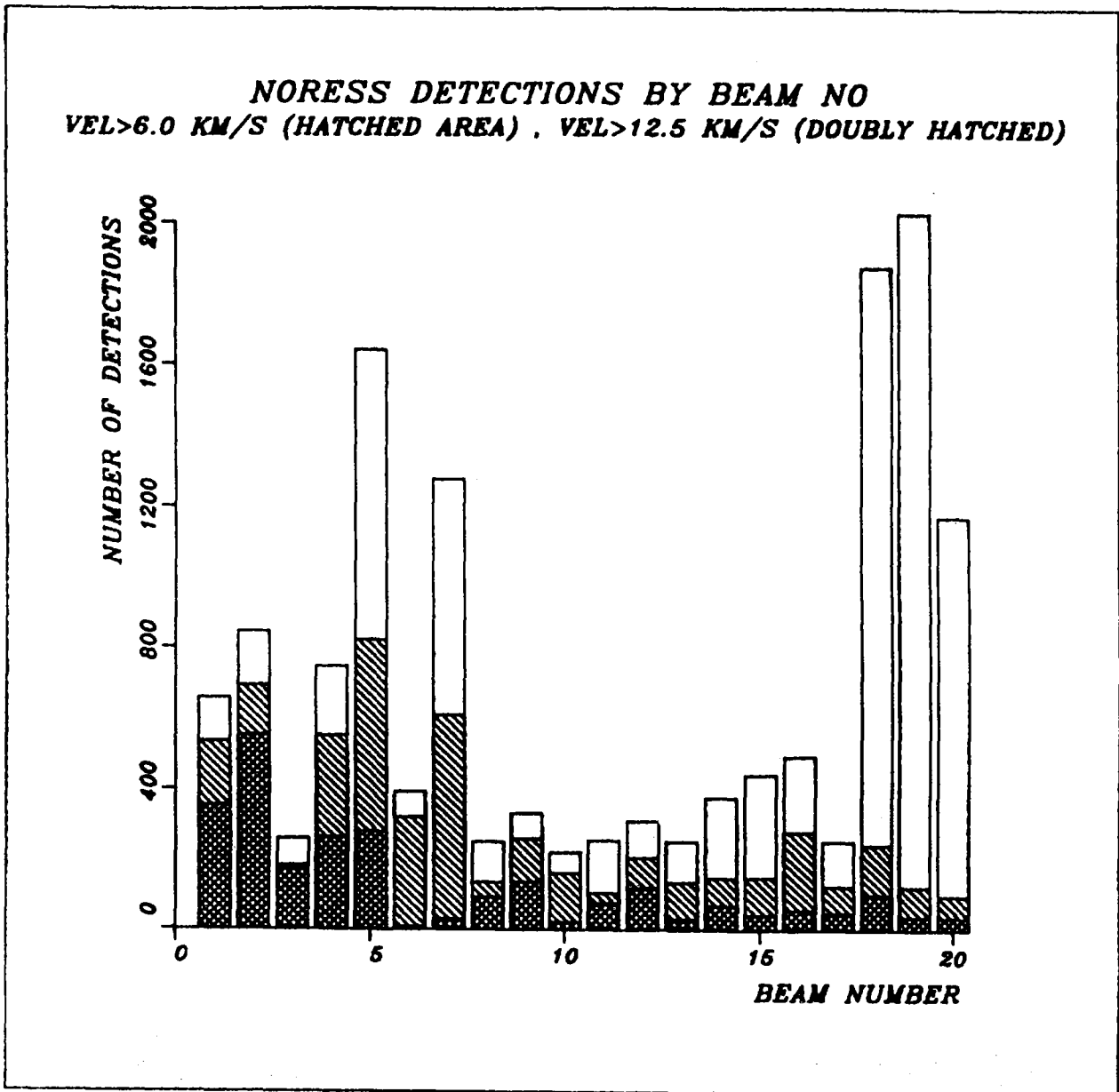


Fig. VII.3.2 NORESS detections during April-September 1985 distributed by beam number (see Table VII.3.1). For each detected phase, the beam with the largest SNR has been selected. The hatching convention is the same as in Fig. VII.3.1.

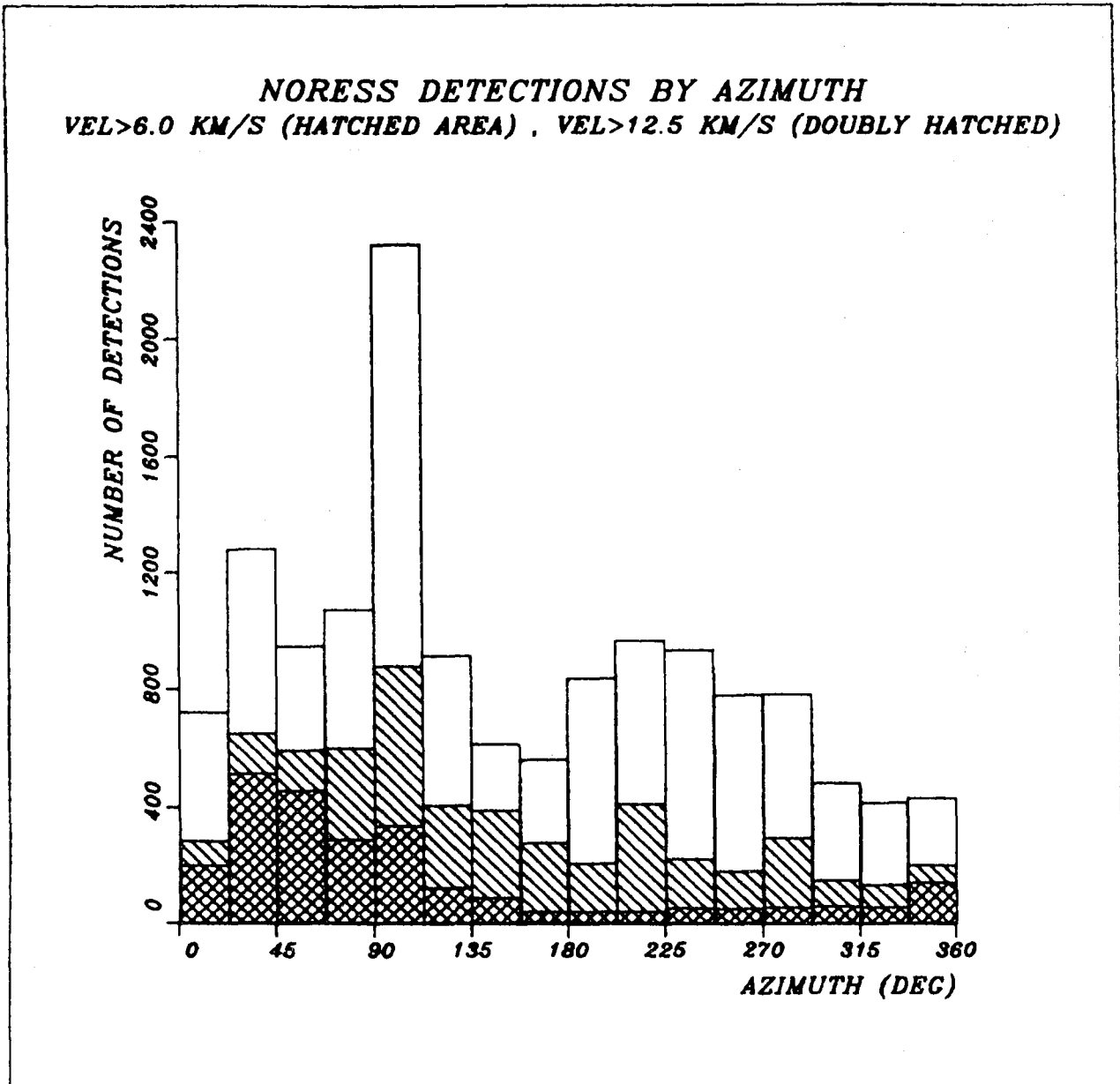
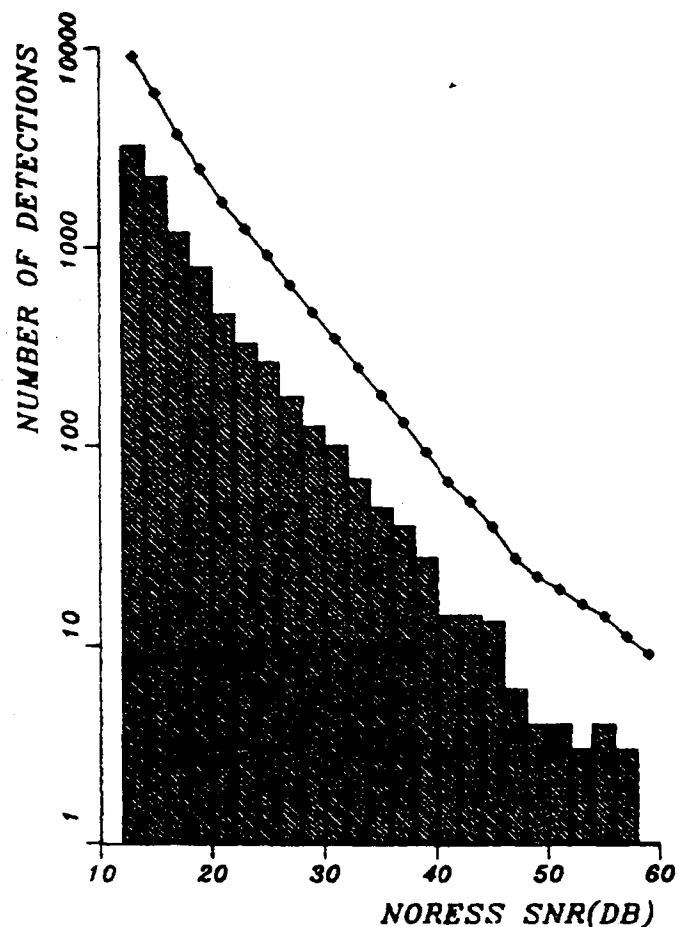


Fig. VII.3.3 NORESS detections during April-September 1985 as a function of estimated azimuth. The hatching convention is the same as in Fig. VII.3.1.

**NORESS DETECTION STATISTICS
DETECTIONS ON CONVENTIONAL BEAMS**



**NORESS DETECTION STATISTICS
DETECTIONS ON ENVELOPE BEAMS**

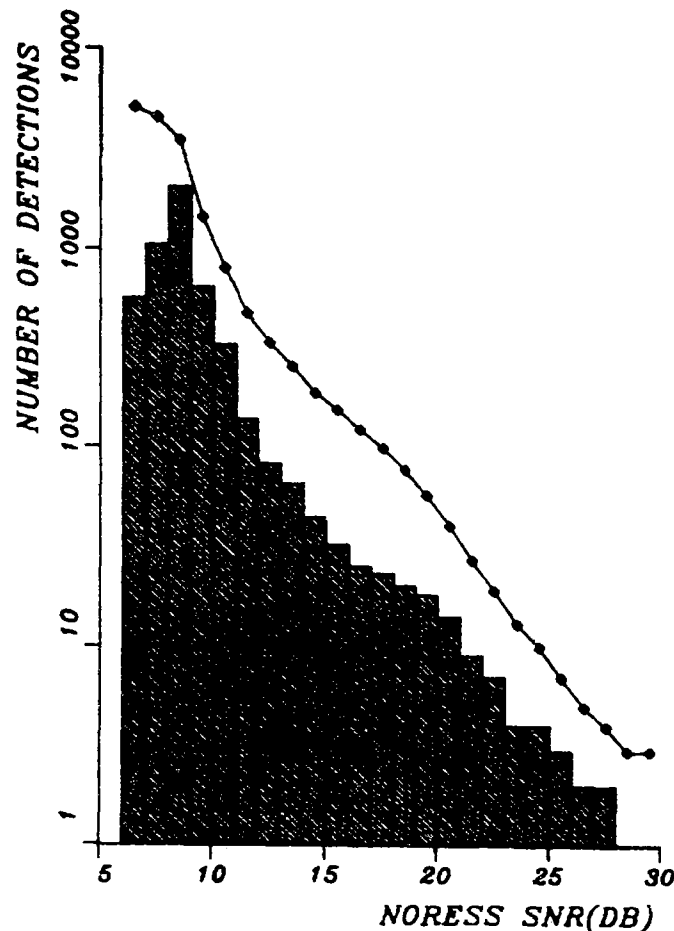
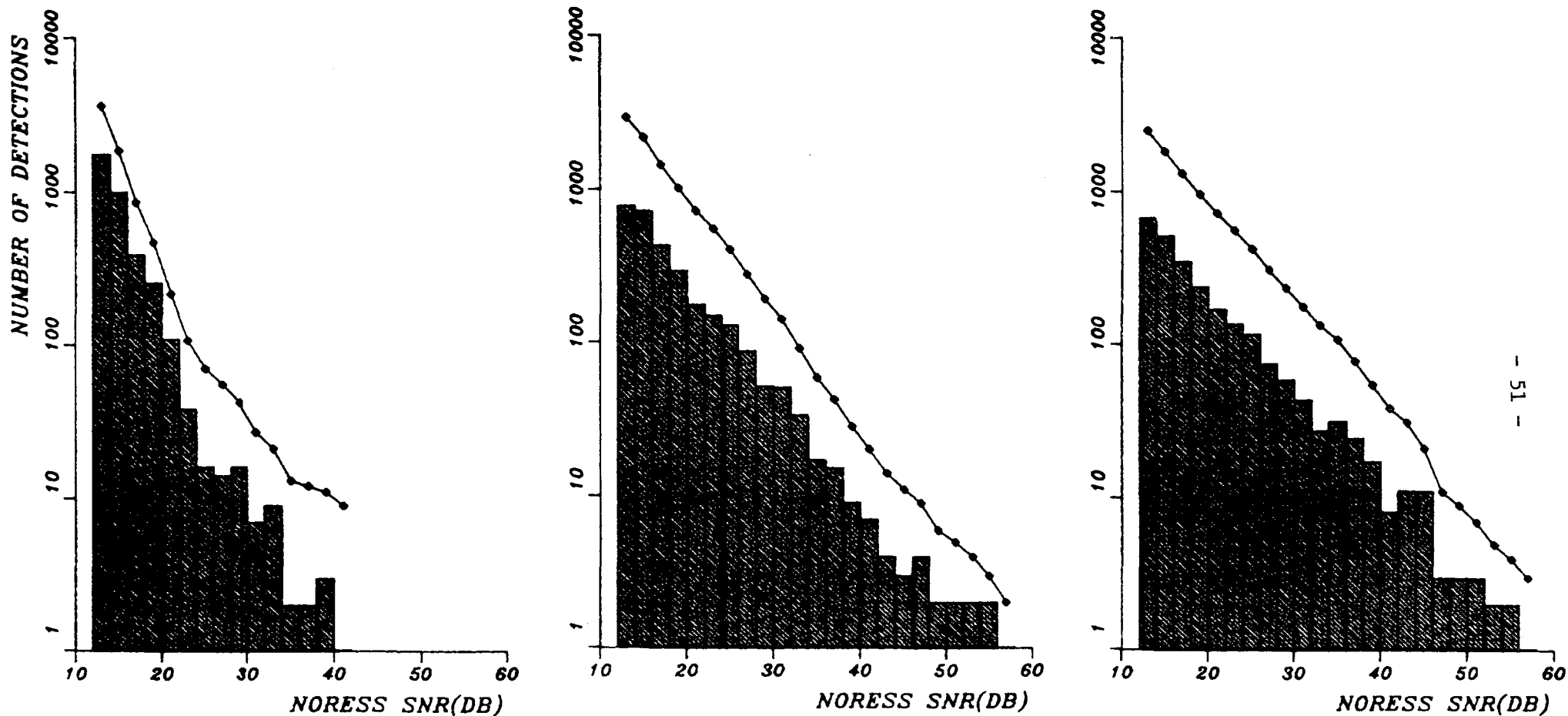


Fig. VII.3.4 NORESS detection statistics during April-September 1985 as a function of SNR. Incremental statistics (histograms) and cumulative statistics (lines) are plotted separately for all detections on conventional beams (nos. 1-17) and envelope beams (18-20) defined in Table VII.3.1. Note the differences in horizontal scales of the two plots.

NORESS DETECTION STATISTICS
CONVENTIONAL BEAMS, VEL<6.0 KM/S

VEL 6.0-12.5 KM/S

VEL>12.5 KM/S



- 51 -

Fig. VII.3.5 NORESS detection statistics for conventional beams (nos. 1-17 of Table VII.3.1) in three velocity intervals (based on NORESS estimated phase velocity). The plots show incremental statistics (histograms) and cumulative statistics (lines). Note the differences in slopes of the logN vs SNR(DB) relations.

VII.4 NORESS-NORSAR processing system comparison

As an initial assessment of the NORESS real time event detector, a study has been conducted comparing the NORESS detection file to the seismic bulletin generated from NORSAR data. Such a comparison is of particular interest since the small NORESS array is located in the same geographical area as the large NORSAR array (Fig. VII.4.1). Thus we obtain a measure of how the high-frequency NORESS processing based on densely deployed sensors compares to the NORSAR processing, which utilizes lower signal frequencies and larger intersensor spacing.

The data base for this study covers the six-month period April-September 1985, during which the NORESS experimental detection processor (RONAPP) has been run with a fixed parameter setting (reference subsection VII.3). For the purposes of this evaluation, time intervals when NORESS operation was degraded due to transmission line problems have been deleted, thus the total number of full data days is 138, or approximately 75 per cent of total time.

The NORSAR event list for these 138 days comprises in total 1628 seismic events. All of these have been reviewed and accepted by the analyst, and thus constitutes an excellent reference data base. The NORESS automatic detection list for the same interval contains 14069 entries, and has not been subject to systematic analyst review. From the results of subsection VII.3, it is clear that the large majority of NORESS detections correspond to local and regional phases, which are not reported in the NORSAR bulletin. Thus, the respective numbers of NORSAR-NORESS detections

alone give no measure of the relative array detection performance, and it is necessary to match the entries directly against one another in order to obtain a comparison.

The following procedure was applied in matching NORESS detection entries against NORSAR-reported events. For each NORSAR event, the predicted P arrival time at NORESS was calculated based on the NORSAR arrival time and the NORSAR estimated phase velocity and azimuth. If one or more NORESS detections were found within 15 seconds of the predicted time, the time of the earliest such detection was then examined. If this differed less than 3 seconds from the predicted time, a match was automatically declared. If the difference was in the range 3-15 seconds (about 5 per cent of the cases), the NORESS recordings were reviewed in order to determine whether or not they represented the same event (typically, this would be a emergent P phase). In cases where no NORESS entry was found within 15 seconds of predicted time, the event was considered not detected by NORESS.

A total of 1376 of the reference events was thus found to be detected at NORESS, i.e., 84.5 per cent. The NORSAR-reported events are almost exclusively at teleseismic and greater distances, thus this high percentage shows that NORESS has an excellent detection capability for teleseismic and core phases. It might be added that a significant number of the NORESS detections which have no matching NORSAR entry also appear to be of teleseismic origin, and this will be the subject of further study in the future.

Fig. VII.4.2 illustrates the differences in observed and predicted NORESS arrival time for the 1376 common events. In reviewing this figure, it must be kept in mind that the NORSAR arrival times have been refined through analyst review, whereas the NORESS times have been determined automatically. There is on

the average a slight positive bias (about 0.5 seconds) in the data, and about 80 per cent of the observed differences are within 1.5 seconds of this average. This indicates that the automatic arrival time definition used in the NORESS processing system works quite well, especially taking into account that the large majority of the events are of low magnitude, and many are characterized by emerging P-waves or multiple phases.

The percentages of NORSAR events detected by NORESS are shown as a function of distance and azimuth (NORSAR estimates) in Figs. VII.4.3 and VII.4.4. Not surprisingly, NORESS detects all of the NORSAR events within 20 degrees distance (as well as many more events not visible on NORSAR recordings). Otherwise, Fig. VII.4.3 shows that the relative NORESS detection performance of P-waves decreases slightly with increasing distance. A noteworthy feature is the high percentage of core phases detected by NORESS; this is primarily due to the predominantly high frequency signals seen from the Kermadec-Fiji Islands region in combination with favorable signal-focusing effects at NORESS for this region.

From Fig. VII.4.4 it is seen that the large majority of NORSAR events are in the azimuth range 0-120 degrees. The NORESS detection percentages are about constant when averaged over 30 degrees azimuth windows. The only exception, the interval 180-210 degrees, comprises very few events, mostly low-frequency earthquakes from the South Atlantic Ridge. Even when taking the uneven distribution of reference events into account, it might be surprising that NORESS does not show higher percentages for the predominantly high frequency signals from Asia (azimuths 0-120 degrees) than for the low frequency signals from North America (azimuths 270-360 degrees). The explanation lies in the signal focusing effects across NORSAR: For high seismicity areas such as the Japan-Kamchatka arc and Hindu Kush, NORSAR benefits from

sharp focusing effects at subarrays 02B and 03C, respectively, whereas the NORESS site (06C) is relatively poor in comparison. The fact that the detection percentages remain so high is attributed to the improved gains by the high frequency signal processing at NORESS. The high NORESS detection percentages from North America are due to relatively favorable focusing effects at the NORESS site for this region, which at least partly compensate for the detectability loss caused by low signal frequencies.

For those teleseismic regions that are characterized by both high-frequency signals and favorable signal focusing effects at the NORESS site, the NORESS detection performance appears to be significantly better than that of NORSAR (judging from SNR of common events). For example, Semipalatinsk explosions show 10-14 dB higher SNR for NORESS when comparing the respective array beams. Admittedly, at least part of this difference will be compensated for by the introduction of higher frequency filters at NORSAR, which is now in progress.

The 1376 common NORSAR-NORESS events have also provided a data base for comparing various signal parameter estimates. Fig. VII.4.5 shows the results with respect to azimuth and slowness. The median NORSAR-NORESS difference is 12 degrees (azimuth) and 1.5 s/deg (slowness). It should be noted that the grid used in the automatic f-k analysis of NORESS signals is relatively coarse, and this is likely the reason for some of the differences. Also, at low SNR, the NORESS f-k solution becomes more unreliable because of noise interference, and analyst interaction would be necessary to improve the estimates in such cases. Nevertheless, it appears that NORESS can provide, in most cases, a useful automatic estimate of teleseismic phase velocity and azimuth. The eventual capabilities of the array in this

regard cannot be assessed until more detailed regional studies have been conducted.

The differences in estimated dominant signal period for NORSAR and NORESS are illustrated in Fig. VII.4.6. This parameter is measured manually at NORSAR, automatically at NORESS, in both cases on the respective array beam. The NORSAR beam is unfiltered, whereas a variable prefilter is applied at NORESS, and this accounts for some of the differences. However, the most significant factor appears to be the array beam loss at high frequencies at NORSAR, causing the NORSAR period measurement to be biased high in many cases.

In conclusion, this study has shown that the high-frequency signal processing conducted at NORESS provides a teleseismic detection capability which is comparable to that of the much larger aperture NORSAR array. NORESS also gives useful azimuth and phase velocity information for teleseismic events, although its capabilities in this regard are limited by the array aperture. Further studies will be directed toward continued improvements in NORESS automatic processing, and also toward taking advantage of the NORESS experience in improving high-frequency signal processing at NORSAR.

F. Ringdal

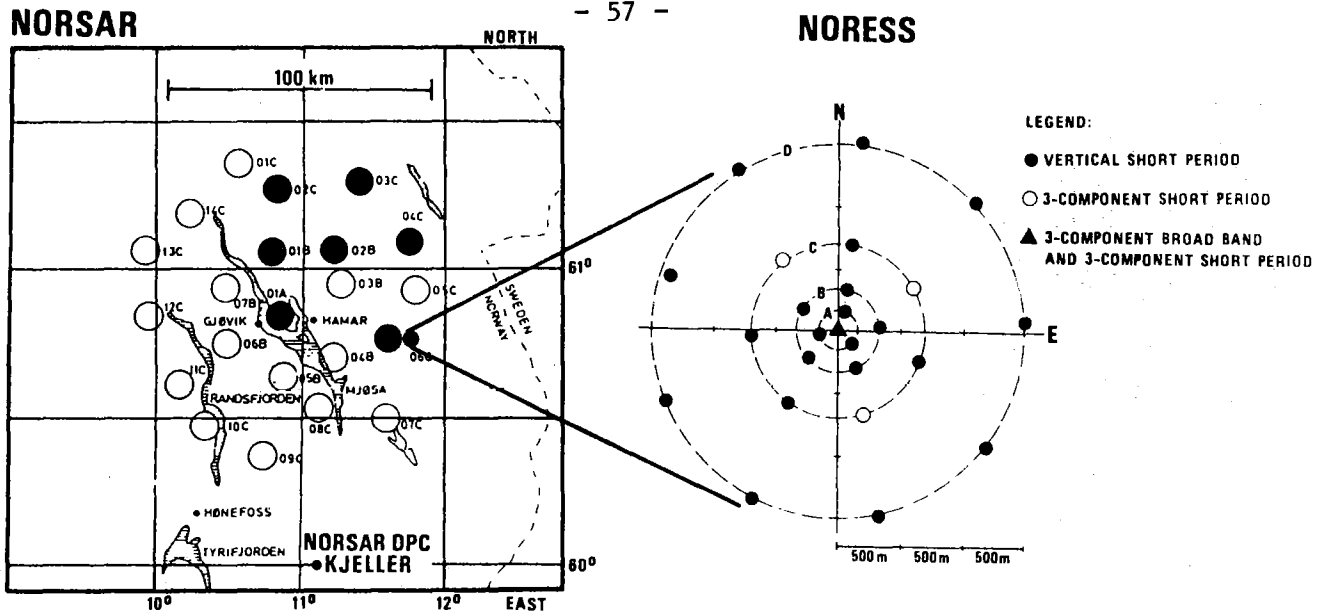


Fig. 1 Map showing the relative geometries of the NORSAR and NORESS array. The current NORSAR SP configuration comprises 7 subarrays (large filled circles), each with SPZ seismometers deployed over an area 10 km in diameter. NORESS comprises 25 SPZ sensors within a 3 km diameter aperture.

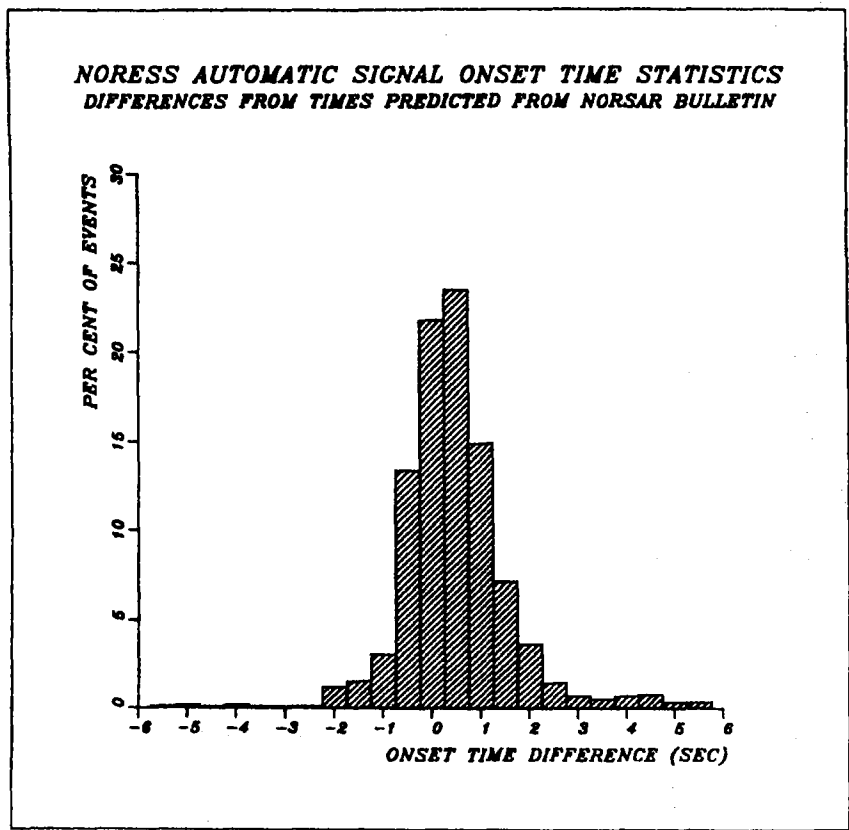
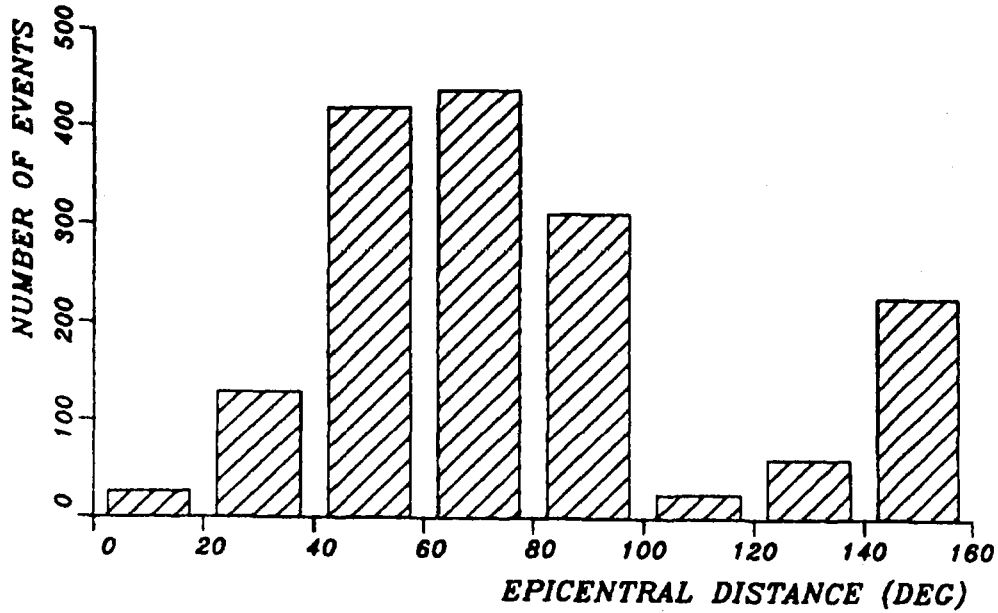


Fig. VII.4.2 Histogram showing the distribution of differences between signal onset times computed for NORESS and predicted onset times based on the NORSAR bulletin. The data base consists of seismic events detected by both systems during April-September 1985.

EVENT DISTRIBUTION BY DISTANCE
REFERENCE NORSAR EVENT LIST APRIL-SEPTEMBER 1985



NORESS DETECTION BY DISTANCE
REFERENCE NORSAR EVENT LIST APRIL-SEPTEMBER 1985

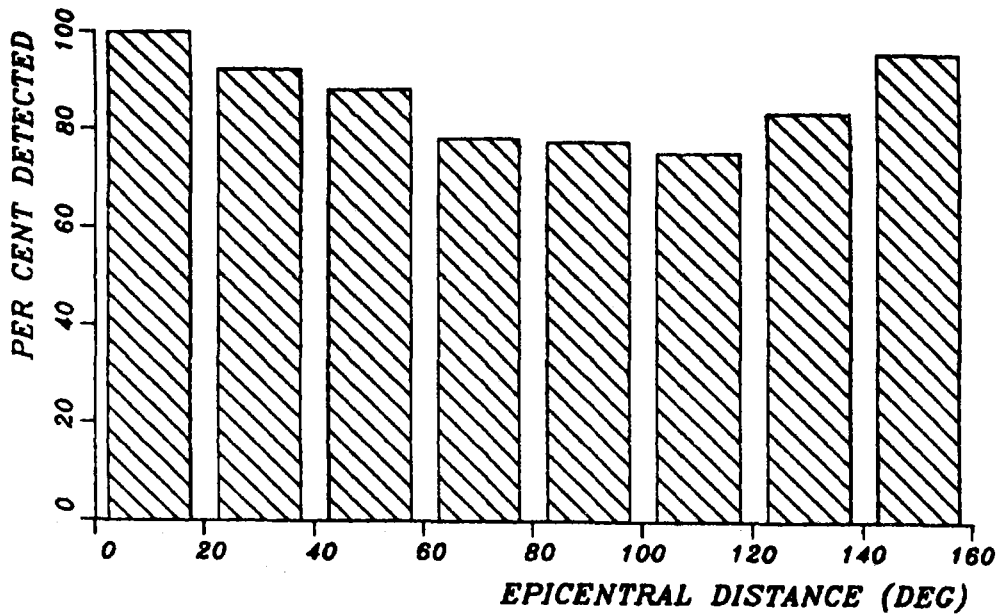
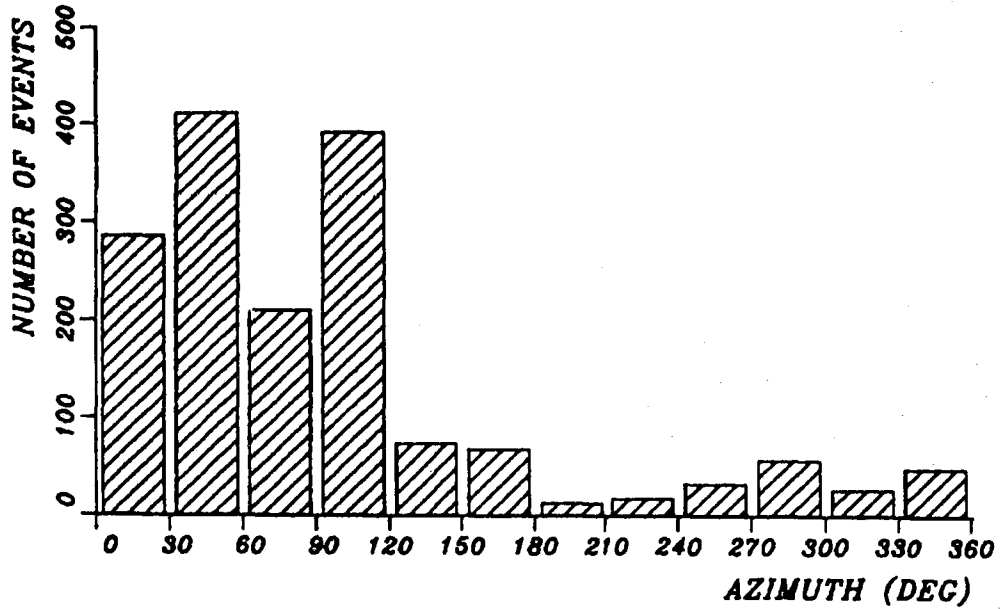


Fig. VII.4.3 Top part of figure shows the distribution by epicentral distance (20 degrees increment) of seismic events reported by NORSAR April-September 1985, during time intervals when NORESS was operational. The bottom part shows percentages of these events detected by NORESS. Note the high NORESS detection percentages at all distances.

EVENT DISTRIBUTION BY AZIMUTH
REFERENCE NORSAR EVENT LIST APRIL-SEPTEMBER 1985



NORESS DETECTION BY AZIMUTH
REFERENCE NORSAR EVENT LIST APRIL-SEPTEMBER 1985

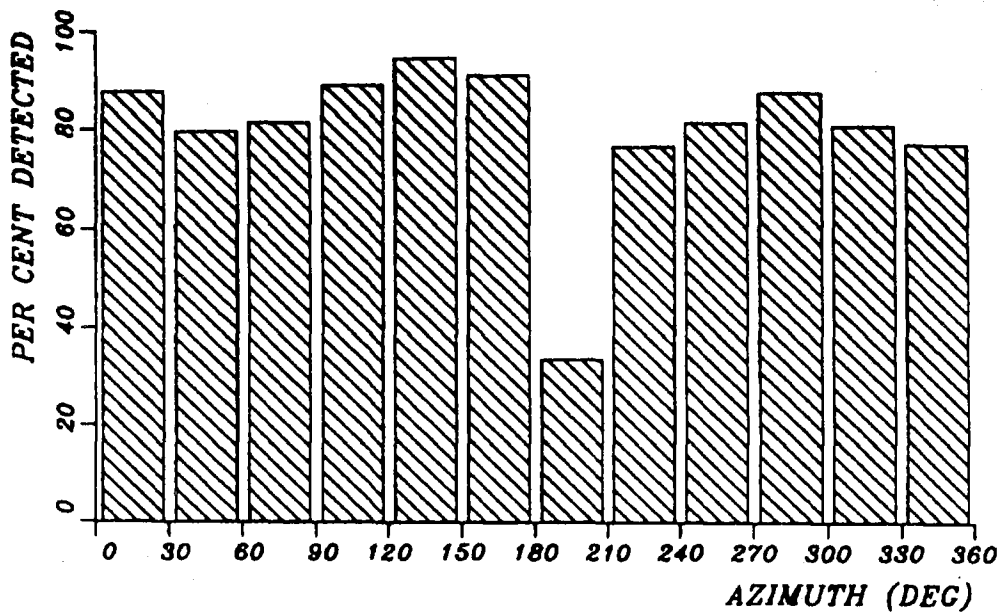
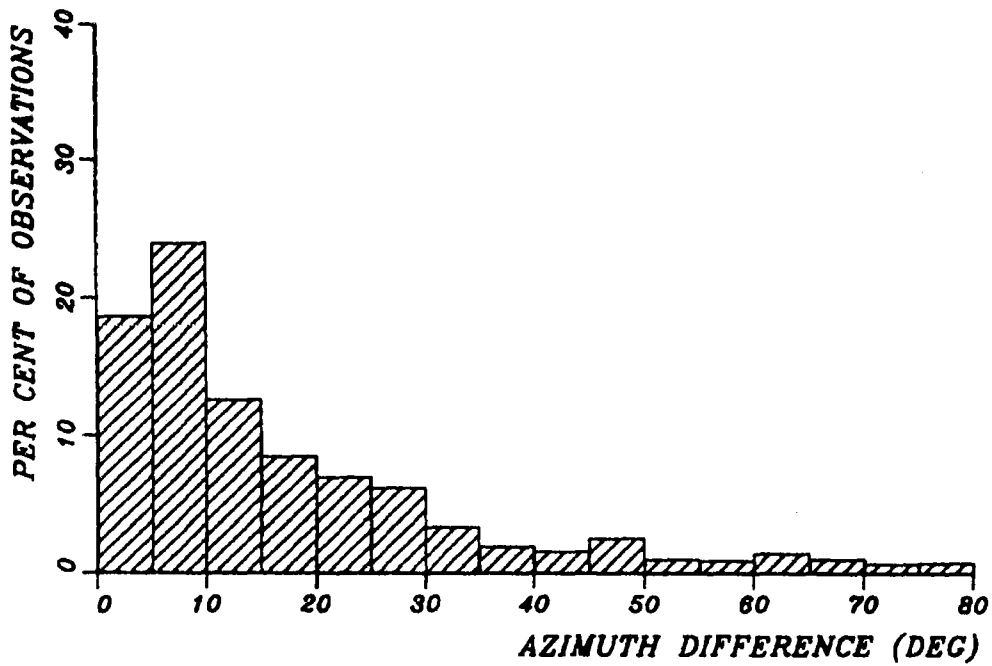


Fig. VII.4.4 Same as Fig. VII.4.3, but with event distribution based on NORSAR azimuth (30 deg increments).

NORSAR-NORESS AZIMUTH COMPARISON
DATA BASE 1376 EVENTS APRIL-SEPTEMBER 1985



NORSAR-NORESS SLOWNESS COMPARISON
DATA BASE 1376 EVENTS APRIL-SEPTEMBER 1985

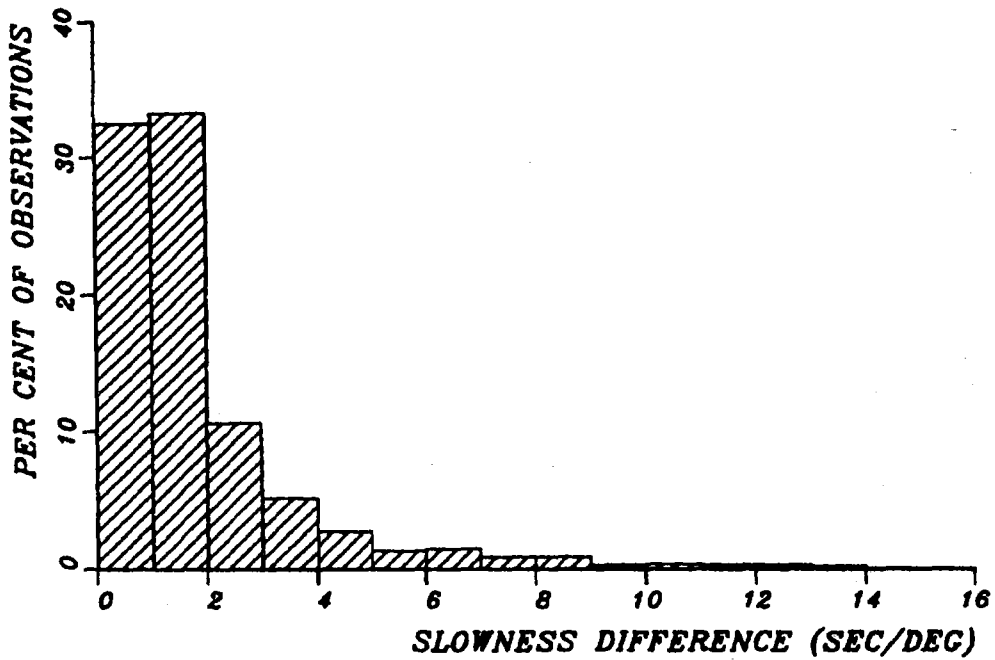


Fig. VII.4.5 Histograms showing differences (absolute values) between NORSAR and NORESS azimuth and slowness estimates for the common events in the data base.

NORSAR-NORESS SIGNAL PERIOD COMPARISON
DATA BASE 1376 EVENTS APRIL-SEPTEMBER 1985

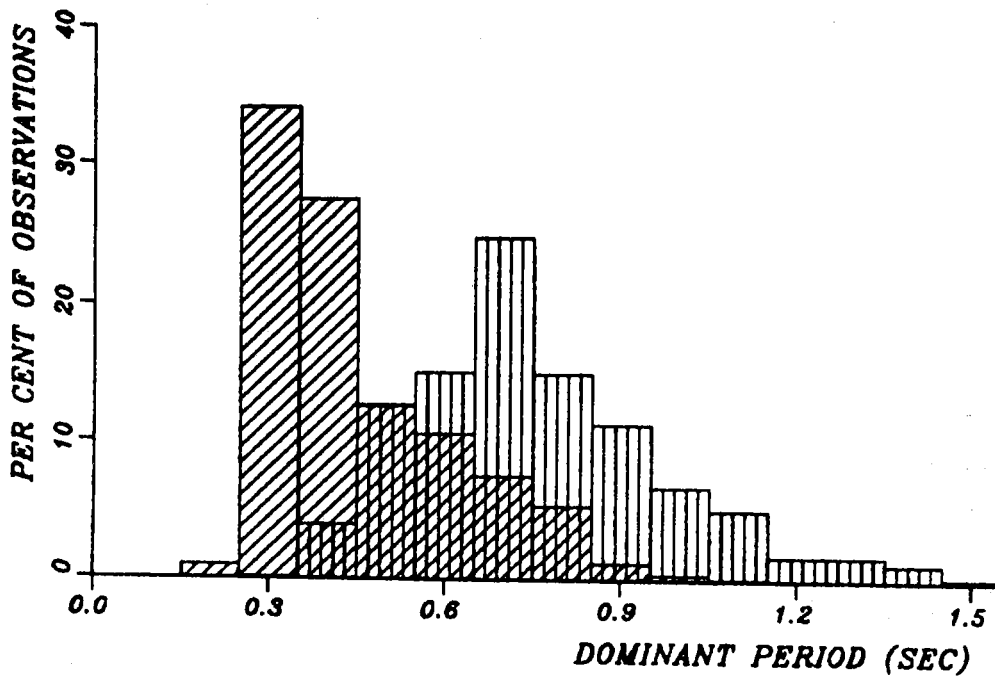


Fig. VII.4.6 Comparison of dominant signal periods estimated by NORSAR and NORESS for common events in the data base. The NORSAR histograms have vertical hatching, vs diagonal hatching for NORESS. Note the significantly lower dominant periods estimated from NORESS data.

VII.5 P-wave spectra from NORESS recordings

A number of earlier studies, some of which based on NORSAR data, have shown that high frequency signal propagation in Eurasia is very efficient, even at teleseismic distances. With the new NORESS installation in Norway, we now have the possibility to study both the spectral contents and spatial coherency of teleseismic phases at higher frequencies than before, since the NORESS SP system, which is based on 40 Hz sampling rate, effectively records signals of up to about 15 Hz frequency.

We have initiated a systematic study of the spectral characteristics of NORESS-recorded seismic phases, and in this paper we present some representative examples, together with brief comments summarizing the most important features. Five events of low and intermediate magnitude (m_b 4.0-5.0) have been chosen, at least three of these are presumed underground explosions. The events are in the epicentral distance range 14-49 degrees. In Figs. VII.5.1 to VII.5.5 we show, for each event, NORESS single sensor and beam time domain traces as well as spectral plots of signal and noise. The beam has been steered to the event epicenter using plane-wave time delays, and is based on the subset of NORESS instruments comprising the center instrument and the C and D rings, i.e., 17 of the 25 NORESS SPZ channels. As discussed by Mykkeltveit et al (1985), this subset provides particularly efficient noise suppression in the band 1.5-3.0 Hz, and is better than the full array in this regard.

The noise spectra have been estimated using the indirect covariance method. We first estimate the correlation function by splitting a long data record into many windows, calculating a sample correlation function for each window, then averaging the sample correlation functions. Typically, we use 20 windows, each of which is 5 seconds long. Because the earth noise has such a

large dynamic range, we prewhiten it prior to estimating the correlation function with a low-order prediction-error filter. The spectrum is then estimated by windowing the correlation function with a 3-second Hamming window, then computing the Fourier transform. The spectral estimate obtained this way is compensated then for the effects of prewhitening and normalized to a 1-second window length.

Signal spectra have been estimated using the same technique, but with 4 overlapping windows, each of 7 seconds length. Start times of these windows are 3, 2, 1 and 0 seconds before signal onset, respectively. Thus we achieve a smoothing of the signal spectra while retaining compatibility with the noise spectra.

The NORESS digital recording system employs gain-ranged 16 bits data words, as described by Stokes (1982). While the overall dynamic range is as large as 120 dB, the actual resolution at any given gain level is considerably lower. Thus, quantization effects become significant for those portions of the spectra which are 70 dB or more below the spectral peak of a given signal, and this must be kept in mind when reviewing the spectra displayed in this subsection. The quantization effects are manifested in these plots as an oscillation in the spectral traces, which is apparent on some events at very high frequencies.

In the following, we briefly comment on the main features of the five events selected:

Event 1: 66.ON 40.8E, distance 14 deg, azimuth 55 deg, $m_b=5.0$

The P wave is very complex, with significant high frequency energy, especially in the P coda. Much of the high frequency energy is lost on the beam, as seen both from the time domain plots and the spectra. There is significant SNR over the entire

frequency band shown, and in fact it appears likely that there would be significant energy also above 15-20 Hz for this event. However, the largest SNR is found in the 2-8 Hz band. This event is in the regional distance range, and has large Sn and Lg phases recorded by NORESS.

Event 2: 46.8N, 48.1E, distance 25 deg, azimuth 107 deg, $m_b=5.0$

The P wave is complex also for this event, due to multiple onsets from different upper mantle P phases. The signal has a clear spectral density peak at 2 Hz, and the spectral density drops much more rapidly with increasing frequency than for Event 1. There appears to be no significant SNR above 12 Hz frequency, even though the quantization noise makes a definite conclusion difficult. Beam signal loss is negligible up to 6 Hz in this case.

Event 3: 49.9N 78.1E, distance 38 deg, azimuth 75 deg, $m_b=4.9$

This event is characterized by a very clear, impulsive P signal. A sharp spectral peak is seen at 2 Hz for the signal, and there is significant SNR out to at least 15 Hz. Beam signal loss is negligible up to 6 Hz. Note the pronounced noise suppression on the beam around 2 Hz (associated with the choice of subgeometry discussed before); this feature, which here is particularly visible, can also be identified on the other figures by close inspection.

Event 4: Central Asia (no NEIS location, distance ~ 40 deg, azimuth ~ 80 deg, $m_b=4.0$

This is a low magnitude event from the same general area as Event 3, and many of the same comments apply. The recordings illustrate in particular the large SNR gain on the beam, especially around 2 Hz, and it is noteworthy that even for an event

at such low magnitude, a significant SNR can be found on the beam up to around 10 Hz frequency.

Event 5: 41.7N 88.4E, distance 49 deg, azimuth 76 deg, $m_b=4.7$

This event has a clear, impulsive P phase recorded at NORESS. In contrast to previous event, the signal power around 2 Hz is much lower than the spectral maximum, thus the best SNR occurs at 4 Hz frequency. Again, the beam has significant SNR up to about 10 Hz.

In conclusion, the studies of these and other events have shown that P phases from intermediate and low magnitude Eurasian events very often contain signal energy well above the noise level up to at least 10 Hz frequency. However, for teleseismic events, the SNR on the beam is usually best at frequencies below 4 Hz; thus for teleseismic event detection purposes, a set of bandpass filters covering the range 1-5 Hz would be expected to give the best performance. At the high frequency end, there is clearly a potential for additional SNR gains through beamforming based on array subgeometries involving only the inner rings, and this will be the topic of a separate investigation.

We emphasize that these results are preliminary, and we plan to continue our research on this topic.

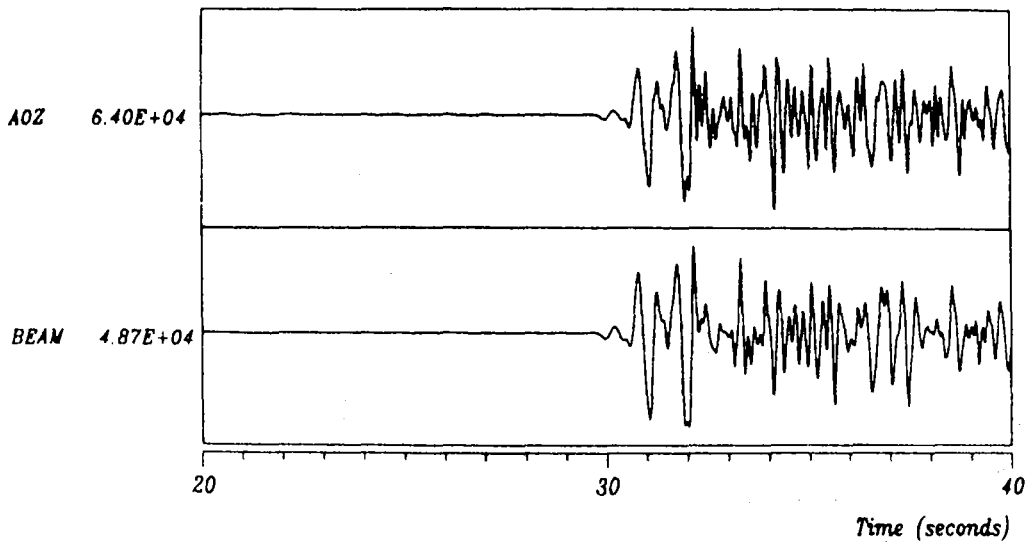
T. Kväerna
F. Ringdal

References

Mykkeltveit, S., D.B. Harris & T. Kvarna (1985): Preliminary evaluation of the event detection and location capability of the small aperture NORESS array, NORSAR Semiannual Technical Summary, 1 Oct 84 - 31 Mar 85, NORSAR, Kjeller, Norway.

Stokes, P.A. (1982): The National Seismic Station, Sandia Report SAND81-2134.

PST 85 199 21 17 45 69



07/18/85 21.15.00

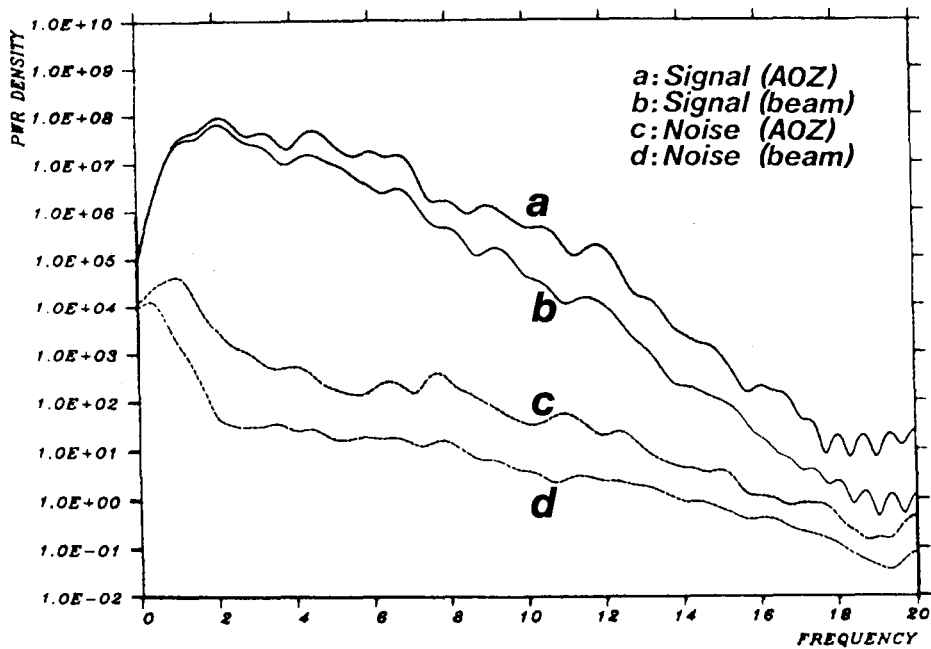
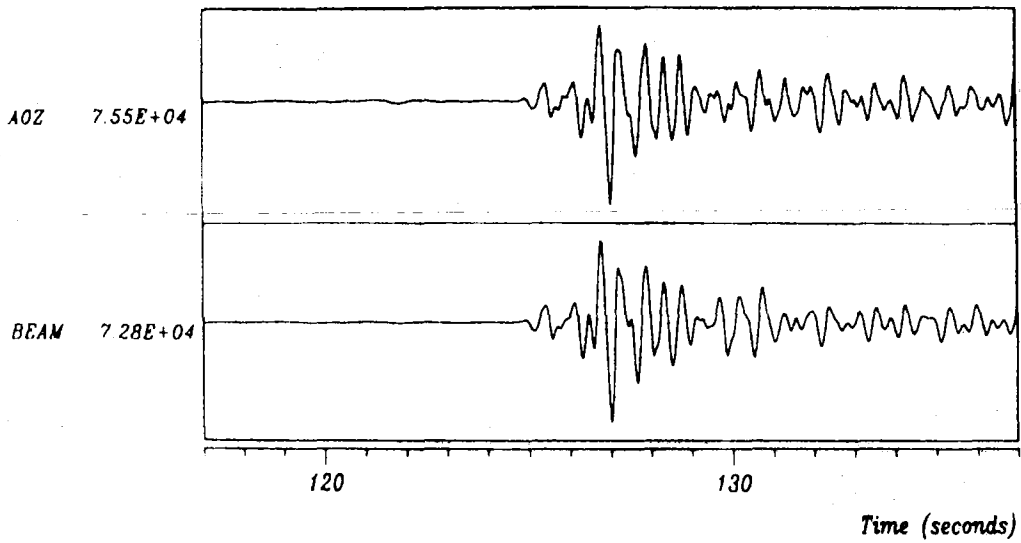


Fig. VII 5.1 The top part of the figure shows NORESS single sensor trace (instrument A0Z) and NORESS steered beam (employing the 17 seismometers A0, C1-7, D1-9) for Event 1 described in the text. The lower part of the figure shows power density spectra for (a) signal (A0Z), (b) signal (beam), (c) noise (A0Z) and (d) noise (beam). Tick marks on the vertical axis correspond to 10 dB power increments. The spectra have not been corrected for system response.

PST 301 06 03 20 80



10/27/84 06.00.00

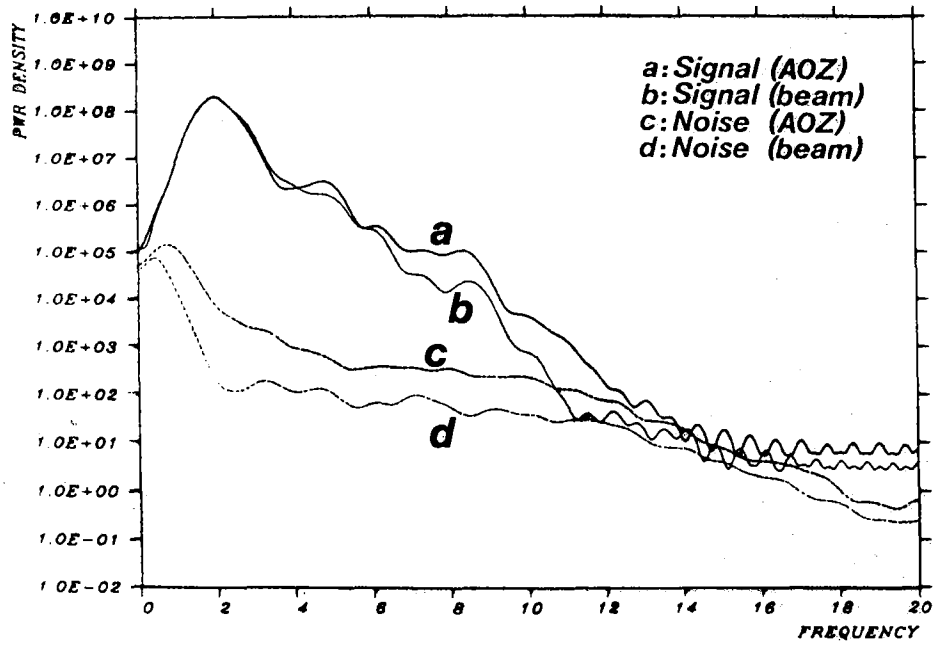
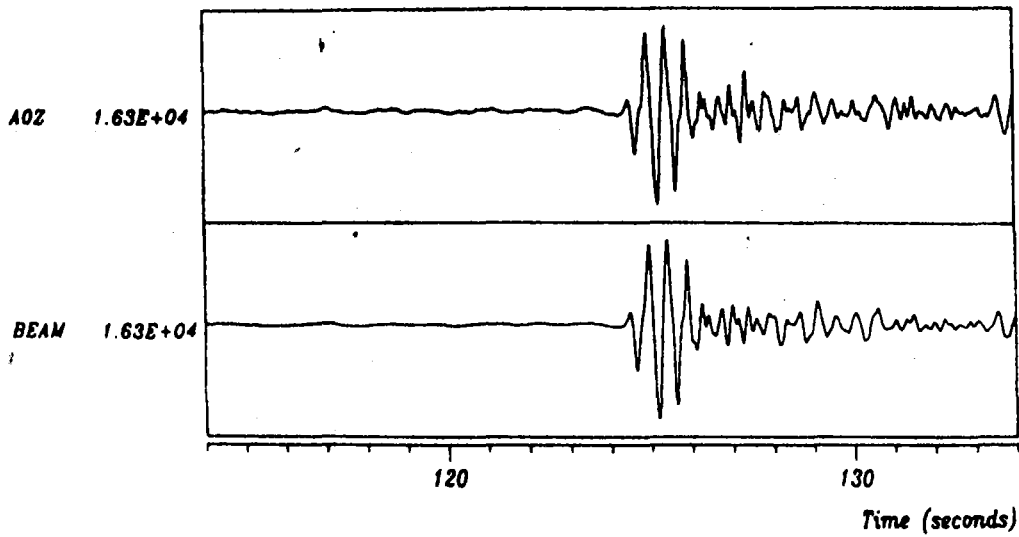


Fig. VII.5.2 Same as Fig. VII.5.1, but for Event 2 described in the text.

PST 85 206 03 16 20 74



07/25/85 03.11.00

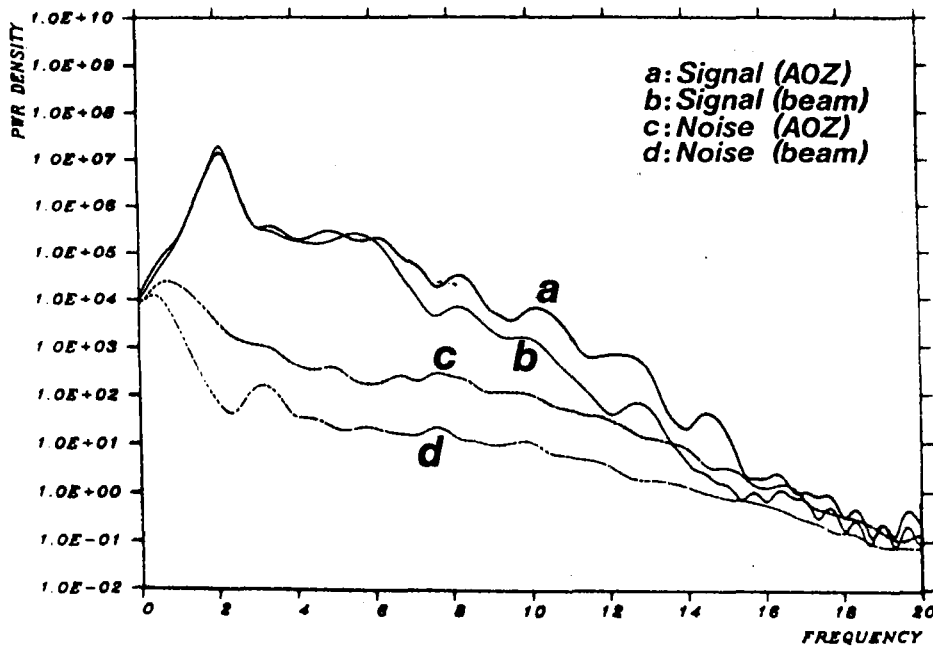


Fig. VII.5.3 Same as Fig. VII.5.1, but for Event 3 described in the text.

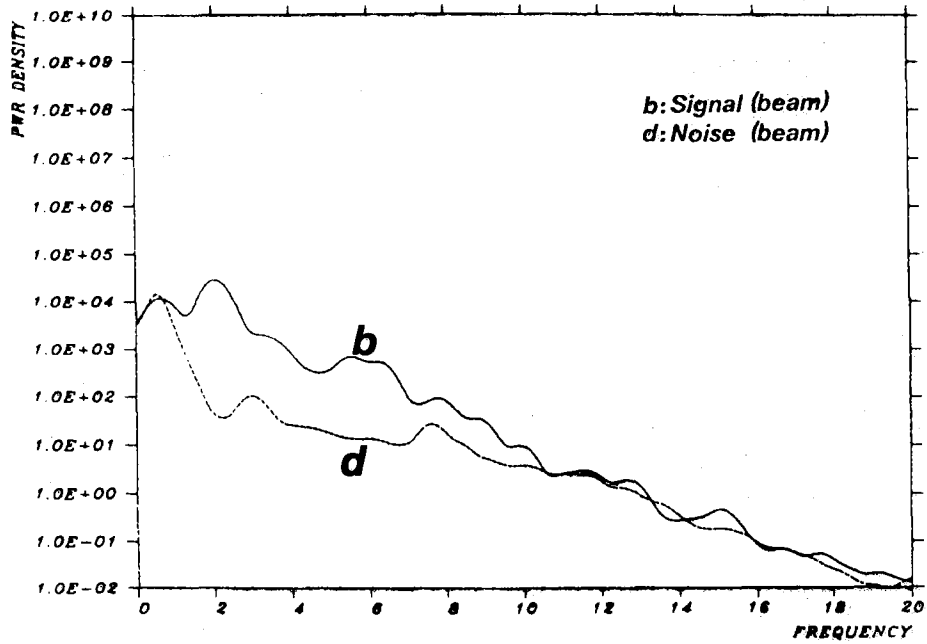
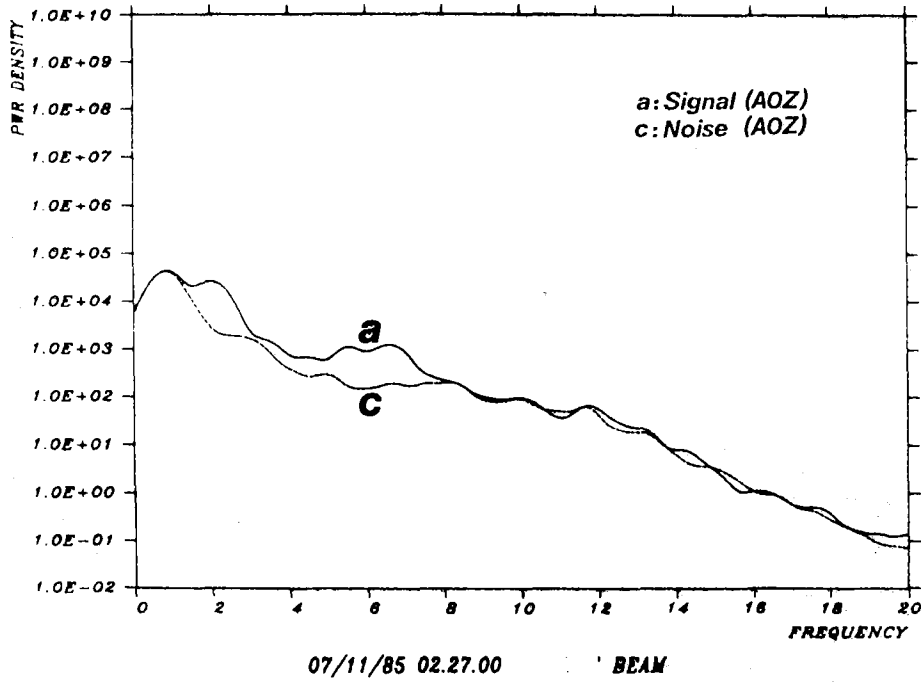
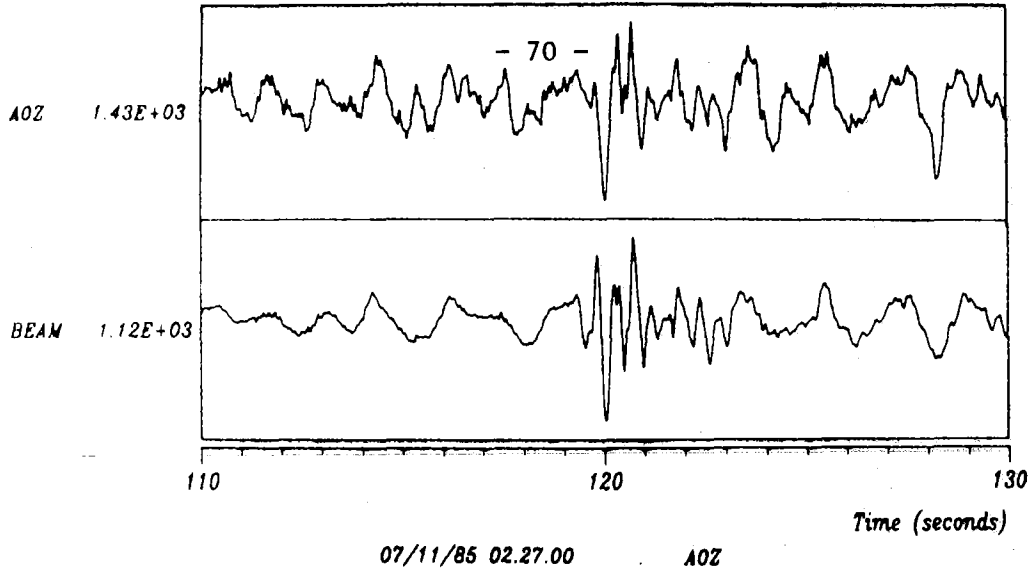


Fig. VII.5.4 Same as Fig. VII.5.1, but for Event 4 described in the text.

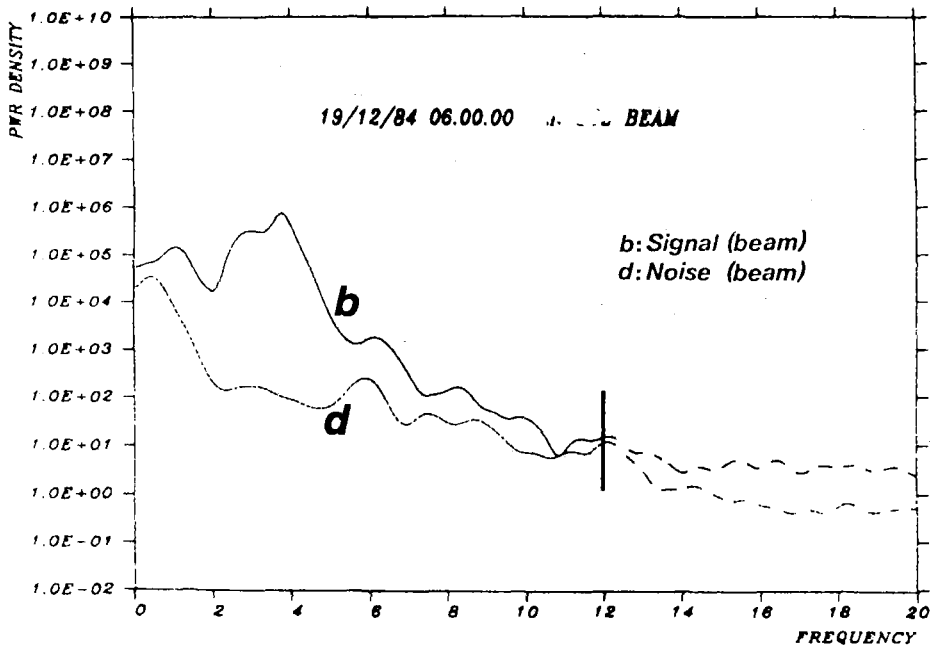
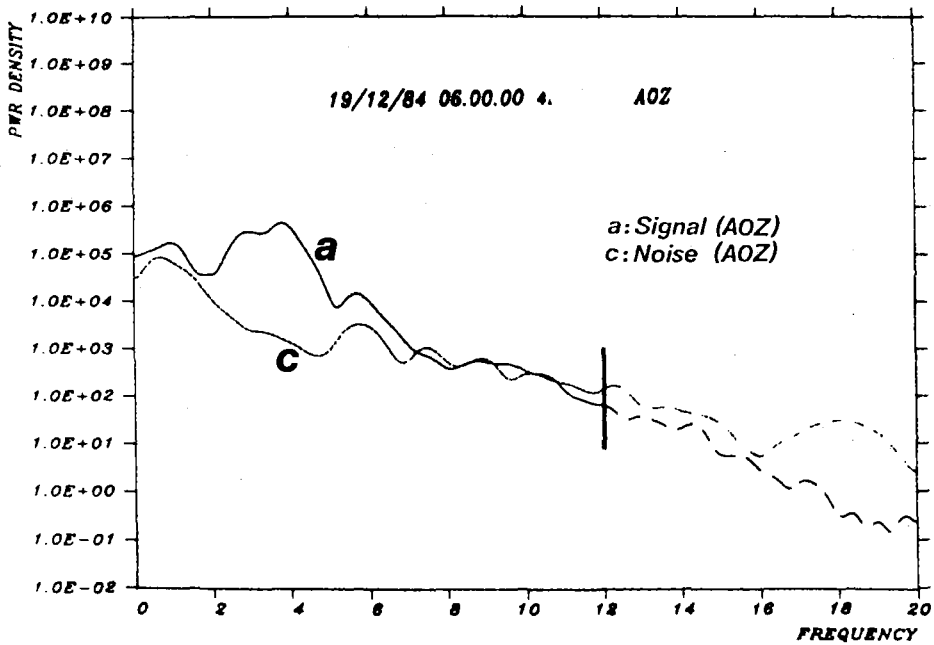
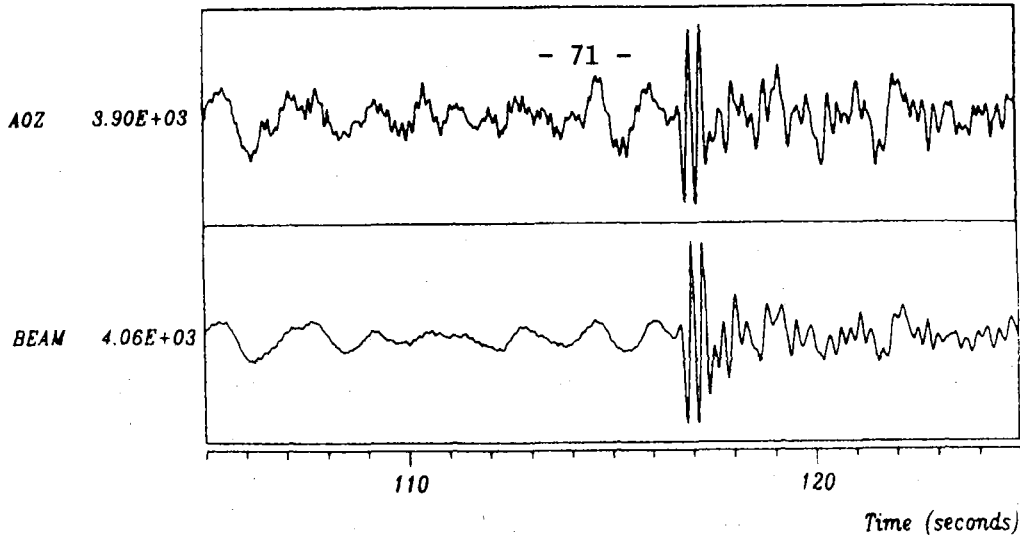


Fig. VII.5.5 Same as Fig. VII.5.1, but for Event 5 described in the text. Due to data problems, the spectra for this event are based on shorter time windows than Events 1-4, and the spectral estimates beyond 12 Hz are uncertain.

VII.6 The calculation of ellipticity corrections

For many purposes, including that of evaluating the performance of GDSN stations in source analysis studies, it is necessary to calculate synthetics, or Green's functions, in a spherically symmetric earth model (or a combination of such models), but with the effects of asphericity of structure included to first order. The effects are of primary significance to the travel times of waves, and the most conspicuous such effect is that due to ellipticity. Since the ellipticity correction is to be applied routinely to a variety of phases and for many source-receiver combinations, it is important that an effective computational method is available. Dziewonski and Gilbert (1976) obtained expressions for the ellipticity correction in the form of an integral over epicentral distance. On the other hand, the spherical travel times are usually evaluated much more efficiently as an integral over radius. First order perturbations in these travel times can be evaluated similarly; in fact, the ellipticity correction can be obtained as a by-product of the spherical travel time calculation.

The one-way spherical travel time of a ray between levels r_0 and r_1 can be expressed:

$$T = \int_{r_0}^{r_1} \frac{d(\eta^2 - p^2)^{\frac{1}{2}}}{1 - \eta v'} \quad (1)$$

where p is the ray parameter, $\eta = r/v$, and $v' = dv/dr$ in the spherical reference model. For a turning ray, r_0 is the turning point radius. Following Dziewonski and Gilbert (1976), if the asphericity is given by

$$\delta v(r, \theta, \phi) = -v'(r) \delta r(r, \theta, \phi)$$

and letting

$$\delta r(r, \theta, \phi)/r = \sigma(r, \theta, \phi)$$

the perturbation in T can be expressed:

$$\delta T = \int_{r_0}^{r_1} \eta v^1 \sigma \frac{d(\eta^2 - p^2)^{\frac{1}{2}}}{1 - \eta v'} \pm [\sigma(\eta^2 - p^2)^{\frac{1}{2}}]_{r_0}^{r_1} \quad (2)$$

where in the last term, +/- is to be taken for down-/upgoing waves. For a complete ray the last term is always cancelled by contributions from subsequent layers, unless r_0 or r_1 represents a velocity discontinuity or an end-point of the ray.

Numerically, T in eq. (1) is evaluated by interpolating v between r_0 and r_1 . For example, for $v = a(r/r_c)^b$:

$$T = \frac{1}{1-b} [(\eta^2 - p^2)^{\frac{1}{2}}]_{r_0}^{r_1} \quad (3)$$

Similarly, if we choose $(r_1 - r_0)$ sufficiently small so that σ can be averaged:

$$\delta T = \left(\frac{1}{2} \frac{b}{1-b} \pm 1 \right) [\sigma(\eta^2 - p^2)^{\frac{1}{2}}]_{r_0}^{r_1} \quad (4)$$

To substitute for σ we need the lateral position of the ray at r_1 and r_0 . This information can be obtained from the change in epicentral distance:

$$\Delta = \pm \frac{1}{1-b} [\cos^{-1}(p/\eta)] \frac{r_1}{r_0} \quad (5)$$

Further simplifications are possible if σ represents the ellipticity. As a check on the accuracy of the calculations we compared the results to tabulated results (Dziewonski and Gilbert, 1976), and Fig. VII.6.1 shows an example for surface focus S waves. Considering the difference in reference model and possibly in the values for ellipticity (we used the values of Bullen, 1975), the agreement is quite satisfactory.

D.J. Doornbos

References

- Bullen, K.E. (1975): The Earth's density. Chapman and Hall Ltd., London, pp. 420.
- Dziewonski, A.M. and Gilbert, F. (1976): The effect of small, aspherical perturbations on travel times and a re-examination of the corrections for ellipticity. Geophys. J. R. Astron. Soc., 44, 7-17.

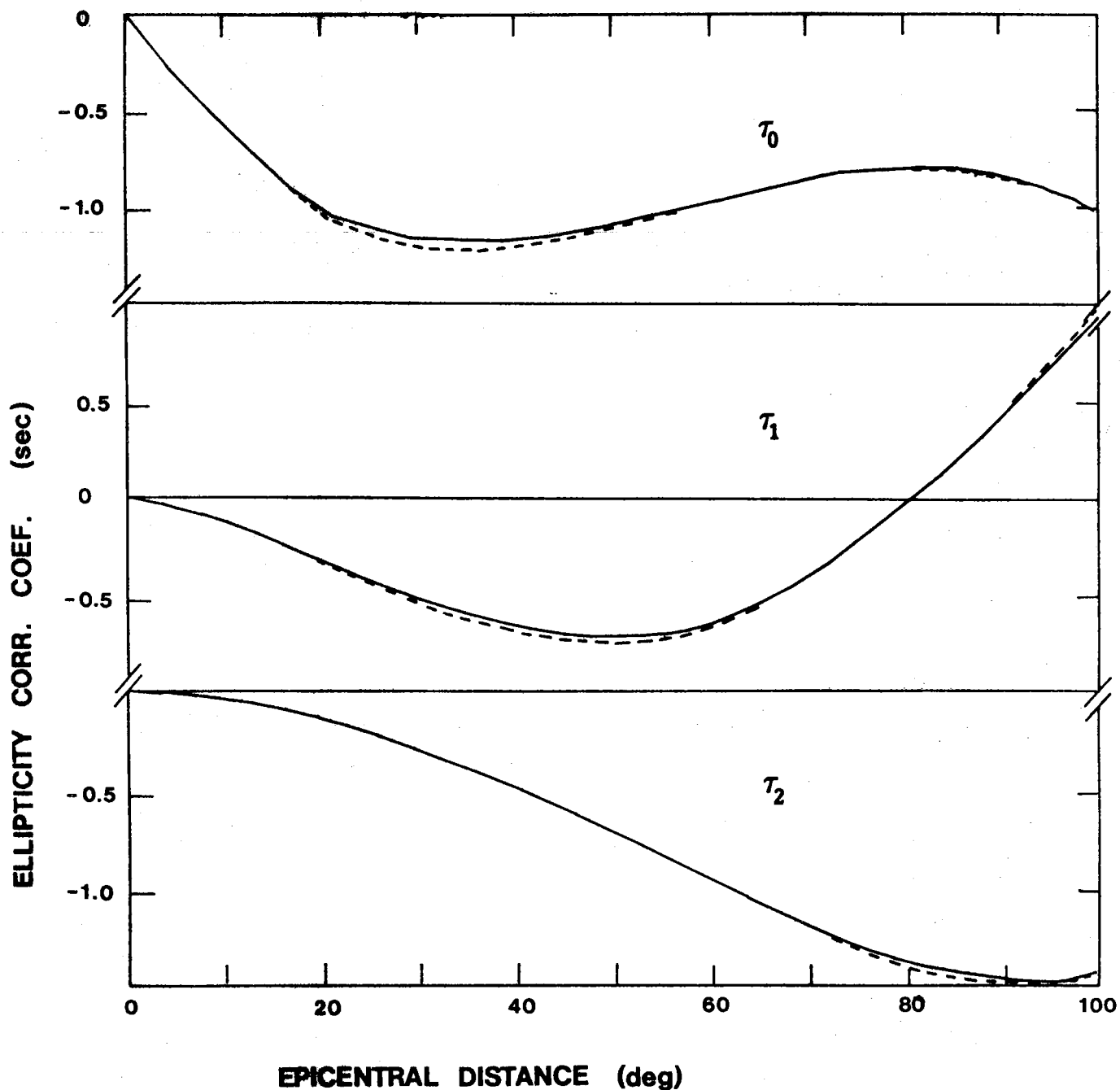


Fig. VII.6.1 Comparison of ellipticity correction coefficients for surface focus S phase
——: this study; - - - - -: Dziewonski and Gilbert (1976).

VII.7 Attenuation of seismic energy from local events in southern Norway

Seismic wave attenuation characteristics at local and regional distances in Norway and surrounding areas are known to be very dependent on the local geology, with rapid regional variations. Still, very few (if any) more extensive studies on this problem have been carried out in this region, and we therefore now report on a work aimed at analyzing how the quality factor Q appears in the southern Norway region.

Two different methods, the coda decay method and the method of spectral ratio, were tested out and applied to local events recorded within the region studied. In all cases the event-station distances were less than 300 km, and the depth of the events were in the range 0-35 km. Because observed Q in most other studies is found to depend strongly on frequency it is commonly expressed in the form $Q=Q_0*f^m$, where Q_0 is Q at a reference frequency (usually 1.0 hz), and m is a constant.

The use of the coda decay method to determine Q was first applied by Aki & Chouet (1975) and is in principle used to investigate how the coda energy from a local earthquake recording decays with time. The coda energy is thought to consist primarily of energy back-scattered from randomly distributed inhomogeneities and boundaries in crust, and a medium which generates coda well will then be less efficient as a wave transmitter. Theoretically, the coda is assumed to be described as a homogeneous pool of scattered energy covered in an ellipsoid with foci at the event's hypocenter and the station, and the measured decay of this energy with time will reflect Q within the ellipsoid. For different

scattering models it has been shown that the following simple relation describes the decay of coda energy with time:

$$A(f,t) = S(f) \cdot t^{-u} \cdot \exp(-\pi f t / Q(f))$$

Here $A(f,t)$ is the present coda amplitude, $S(f)$ the coda source factor, t the time measured from origin, and f is the frequency. The dispersion parameter u describes the type of spreading that occur, and is mostly given the value 1.0 which reflects scattered body-waves. Under the assumption that u is a constant and Q is a constant in each frequency band, Q can be found by linear least squares analysis for each fixed frequency f (see Fig. VII.7.1).

Another way to find Q directly from observations is to use the method of spectral ratio. This method is perhaps more known, and the way it is applied in this work is to see how the energy of direct body-waves decays between two stations with approximately equal azimuth relative to the source. By comparing the spectral contents of the direct waves recorded at the two stations, an estimate of the decay of energy as a function of frequency is obtained by linear least squares analysis (see Fig. VII.7.2). The estimated Q found using this method will describe the energy loss along the refracted wave-path of the primary waves and will therefore generally not describe the same volume as Q found from coda-waves.

The data used in this analysis are a selection of 19 local events recorded during 1982-83 by the temporary digital network of southern Norway (SNN) operated by NORSAR. Additionally, a selection of 14 local events recorded between January and March 1985 at the new Western Norway Network (WNN), which is operated by the Seismological Observatory in Bergen, were used. All stations were

short period vertical instruments, and the events used were relatively widely distributed south of 62 degrees north.

The coda decay method were applied to recordings from both networks, but the spectral ratio method could only be used for recordings from the SNN-network because the stations in the WNN-network were not calibrated at the time this work was carried out.

To ensure that only high-quality data were used in this analysis, only events with acceptable signal-to-noise ratio were included. Tests showed that the method of coda decay was very sensitive due to the noise level, but a noise level less than about 20% of the signal amplitude was not critical when calculating Q . This observation was then used as a criterion under selection of data. Fig. VII.7.1 shows some examples of chosen coda signals.

In most studies on this problem it is found that the quality factor Q increases with depth. This result was also found in this work in the way that coda Q seems to increase with increasing length of the investigated time window of data used. The increase in Q with window length is tied to the fact that the later parts of coda consists of energy back-scattered from deeper parts of the lithosphere (with higher Q). The observed coda Q did not turn out to differ significantly for subareas within the southern Norway region, and the averaged Q -values for the entire region were

Q-value	Corr. coeff.	No of obs.	Window (secs)
55*f ^{1.15}	0.93	50	20
75*f ^{1.15}	0.94	46	30
120*f ^{1.09}	0.92	46	40

The time window dependence for the spectral ratio method was not as critical as in the coda decay method. The chosen window length was 5 secs and was based on the experience that this length gave the most stable results. The spectral ratio method was applied to P- and S-waves separately and gave the following results:

Q-value	Waves	No of obs.	Q ₀	m
121*f ^{0.89}	P	17	121 ± 90	0.89 ± 0.3
127*f ^{1.08}	S	11	127 ± 70	1.08 ± 0.2

Some examples of the spectral ratio estimation of Q are shown in Fig. VII.7.2. It must be emphasized, however, that the results were rather scattered, and much more data would be needed to reduce the rather wide error limits.

The results indicate that Q for P-waves generally is lower than Q for S-waves within the region studied (see Fig. VII.7.3). Another interesting observation is that the Q-values for S-waves are quite similar to those obtained for coda-waves. This is shown explicitly for coda Q over a 40 secs time window. The fact that Q for coda waves in this window are almost identical to spectral ratio Q values for S-waves probably means that the coda primarily consists of S-waves, which also is observed in other regions, and

that coda in this window samples approximately the same part of crust as the direct S-waves.

The rate of frequency dependence of Q can be thought to give an indication of the amount and size of the scatterers that occur. A scattering model described by Dainty (1981) to explain the frequency dependence of Q showed that observed Q can be divided into two different mechanisms, intrinsic Q caused by the medium's deviation from complete elasticity, and scattering dependent Q caused by inhomogeneities the waves encounter during propagation. Intrinsic Q is in most works assumed to be relatively frequency independent, in which case the frequency dependence of observed Q must be mainly caused by scatterers or inhomogeneities in the crust. The apparent energy loss due to scattering will then be most critical for wave lengths comparable with the typical size of these scatterers, which in turn means that the attenuation of energy at low frequencies must be stronger than expected from intrinsic attenuation only. This is clearly shown if we compare the result found in this work with the result from Hasegawa (1985) for the Canadian Shield area (Fig VII.7.4). These two regions both represent old shield areas and should therefore not be too dissimilar geologically. It is seen from Fig. VII.7.4 that the frequency dependence of Q in southern Norway is much higher, but that Q for both areas seems to coincide for higher frequencies. This can be interpreted in terms of similar intrinsic Q in the two regions, but with more and stronger inhomogeneities in southern Norway.

Leif B. Kvamme
Jens Havskov (Univ. of Bergen)

References:

- Aki, K. & Chouet, B. (1975): Origin of coda waves: source, attenuation and scattering effects. *J. Geophys. Res.*, 80, 3322-3342.
- Dainty, A.M. (1981): A scattering model to explain seismic Q observations in the lithosphere between 1 and 30 Hz. *Geophys. Res. Lett.*, 8, 1126-1128.
- Hasegawa, H.S. (1985): Attenuation of Lg waves in the Canadian Shield. *Bull. Seism. Soc. Am.*, in press.
- Rovelli, A. (1984): Seismic Q for the lithosphere of the Montenegro region (Yugoslavia): Frequency, depth and time windowing effects. *Phys. Earth & Planet. Int.*, 34, 159-172.

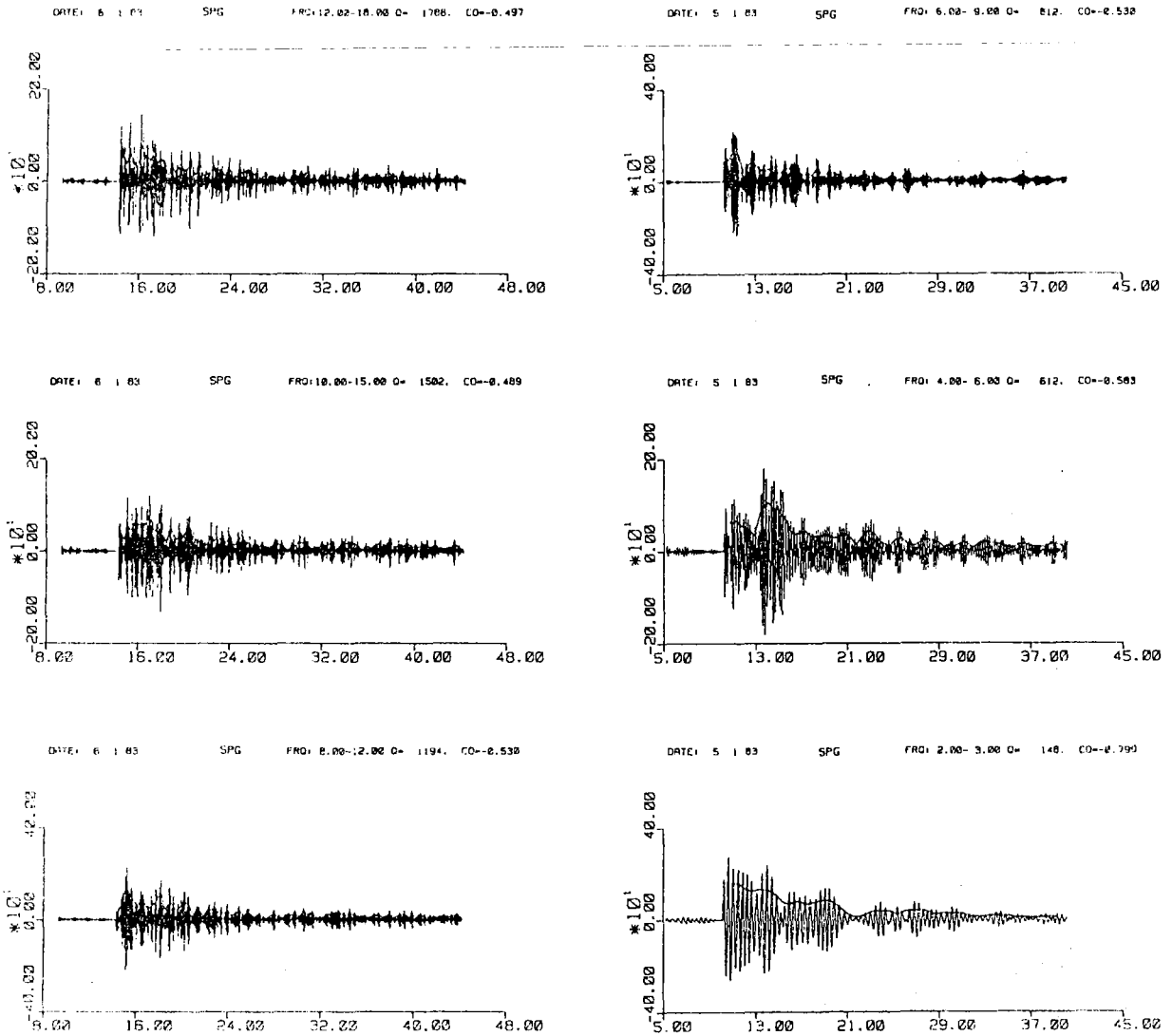


Fig VII.7.1 Examples of coda-recordings for one specific station band-pass filtered at different frequencies. The first part of the recordings indicate the noise level before P-wave arrival, and on top of the signals the RMS-envelope is drawn as an approximation to $A(f,t)$. Axes are time after origin versus amplitude.

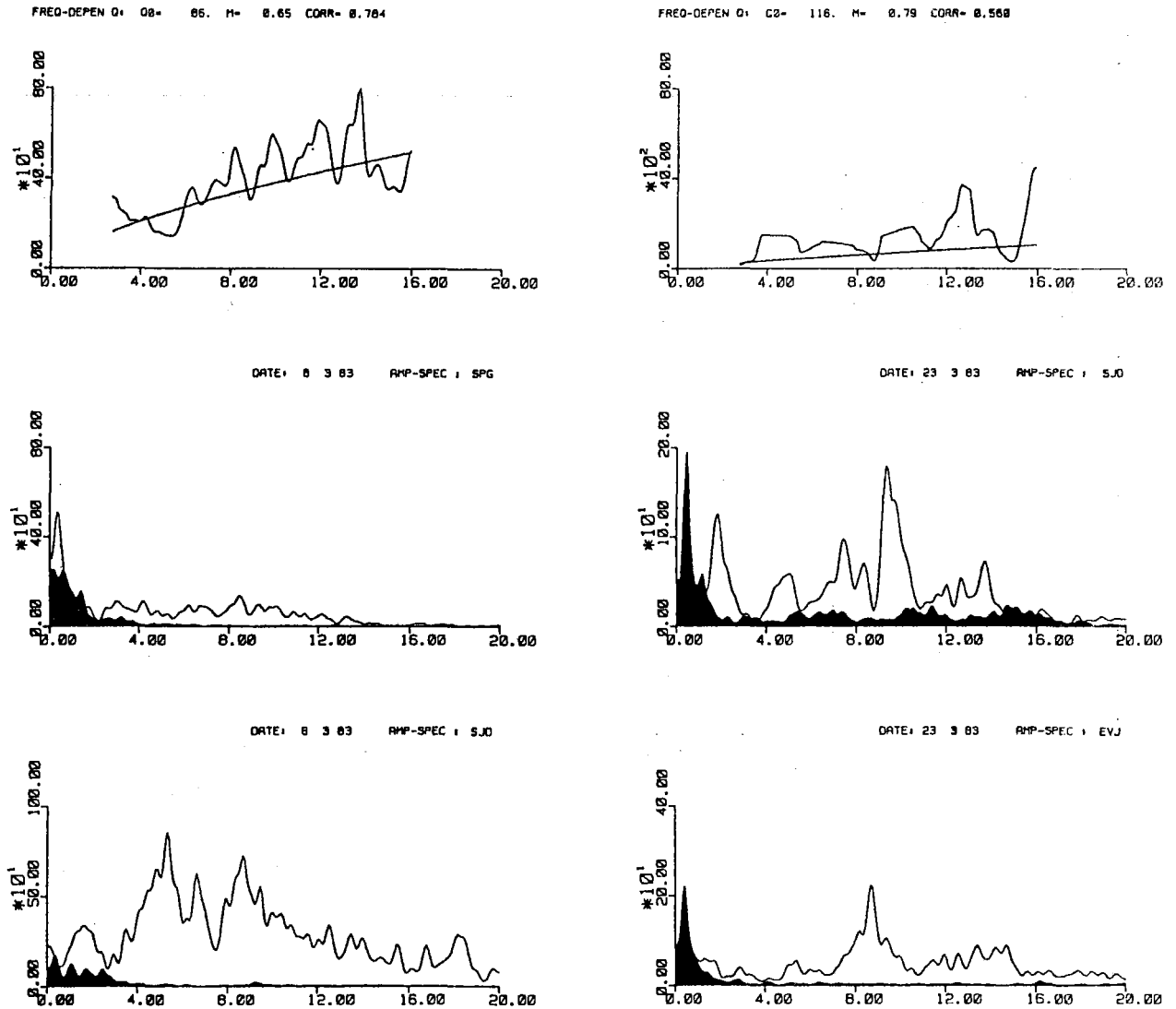


Fig. VII.7.2 Examples of spectral ratio estimation of Q for P-waves. On top the $Q(f)$ -functions of frequency obtained from spectral ratio analysis of the two below recorded amplitude spectra. The least squares lines show the curve of the best fit frequency dependent Q . The black zones on the amplitude spectra indicate the noise before P-wave arrival.

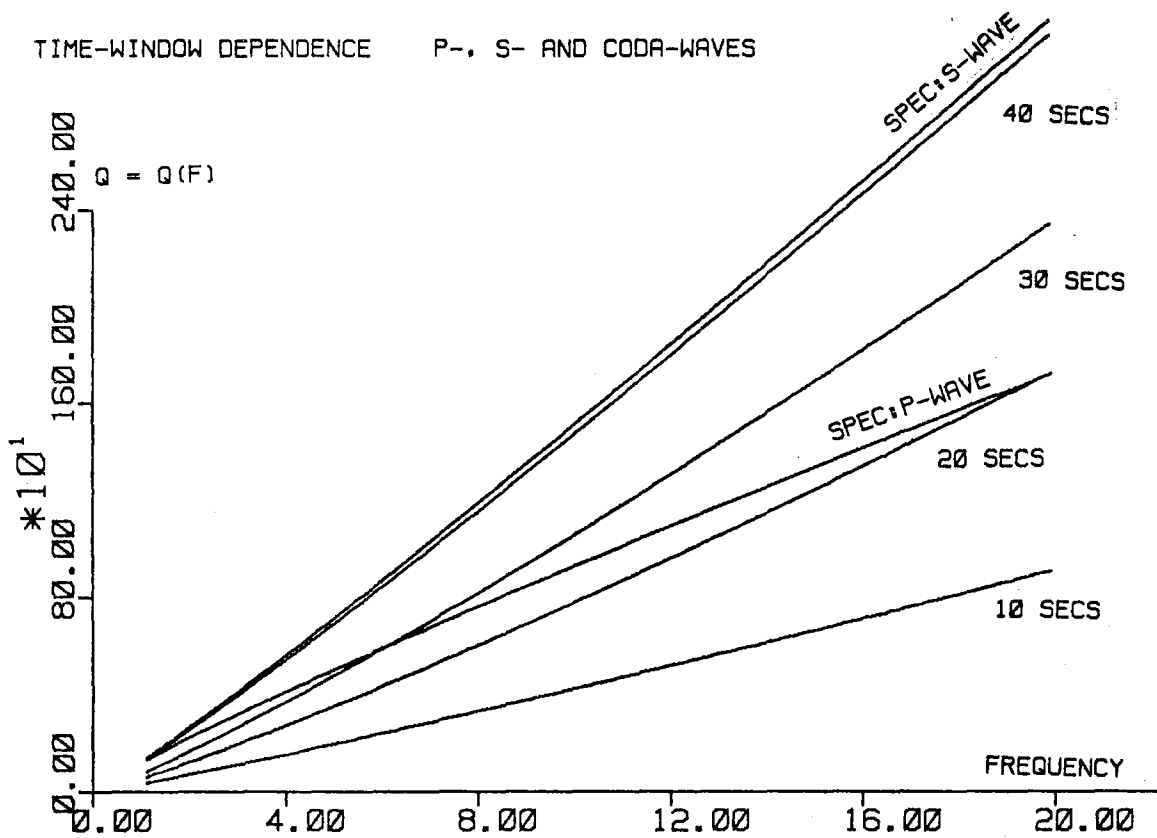


Fig. VII.7.3 Q as a function of frequency for both spectral ratio and coda-decay method. The figure shows coda Q for different time window lengths and Q for P- and S-waves using spectral ratio for a 5-second time window. Dispersion parameter u is fixed at $u = 1.0$, and data from both SNN- and WNN-networks are used.

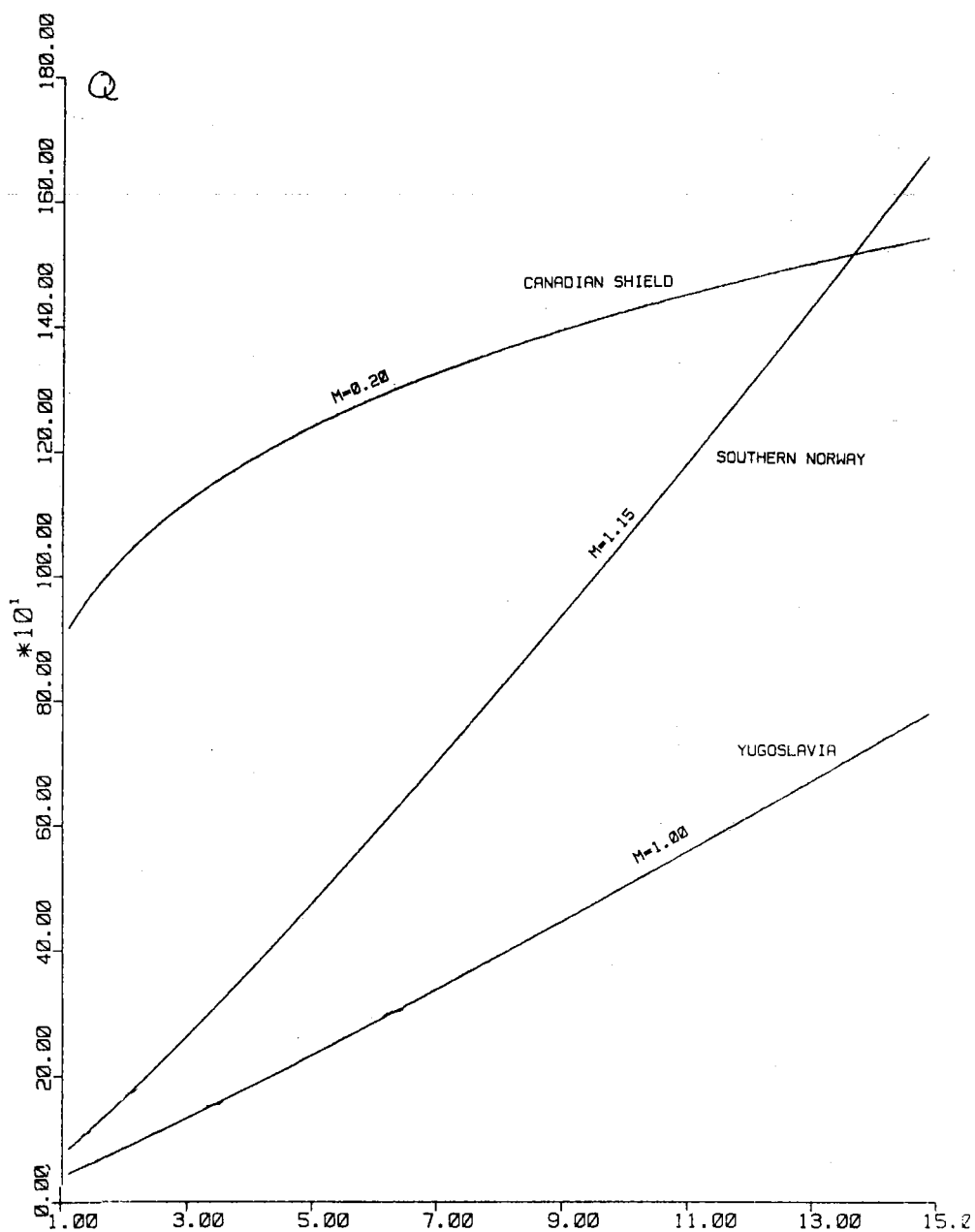


Fig. VII.7.4 Q as a function of frequency for different regions. The value of the scattering index m is shown on the figure. The curves intersect the vertical axis for 1 Hz at the value of the proportionality factor Q_0 .

VII.8 A new technique for 3-component seismogram analysis

The individual seismograph stations of global networks always include three-component instrumentation for the very simple reason that the seismic wavefield comprises both vertical and horizontal ground motions. Seismologists have for many years successfully exploited the information potential of three-component records for wave propagation modelling, retrieval of structural information (imaging) and source parameters, but these efforts have mainly been confined to the low frequency (less than 0.2 Hz) part of the wavefield. Much effort has been invested in extracting similar information in the high frequency band, say 1-10 Hz, but efforts generally have met with little success. The reason for this appears to be twofold:

- 1) High frequency records are rather complex due to scattering, mode conversions and multipathing.
- 2) The techniques of analysis often fail to produce wavefield parameters in an easily interpretable format. For example, a common procedure is to produce many particle-motion plots which generally are difficult to interpret.

In this section we present a new approach for extracting wavefield parameters, based on a priori models for P and S wave particle motions. Special attention has been given to the problem of presenting results in an easily interpretable manner for extracting signal parameters convenient for a wide variety of research applications. This has provided some remarkable results using data from the NORESS array, which were presented in the previous Semiannual Technical Summary (Christoffersson et al, 1985).

Structure of 3-component registrations

Both P and S waves exhibit a high degree of linear polarization. Ground particle motion coincides with the azimuth of propagation for the P phases. Surface waves of the Rayleigh type are generally elliptically polarized in the vertical-radial plane, the fundamental modes displaying retrograde particle motion and the higher modes prograde ellipticity. Surface Love waves are also found to be rectilinearly polarized, but in a horizontal plane orthogonal to the direction of wave propagation. Microseismic background is of the Rayleigh type, but with little preferred directionality. Signal-generated noise may also be polarized, although the direction of polarization is often random in nature. Using these various characteristics of polarized particle motion trajectories, we proceed in the following way:

Notations:

$$y(t) = [y_1(t), y_2(t), y_3(t)]^*$$

is the observed 3-component data vector where y_1 is the north component, y_2 the east and y_3 the vertical. The asterisk denotes the transpose.

$$z(t) = [z_1(t), z_2(t), \dots, z_k(t)]^*$$

is a k-dimensioned representation of the signal.

$$\Lambda = \begin{pmatrix} \lambda_{11} & \dots & \lambda_{1k} \\ \cdot & & \\ \cdot & & \\ \cdot & & \\ \lambda_{31} & & \lambda_{3k} \end{pmatrix}$$

is a matrix of unknown constants relating the signal to the observed 3-component data.

$$\varepsilon(t) = [\varepsilon_1(t), \varepsilon_2(t), \varepsilon_3(t)]^*$$

is the noise vector.

Model

We assume that the observed data vector $y(t)$ allows the following representation

$$y(t) = \Lambda z(t) + \varepsilon(t) \quad (1)$$

with the following basic assumptions:

- i) $z(t)$ and $\varepsilon(t)$ are orthogonal (uncorrelated)
- ii) $\varepsilon(t)$ has expectation zero
- iii) the components of $z(t)$ are linearly independent, i.e., the signal is k -dimensional
- iv) all moment up to at least second order exist.

From these assumptions it follows that the zero-lag second order moments of $y(t)$ can be written

$$\Sigma(t) = \Lambda \phi(t) \Lambda^* + \Psi(t) \quad (2)$$

$$\begin{aligned} \text{where } \Sigma(t) &= E [y(t) y(t)^*] \\ \phi(t) &= E [z(t) z(t)^*] \\ \Psi(t) &= E [\varepsilon(t) \varepsilon(t)^*] \end{aligned}$$

Integrating (or averaging in discrete time) eq. (2) over a time window $T_0 < t < T$ we obtain the following, second-order structure

$$\Sigma = \Lambda \phi \Lambda^* + \Psi \quad (3)$$

$$\Sigma = \int_{T_0}^T \Sigma(t) dt = \left[\begin{array}{c|c} 1 & \int_{T_0}^T \Sigma(t) dt \\ \hline T-T_0+1 & \end{array} \right]$$

$$\phi = \int_{T_0}^T \phi(t) dt = \left[\begin{array}{c|c} 1 & \int_{T_0}^T \phi(t) dt \\ \hline T-T_0+1 & \end{array} \right]$$

$$\Psi = \int_{T_0}^T \Psi(t) dt = \left[\begin{array}{c|c} 1 & \int_{T_0}^T \Psi(t) dt \\ \hline T-T_0+1 & \end{array} \right]$$

Eq. (3) is the ordinary factor analysis model.

Before discussing the estimation of the unknown parameters, usually based on the second order measurements, some details on the P and S wave representations will be given - at this time the surface wave representations are excluded.

Body wave representations

For P-waves the signal is 1-dimensional and will be written as:

$$\begin{aligned} y_1(t) &= \lambda_{11} z_1(t) + \varepsilon_1(t) \\ y_2(t) &= \lambda_{21} z_1(t) + \varepsilon_2(t) \\ y_3(t) &= \lambda_{31} z_1(t) + \varepsilon_3(t) \end{aligned} \quad (4)$$

In terms of the second order structure we have

$$\Lambda = \begin{Bmatrix} \lambda_{11} \\ \lambda_{21} \\ \lambda_{31} \end{Bmatrix} \quad \phi = \text{signal power} = (1 \times 1 \text{ matrix})$$

$\Psi =$ covariance matrix of the noise.

For P-waves the second order moments would be:

$$\Sigma_0 = \Lambda_p \phi_p \Lambda_p^* + \Psi \quad (5)$$

where (given rotated in z, T, R)

$$\Lambda_p = \begin{Bmatrix} \lambda_{11} \\ 0 \\ \lambda_{31} \end{Bmatrix} \quad \text{and} \quad \phi_0 = (\phi_{11})$$

and $\text{sgn}(\lambda_{11}) \neq \text{sgn}(\lambda_{31})$.

In the case of S-waves the signal is 2-dimensional, with SH and SV components.

$$\begin{aligned}
 y_1(t) &= \lambda_{11} z_1(t) + \lambda_{12} z_2(t) + \varepsilon_1(t) \\
 y_2(t) &= \lambda_{21} z_1(t) + \lambda_{22} z_2(t) + \varepsilon_2(t) \\
 y_3(t) &= 0 \cdot z_1(t) + \lambda_{32} z_2(t) + \varepsilon_3(t)
 \end{aligned}
 \tag{6}$$

where $z_1(t)$ is the SH component and $z_2(t)$ the SV component.

In terms of the second order structure we have

$$\Lambda = \begin{bmatrix} \lambda_{11} & \lambda_{12} \\ \lambda_{21} & \lambda_{22} \\ 0 & \lambda_{32} \end{bmatrix} \quad \text{and} \quad \phi = \begin{bmatrix} \text{power of SH} & 0 \\ 0 & \text{power of SV} \end{bmatrix}$$

with the columns of z being orthogonal.

In this case, the second order moments would be:

$$\Sigma_S = \Lambda_S \phi_S \Lambda_S^* + \Psi \tag{7}$$

where (given rotated z , T, R)

$$\Lambda_S = \begin{pmatrix} 0 & \lambda_{12} \\ \lambda_{21} & 0 \\ 0 & \lambda_{32} \end{pmatrix} \quad \text{and} \quad \phi_S = \begin{pmatrix} \phi_{11} & 0 \\ 0 & \phi_{22} \end{pmatrix}$$

and $\text{sgn}(\lambda_{12}) = \text{sgn}(\lambda_{32})$.

The first column in Λ_S is the SH component with signal power ϕ_{11} , the second is the SV component with signal power ϕ_{22} .

Estimation

For a 3-component station, the Σ 's in eqs. (5) and (7) are symmetric 3x3 matrices having at most 6 different elements. In order to make the covariance structures identified, we can have at most

6 unknown parameters in Λ , ϕ and Ψ , so we must introduce some restrictions. Firstly, we will normalize the non-zero element in the ϕ -matrices to be equal to 1 which is actually not a restriction. Secondly, we assume that the Ψ -matrix is diagonal, i.e., the noise is assumed to have no zero-lag correlation. Further, in some cases we will use the additional restriction that Ψ is proportional to some known diagonal matrix Ψ_0 , i.e., $\Psi = \theta \Psi_0$.

The estimation of the unknown parameters will be based on the observed second order moment of the observations over a time window

$$S = \frac{1}{T-T_0+1} \sum_{t=T_0}^T y(t) t(t)^* \quad (8)$$

There are several possible estimators that can be used. Most are based on some fitting function, i.e., minimizing the difference between the observed S and the theoretical Σ .

The most commonly used are

i) ML (MAXIMUM LIKELIHOOD)

This estimator is derived from Gaussian assumptions and minimizes:

$$F = \log |\Sigma| + \text{tr}(S\Sigma^{-1}) - \log |S| - q \quad (9)$$

where q is the dimension of the data (in this case $q=3$), and tr = the trace operator.

ii) ULS (UNWEIGHTED LEAST SQUARES)

This estimator minimizes:

$$F = \text{tr}(S-\Sigma)^2 \quad (10)$$

i.e., the sum of squares of all the elements in $S-\Sigma$.

iii) GLS (GENERALIZED LEAST SQUARES)

This estimator minimizes:

$$F = \text{tr}(I-S^{-1}\Sigma)^2 \quad (11)$$

iv) PC (PRINCIPAL COMPONENT)

This estimator maximizes, subject to normalizing conditions on Λ :

$$F = \text{tr}(\Lambda^*SA) \quad (12)$$

Properties of estimators

The PC estimator leads to an eigenvalue decomposition of the observed moment matrix S and was suggested by Husebye et al (1967). It differs from the other three mainly in that it focuses heavily on the diagonal of S whereas the other put more weight on the off-diagonal. Under Gaussian's assumption, the ML and GLS estimates are asymptotically equivalent and it is possible to obtain a statistical test for the model fit to data. ML and GLS need a positive definite S -matrix, whereas ULS works even with non-grammian S . This property would point in favor of ULS because for strong and clear P-waves much above ground noise, the observed S -

matrix will often be near singular. However, this problem can be overcome by attenuating the transverse component, i.e., by adding white noise. We will therefore use the ML estimator, mainly because of its possibility for model tests. These are of course strictly valid only under the Gaussian assumptions. However, as has been demonstrated in the applications, the tests can be modified to work well in practice.

Model test

Under the assumption of independent observations and Gaussian distribution, model tests can be carried out based on the ML estimator. We have approximately that

$$(N^+ - 1) \cdot F \quad \text{with } N^+ = (T - T_0 + 1) \quad (13)$$

is distributed as chi-square with degrees of freedom equal to $q(q+1)/2$ - number of unknown parameters. Test for the P-wave can then be constructed in the following way:

We assume that $\Psi = \phi^2 I$. Let F_N and F_P denote the minimum of the fitting functions for the Noise and P models, respectively, using ML.

Then $(N^+ - 1)F_N$ is approximately chi-square with 5 d.f., $(N^+ - 1)F_P$ approximately chi-square with 3 d.f., and the difference $(N^+ - 1)(F_N - F_P)$ is chi-square with 2 d.f. Now, if data really are noise with $\Psi = \phi^2 I$, both the Noise and the P model would have reasonable fit to data and the drop in chi-square, i.e., $(N^+ - 1)(F_N - F_P)$ would not be significant.

For data generated by a P-wave, on the other hand, the noise model would have poor fit, the drop in chi-square would be significant and the P model would have good fit to data.

Define

$$\begin{aligned} P(P) &= \text{Probability } \chi^2(3) > (N^*-1) F_P \\ P(N) &= \text{ " } \chi^2(5) > (N^*-1) F_N \\ P(D) &= \text{ " } \chi^2(2) > (N^*-1) (F_P - F_N) \end{aligned} \quad (14)$$

We then use

$$P(P) \cdot P(PE>0) = P(P)(1-P(D)) \quad (15)$$

i.e., the "probability of a P-wave multiplied with the probability of the P energy being larger than zero".

This measure is rather sensitive to deviation from the Gaussian and independent assumptions. Also, for large N it is sensitive in the sense that small deviations from the P-wave model will easily be detected. This problem can be solved by multiplying N^+ with a constant $C(0<C<1)$, the size of which depends on the sampling rate and frequency. The actual value of C can be determined such that $P(P) \cdot P(PE>0)$ is small for noise data and large for data containing P signals. Similar tests can easily be determined for S-, R- and L-waves.

Concluding remarks

The 3-component analysis techniques as described above have been tested on a large variety of seismic recordings and a few examples here will be mentioned. For the broadband records of the recent large Mexican earthquake (unfiltered) at HRV (Harvard, Mass., USA) we easily identified phase arrivals like P, PP, PPP,

PcP, ScP and S. The corresponding azimuth estimates deviated only around ± 2 deg from the true ones - thus, from a single 3-component station record, a good initial epicenter estimate is feasible. Very many NORESS records have also been analyzed, and for teleseismic events adequate estimates of the slowness-vector are obtainable. In the extreme, deterministic scattering contributions in the P-wave coda have been identified. Our 3-component analysis techniques also work quite well, particularly for P-wave motion, for vertical seismic profiling (VSP) records where dominant signal frequencies typically are 50-100 Hz.

Another feature of this technique is tht it works quite well for weak signals, which is not exactly surprising as here we exploit the wavefield structure in contrast to stacking techniques where signal power variations over the earth's surface are used. One drawback with our 3-comp. analysis is pure noise triggering, which is attributed to some P-wave energy in the background noise; the so-called whispering mantle effect. Therefore, in an on-line event detection context 3-comp. triggering has to be weighted by signal power estimates say on the vertical component before event presence is declared.

Finally, we consider that 3-comp. analysis should be potentially very useful in an "expert system" context (e.g., see Chen, 1983), as in this way a systematic wavefield decomposition is feasible

even at relatively low SNRs, whereas conventional "signal power" techniques like spectral and f-k analysis become inefficient.

A. Christoffersson
(Uppsala Univ.)
E.S. Husebye
S.F. Ingate (MIT)

References

- Chen, C.H. (ed.) (1984): Seismic signal analysis and discrimination III; *Geoexploration*, 23, 1-170.
- Christoffersson, A., E.S. Husebye & S.F. Ingate (1985): 3-component seismogram analysis, Semiannual Technical Summary, 1 Oct 84 - 31 Mar 85, NORSAR, Kjeller, Norway.
- Husebye, E.S., A. Christoffersson & C.W. Frasier (1975): Orthogonal representation of array-recorded short period P-waves, IN: *Exploitation of Seismograph Networks*, K.G. Beauchamp (ed.), Noordhoff Int. Publ. Co., The Netherlands.

VII.9 NORESS regional event records - wavefield decomposition schemes

The high-quality NORESS recordings of events at local and regional distances exhibit many complex features the significance of which is difficult to assess by visual inspections of the records. What is needed here is fast and robust analyzing schemes for phase-type identification, and estimates of the associated slowness vector. An added advantage would be if the above information or part of it can be used for time-domain filtering of the original records so as to visually expose major features. The ability to extract significantly more information from local and regional event records is essential for more advanced seismogram analysis like forward and inverse modelling and not at least expert system designs. In this context we have conducted a practical analysis experiment on NORESS records of local and regional events, using different techniques, namely, f-k, semblance and the novel 3-comp. analysis technique described in subsection VII.8.

f-k analysis

Our interest here is to have a computationally fast, sliding window approach, and the necessary details here are as follows: Consider an array of N-sensors whose locations are r_j ; $j=1, N$. For a prespecified time window of the records, the respective Fourier transforms are $C_j(\omega)$. The corresponding frequency-wavenumber (f-k) spectrum is defined as

$$P(\omega, \bar{k}) = \sum_{j=1}^N \sum_{l=1}^N S_{jl}(\omega) \exp(i\bar{k}(\bar{r}_j - \bar{r}_l)) \quad (1)$$

where S_{j1} is the cross-spectrum between the j -th and 1 -th instruments. Since $S_{j1}(\omega) = C_j(\omega) \cdot C_1^*(\omega)$, eq. (1) may be rewritten as

$$\begin{aligned} P(\omega, \bar{k}) &= \sum_{j=1}^N \sum_{l=1}^N C_j(\omega) C_l^*(\omega) \exp(i(\bar{k} \cdot \bar{r}_j)) \exp(-i(\bar{k} \cdot \bar{r}_l)) \\ &= \sum_{j=1}^N C_j(\omega) \exp(i(\bar{k} \cdot \bar{r}_j)) \cdot \sum_{l=1}^N C_l^*(\omega) \cdot [\exp(-i(\bar{k} \cdot \bar{r}_l))] \\ &= \left| \sum_{j=1}^N C_j(\omega) \exp(i(\bar{k} \cdot \bar{r}_j)) \right|^2 \end{aligned}$$

which only involves a single summation. This technique for $P(\omega, k)$ -estimation was first proposed by Flinn and Smart (1971). Additional speed-up in programming is obtained by using properties of the exponential function to eliminate indexing during power component summation and by using the "sum of angles" formula for sine and cosine terms when estimating the Fourier spectrum $C_j(\omega)$. Frequency domain smoothing was performed by a Hanning operation, i.e., replacing $C_j(\omega)$ by

$$\frac{1}{4} C_j(\omega_1) + \frac{1}{2} C_j(\omega) + \frac{1}{4} C_j(\omega_2)$$

ω_1, ω_2 being $\omega \pm .5$ Hz) during the initial spectrum estimation.

Comments: f-k analysis, including its ML variants, is generally not rated a robust analyzing technique for several reasons. In ML estimation the signal is presumed non-stochastic, which is not necessarily the case in shorter time windows, while for conventional f-k relatively long time windows are needed ($T > 1.6$ sec) to ensure a good Fourier spectrum estimate. Perhaps the most intriguing aspect of f-k analysis is that in most applications, the slowness estimate extracted is tied to peak power in the f-k space. Under adverse conditions with interfering wavelets, peak power is not always associated with the "primary" phase and thus wild slowness estimates may ensue. Let us add that under more normal conditions, conventional f-k analysis represents in many respects a convenient tool for seismogram decomposition.

Semblance

So-called semblance analysis is in many respects similar to VESPAGRAM analysis, and as such is of potential interest in processing of regional NORESS records. The semblance parameter S_t , essentially the normalized beam power over a given window $2\Delta T$ and for a given slowness, is defined as:

$$S_t = \frac{\sum_{p=t-\Delta T}^{t+\Delta T} \left(\sum_{i=1}^N x(p)_i \right)^2}{N \sum_{p=t-\Delta T}^{t+\Delta T} \left(\sum_{i=1}^N x(p)_i \right)^2} \quad (3)$$

The S_t parameter is a simple signal coherency measure which appears to provide reasonable phase velocity estimates even for complex local and regional event records. Besides its calculational simplicity, an added advantage is that the semblance technique works well even for short time windows of the order of .5

sec. In practical use the looping over the P and S crustal velocity window, say $3-10 \text{ kms}^{-1}$ for a given azimuth and signal window width. We may also loop over azimuth for obtaining a more refined velocity-azimuth estimate for dominant phases in the record.

3-comp. signal analysis

The theoretical basis for this technique is described in subsection VII.8, so here we will only comment on the practical usage of this technique. The output from the 3-comp. analysis (single site) is probability of P, S-, Rayleigh and Love-waves in the records as a function of time and azimuth. Since this technique embodies the estimation of the principal axis of the particle motion ellipsoid, it is easy to estimate also the apparent angle of incidence for an incoming phase. This parameter can in turn be converted to apparent velocity and henceforth epicentral distance via standard travel time tables. The error in the corresponding azimuth and velocity estimates are of the order of $\pm 15 \text{ deg}$ and $\pm 3 \text{ kms}^{-1}$. Important, most of the observed deviations are deterministic, that is, due to structural effects and thus to a large extent can be removed by appropriate corrections in the same way as done for arrays.

The advantages with the novel 3-comp. analysis is that it provides an efficient means for decomposition of even complex wavetrains, can operate on short time windows of the order of 0.5-1.0 sec and provides good estimates of the slowness vector. A drawback is easy triggering on noise wavelets which we consider removable by appropriate filtering schemes.

Practical examples:

The relative merits of the 3 analysis methods discussed above have been tested on real data and detailed results for a presumed explosion near Leningrad (Date: 29 Jan 85; OT: 11.59.47; Lat. & Long.: 59.3N, 28.1E) are presented below in Figs. VII.9.1-6 and Tables VII.9.1-3.

All the figures have the same time scale and thus are easily comparable. The main features are summarized in the figure captions.

In Tables VII.9.1-3 the outputs from f-k, semblance and 3-comp. analysis are presented in detail. All three methods give reasonable velocity and azimuth estimates of the first part of the P-wave train (centered around $t = 126$ sec), although the semblance results by far appear to be the most robust ones. Interestingly, the single 3-comp. station analysis results contain all principal phase information features as found in the semblance and f-k results plus some more, most of which is termed coda signature of the event in question. Also, the 3-comp. analysis results are rather stable when based on beam traces formed from the 4 NORESS stations in question. For the shear wave section we have not run the Love and Rayleigh models of our 3-comp. analysis package.

Comments: The results presented are rather self-evident, so we will only remark that the advantage of f-k is scanning of the whole "space", but that in more extreme cases the associated (peak power) slowness estimate could be very wrong. Semblance is robust and provides adequate slowness estimates, but for easy use in an automated mode require a priori information on azimuth. Furthermore, semblance function values are convenient for generating

weighting filters in the same way as used in 3-comp. analysis (Fig. VII.9.5). Finally, the 3-comp. results do not compare unfavorably with those obtained from f-k and semblance analysis using whole array recordings. It also seems to work well for signals with poor SNR as demonstrated elsewhere.

T. Egilson
E.S. Husebye
B.O. Ruud

References

Flinn, E.S. & E. Smart (1971): Fast frequency-wavenumber analysis and Fisher signal detection in real-time infrasonic array data processing, Geophys. J.R. Astr. Soc., 26, 279-284.

ANALYSIS FREQUENCY :

3.2

WINDOWS :	1.00			1.50			2.00		
TIME	POWER	AZIM	VELO	POWER	AZIM	VELO	POWER	AZIM	VELO
120.00	39.3	0.73	6.15	40.6	0.73	6.15	42.6	240.95	47.20
120.50	36.7	83.75	10.40	37.1	86.01	11.27	37.1	263.16	19.30
121.00	38.1	126.47	16.99	39.2	103.57	16.29	41.6	292.38	26.43
121.50	36.7	225.72	4.30	37.9	225.73	4.41	44.3	188.13	13.75
122.00	37.2	228.95	11.82	39.5	222.80	13.21	42.7	232.59	22.71
122.50	34.7	221.82	19.06	32.3	1.74	14.72	41.3	131.13	4.63
123.00	34.6	250.18	11.06	36.4	259.99	9.38	37.9	129.45	4.75
123.50	38.2	78.59	19.06	38.7	120.96	27.78	38.5	234.46	18.83
124.00	39.2	147.53	37.27	39.8	201.04	34.89	43.9	225.00	18.09
124.50	36.6	245.73	8.69	36.2	133.51	4.46	53.2	83.05	11.77
125.00	37.2	265.26	14.21	37.2	102.99	12.14	56.4	78.69	10.59
125.50	32.8	299.05	9.44	33.3	110.10	11.13	55.8	80.75	11.16
126.00	51.9	80.31	11.66	51.0	77.62	11.58	57.0	76.33	12.76
126.50	56.3	83.66	10.73	55.7	81.16	10.67	59.6	78.69	10.59
127.00	56.3	80.75	11.16	56.2	93.37	11.23	56.2	76.26	10.49
127.50	53.7	77.01	12.14	53.4	79.82	12.27	55.2	74.25	11.99
128.00	51.5	75.65	10.95	51.2	75.65	10.95	52.5	69.30	10.10
128.50	41.9	292.56	6.90	42.2	291.64	7.17	44.9	294.59	7.49
129.00	43.0	231.01	6.00	42.0	231.88	5.68	50.0	99.16	15.48
129.50	42.0	90.78	6.66	43.1	90.78	6.66	48.2	124.88	12.08
130.00	42.0	162.76	16.01	43.6	145.62	21.11	49.0	156.25	17.79
130.50	46.2	83.66	10.73	45.5	83.37	11.23	48.4	86.88	8.82
131.00	44.8	107.78	8.73	44.9	109.13	9.37	47.2	123.16	5.42
131.50	43.1	88.45	13.13	43.7	88.45	13.13	44.2	74.36	18.72
132.00	44.5	81.87	13.75	43.4	79.29	12.91	47.5	96.34	17.89
132.50	42.1	125.54	18.83	43.9	119.48	18.40	46.9	86.63	28.54
133.00	43.8	84.17	9.87	44.3	86.19	10.78	51.5	78.69	10.59
133.50	41.0	83.85	7.43	41.4	86.99	8.51	47.0	76.70	8.60
134.00	40.6	81.53	10.23	38.5	76.83	10.07	45.5	80.36	9.04
134.50	45.3	79.16	10.16	45.7	79.16	10.16	49.4	84.99	8.49
135.00	41.7	78.18	11.06	41.9	71.57	11.82	43.9	330.52	18.40
135.50	41.8	86.99	8.51	41.1	84.99	8.49	44.3	85.86	7.03
136.00	42.9	102.77	6.32	43.1	104.89	5.95	47.2	168.69	95.31
136.50	43.1	50.44	16.29	43.1	47.39	14.31	45.5	141.71	20.08
137.00	38.6	92.17	6.15	39.0	135.00	11.09	45.7	90.88	7.48
137.50	43.2	107.78	3.73	43.3	111.19	9.25	45.8	109.06	8.35
138.00	44.6	71.57	17.08	45.3	77.28	15.29	50.7	98.84	10.67
138.50	43.9	105.46	9.97	44.3	109.23	10.67	45.0	89.92	9.17
139.00	39.7	120.96	27.78	41.3	130.91	24.48	44.2	103.67	12.76
139.50	40.7	118.50	12.20	39.0	137.39	14.31	40.6	155.92	9.44
140.00	39.0	94.64	13.09	38.5	107.45	13.25	48.4	135.00	68.73
140.50	37.3	92.64	7.47	39.3	240.95	47.20	39.5	42.40	5.20
141.00	41.4	100.98	7.12	41.1	103.47	6.66	43.7	78.69	7.33
141.50	41.4	132.92	6.24	41.3	128.95	5.18	43.2	117.47	17.25
142.00	38.6	123.36	5.11	38.5	125.81	4.99	47.1	106.43	153.69
142.50	40.5	304.00	9.37	39.7	261.87	68.73	46.4	84.81	8.80
143.00	43.3	135.00	10.41	42.7	133.32	10.10	45.0	113.55	11.42
143.50	40.1	72.05	6.51	38.9	71.10	6.30	42.5	71.57	153.69
144.00	42.1	258.02	14.41	42.5	253.81	15.06	43.4	274.18	11.82
144.50	43.7	102.72	15.29	44.3	102.72	15.29	44.5	120.38	14.46
145.00	42.8	55.30	30.74	42.5	346.61	22.51	46.2	306.57	12.59
145.50	41.4	152.35	20.50	41.4	138.18	19.06	47.1	115.56	19.06
146.00	41.3	107.05	6.20	41.1	107.05	6.20	45.7	164.74	14.21
146.50	39.9	104.24	7.03	39.3	107.56	5.87	40.3	246.16	10.34
147.00	39.3	59.38	8.54	40.7	59.04	9.26	40.1	262.48	9.09
147.50	39.0	260.31	11.68	39.6	266.19	10.78	41.4	106.05	6.40
148.00	40.5	207.35	14.89	41.7	218.42	13.13	43.0	220.49	9.02
148.50	38.8	15.23	5.91	39.9	16.23	5.91	48.0	109.00	7.53
149.00	39.3	243.43	10.51	40.4	246.45	11.42	45.5	69.78	24.00
149.50	39.2	227.96	5.92	40.3	225.99	5.92	43.5	69.90	11.13
150.00	46.3	105.57	7.57	45.7	108.43	7.32	45.7	108.43	7.32

Table VII.9.1a Output of "sliding" window f-k analysis for signal "center" frequency $f_0=3.2$ Hz and whole NORESS array except A-ring. Three different window lengths are used, namely: 1.0, 1.5 and 2.0 sec. Other values of f_0 gave less consistent results vis-à-vis "true" velocity and azimuth at 8.38 kms^{-1} and 92.60 deg. A comparison with semblance results in Table VII.9.2 clearly implies why semblance is termed a robust analysis technique re f-k.

FK-ANALYSIS WITH SLIDING TIMEWINDOW

DATA FILE : NRS85029 11894002

 ANALYSED FREQUENCY : 3.20

WINDOWS :	1.50			2.00			2.50		
TIME	POWER	AZIM	VELO	POWER	AZIM	VELO	POWER	AZIM	VELO
210.00	38.1	99.34	3.04	40.6	0.91	3.86	42.0	3.24	4.58
210.50	37.7	74.36	9.36	41.2	131.13	2.32	45.8	55.62	10.56
211.00	38.3	225.00	5.93	43.0	111.57	5.26	47.7	107.45	6.62
211.50	41.0	101.82	5.53	45.1	105.02	5.72	47.4	96.53	5.61
212.00	36.7	311.70	3.30	40.9	79.51	8.85	46.2	112.01	4.79
212.50	40.1	87.71	9.71	46.3	115.02	4.89	49.5	112.89	4.97
213.00	38.6	87.88	8.99	45.0	96.84	9.65	48.9	109.54	7.39
213.50	37.9	20.22	12.00	45.0	102.99	8.07	48.0	105.26	7.10
214.00	42.1	112.89	4.97	42.3	337.83	8.33	42.9	336.25	8.90
214.50	39.1	130.43	6.85	41.7	137.60	7.80	43.0	137.60	7.80
215.00	44.1	107.45	6.62	43.7	114.15	7.65	44.0	234.95	2.97
215.50	37.5	138.51	4.52	42.0	113.75	8.90	47.7	96.34	3.85
216.00	36.8	239.04	13.89	42.2	91.40	5.93	45.4	88.15	7.85
216.50	41.0	135.00	10.11	40.9	95.00	4.74	49.0	113.20	4.50
217.00	40.2	94.84	4.10	48.3	106.11	5.19	51.3	109.99	4.86
217.50	43.7	91.98	9.37	49.0	108.43	76.84	50.4	120.96	3.79
218.00	39.9	306.25	13.06	44.9	106.56	6.30	46.3	260.10	3.20
218.50	44.1	112.89	4.97	46.2	93.37	14.27	47.2	90.83	3.52
219.00	40.3	121.91	3.89	45.8	117.90	4.21	49.9	124.56	4.45
219.50	42.5	125.38	2.87	49.8	95.81	5.91	54.1	121.29	4.07
220.00	43.7	111.97	3.95	45.6	128.48	4.88	52.6	125.12	5.31
220.50	46.9	86.99	12.77	48.8	121.87	5.58	49.9	3.52	3.07
221.00	44.6	80.95	7.37	50.8	83.66	5.37	50.6	75.76	3.52
221.50	50.5	120.17	4.89	50.4	115.14	4.49	50.4	107.02	4.74
222.00	46.9	122.47	6.21	52.9	97.82	4.72	52.3	120.53	5.37
222.50	49.9	74.54	4.96	53.7	77.01	6.07	53.9	112.01	4.79
223.00	48.5	343.18	5.41	49.0	343.44	6.30	50.8	127.23	2.50
223.50	50.4	77.62	5.79	53.0	67.48	5.47	53.4	71.57	5.12
224.00	48.2	111.57	5.26	47.8	120.96	41.67	51.2	348.98	3.10
224.50	44.5	50.44	8.15	45.0	40.24	4.76	51.0	88.73	5.40
225.00	47.3	132.14	2.86	50.1	96.63	5.61	53.0	100.18	6.13
225.50	47.2	100.01	4.69	50.6	68.81	4.62	52.3	93.37	4.78
226.00	43.5	185.33	3.23	48.7	126.51	2.54	49.9	128.75	2.59
226.50	46.4	86.76	4.58	51.5	81.33	4.07	55.0	76.22	4.45
227.00	47.9	94.64	6.55	50.4	98.13	6.87	52.4	99.06	3.48
227.50	42.6	65.92	4.72	45.2	269.29	3.00	52.5	267.88	3.00
228.00	43.7	64.75	4.15	52.3	73.39	4.09	53.4	71.57	4.04
228.50	48.6	67.11	4.77	46.9	61.99	4.56	48.4	152.10	12.63
229.00	42.9	269.29	3.00	47.5	189.32	3.58	49.5	188.81	3.38
229.50	48.8	95.55	3.96	50.5	72.91	4.11	51.8	68.96	17.45
230.00	44.7	169.99	14.08	43.2	165.47	8.71	47.2	118.01	4.56
230.50	40.6	72.98	4.74	47.4	76.83	5.03	53.7	93.37	4.76
231.00	43.0	123.41	4.32	48.3	97.82	4.72	48.7	340.06	3.31
231.50	41.0	135.92	2.77	44.9	99.69	5.84	52.2	96.63	5.61
232.00	44.3	91.17	4.96	51.9	88.73	5.40	52.6	86.76	4.58
232.50	48.5	100.84	5.08	49.8	118.20	3.10	52.6	117.53	3.04
233.00	44.2	101.31	5.30	51.5	98.84	5.34	48.5	209.65	3.25
233.50	46.5	98.84	5.34	44.7	8.13	34.37	47.5	116.18	3.70
234.00	47.3	115.97	5.60	46.7	279.90	3.80	54.6	91.12	4.78
234.50	49.5	91.47	6.23	47.2	258.18	5.53	56.0	93.37	4.76
235.00	40.0	84.81	7.33	54.7	93.99	5.64	57.1	107.59	5.65
235.50	45.9	65.88	4.41	49.7	117.35	7.44	51.1	118.50	5.10
236.00	49.8	91.22	5.17	51.4	114.68	5.97	56.6	120.53	5.37
236.50	53.9	91.12	4.76	55.3	119.05	4.72	59.4	101.73	4.49
237.00	46.6	120.38	7.23	53.6	107.70	4.93	56.8	107.70	4.37
237.50	46.1	146.74	4.11	48.6	144.04	3.86	53.2	144.04	3.86
238.00	48.7	121.66	4.40	48.0	216.12	5.31	50.2	28.74	6.87
238.50	51.4	100.41	4.88	50.5	96.07	5.14	50.9	329.47	5.37
239.00	46.2	77.15	4.16	50.2	326.77	7.01	50.2	326.77	7.01
239.50	50.8	91.17	4.96	50.8	91.17	4.96	50.8	91.17	4.96
240.00	45.4	28.50	6.10	45.4	28.50	6.10	45.4	28.50	6.10

Table VII.9.1b Output of "sliding" window f-k analysis for shear wave section, caption otherwise as for a).

		FILTER : 3					
		AZIMUTH : 90.00					
WINDOW :		0.50		1.00		1.50	
TIME	SEMBL	VELO	SEMBL	VELO	SEMBL	VELO	
120.00	0.07	13.00	0.07	13.75	0.09	13.75	
120.50	0.16	12.25	0.13	12.75	0.12	12.75	
121.00	0.19	12.75	0.19	12.25	0.14	12.25	
121.50	0.10	10.50	0.08	13.00	0.10	12.75	
122.00	0.13	6.00	0.10	6.25	0.08	6.25	
122.50	0.07	12.75	0.07	7.00	0.08	6.50	
123.00	0.07	7.00	0.09	13.75	0.11	12.75	
123.50	0.19	13.75	0.12	13.75	0.10	6.75	
124.00	0.17	6.75	0.11	6.75	0.10	13.75	
124.50	0.09	11.00	0.12	6.75	0.12	6.75	
125.00	0.15	6.00	0.19	8.75	0.16	8.75	
125.50	0.23	8.75	0.23	9.25	0.39	9.25	
126.00	0.49	11.00	0.71	9.25	0.75	9.25	
126.50	0.82	9.25	0.80	9.25	0.79	9.25	
127.00	0.82	9.25	0.79	9.25	0.79	9.25	
127.50	0.76	9.75	0.75	9.75	0.72	9.25	
128.00	0.55	10.75	0.62	10.00	0.64	10.00	
128.50	0.50	9.25	0.45	9.25	0.48	10.75	
129.00	0.30	13.00	0.22	13.00	0.36	9.25	
129.50	0.33	7.50	0.24	7.50	0.20	8.75	
130.00	0.13	6.50	0.31	7.50	0.29	8.75	
130.50	0.47	10.75	0.35	10.75	0.34	8.75	
131.00	0.43	8.00	0.44	8.75	0.39	8.75	
131.50	0.31	8.50	0.39	8.50	0.40	8.75	
132.00	0.44	8.75	0.34	8.75	0.31	8.75	
132.50	0.12	13.25	0.25	11.00	0.27	11.00	
133.00	0.22	11.00	0.23	9.75	0.19	8.75	
133.50	0.29	7.50	0.26	8.75	0.24	8.25	
134.00	0.28	7.25	0.24	7.25	0.30	9.75	
134.50	0.44	13.00	0.51	9.75	0.45	9.75	
135.00	0.63	9.25	0.55	9.25	0.47	9.25	
135.50	0.18	7.50	0.31	8.00	0.40	9.25	
136.00	0.30	7.00	0.24	7.00	0.21	7.00	
136.50	0.14	7.00	0.15	7.00	0.16	7.00	
137.00	0.10	9.75	0.10	7.50	0.14	8.50	
137.50	0.28	8.50	0.23	8.50	0.18	8.75	
138.00	0.23	7.50	0.25	7.50	0.27	7.50	
138.50	0.29	7.50	0.32	7.50	0.29	7.50	
139.00	0.34	8.00	0.32	8.00	0.29	8.00	
139.50	0.25	7.25	0.27	8.25	0.30	8.25	
140.00	0.34	8.25	0.28	8.00	0.25	8.25	
140.50	0.19	8.75	0.25	8.00	0.27	8.00	
141.00	0.36	7.00	0.26	7.00	0.19	6.50	
141.50	0.13	6.50	0.12	6.50	0.14	6.50	
142.00	0.09	13.75	0.08	13.75	0.10	8.00	
142.50	0.18	12.75	0.15	12.75	0.11	8.00	
143.00	0.18	8.75	0.14	7.25	0.17	7.25	
143.50	0.22	7.25	0.17	7.25	0.18	7.25	
144.00	0.12	6.00	0.25	9.75	0.22	9.25	
144.50	0.34	12.00	0.33	12.25	0.30	12.25	
145.00	0.36	12.25	0.30	12.25	0.29	12.25	
145.50	0.13	11.00	0.20	11.00	0.22	11.00	
146.00	0.20	8.00	0.11	8.00	0.10	8.00	
146.50	0.05	6.25	0.13	8.00	0.16	9.25	
147.00	0.29	9.25	0.21	9.25	0.20	8.75	
147.50	0.32	8.75	0.28	8.00	0.27	9.00	
148.00	0.24	8.50	0.26	9.00	0.23	9.00	
148.50	0.09	6.25	0.11	9.00	0.14	9.00	
149.00	0.05	9.00	0.04	6.25	0.07	6.25	
149.50	0.14	7.00	0.27	8.00	0.24	8.00	
150.00	0.40	8.00	0.43	8.00	0.37	8.00	

Table VII.9.2a Output of "sliding" window semblance analysis with azimuth fixed at 90 deg, and traces 3.0-5.0 Hz bandpass filtered. Windows of lengths 0.5, 1.0 and 1.5 have been used. Semblance values less than 0.3 not considered significant. Finally, fixing azimuths at 80 and 100 deg did not profoundly change the semblance results displayed here.

SEMBLANCE COHERENCY ANALYSIS OF WGRESS SPZ DATA.
 DATA FILE : NRS85029 11594002
 CHANNELS NOT USED : B3 B4 B5 A1 A2 A3 B1 B2

FILTER : 2
 AZIMUTH : 90.00

WINDOW :	1.00		1.50		2.00	
TIME	SEMBL	VEL0	SEMBL	VEL0	SEMBL	VEL0
210.00	0.35	7.50	0.32	7.50	0.28	7.50
210.50	0.25	7.50	0.31	7.50	0.28	7.50
211.00	0.20	7.25	0.19	7.50	0.18	7.50
211.50	0.11	7.50	0.12	3.50	0.15	7.25
212.00	0.20	4.00	0.17	4.00	0.15	3.75
212.50	0.24	4.00	0.19	4.00	0.16	4.00
213.00	0.15	7.00	0.16	7.25	0.18	4.25
213.50	0.19	5.50	0.15	5.50	0.15	5.25
214.00	0.17	5.50	0.17	5.50	0.17	5.50
214.50	0.15	5.25	0.18	5.25	0.19	6.50
215.00	0.25	6.75	0.23	6.75	0.20	6.75
215.50	0.25	6.75	0.25	6.75	0.23	6.75
216.00	0.20	6.75	0.23	6.75	0.19	6.75
216.50	0.23	4.25	0.21	4.25	0.20	4.25
217.00	0.28	4.25	0.33	4.25	0.29	4.25
217.50	0.33	4.25	0.30	4.25	0.24	4.25
218.00	0.19	4.00	0.20	4.00	0.22	5.00
218.50	0.20	6.00	0.20	5.00	0.20	5.00
219.00	0.23	5.00	0.21	5.00	0.19	7.00
219.50	0.19	7.00	0.22	6.25	0.19	5.00
220.00	0.18	6.25	0.19	7.00	0.17	7.50
220.50	0.15	3.25	0.15	6.00	0.20	5.75
221.00	0.22	5.75	0.18	5.75	0.16	5.75
221.50	0.17	5.75	0.16	5.75	0.16	5.75
222.00	0.13	6.75	0.15	5.50	0.17	4.75
222.50	0.19	4.00	0.14	3.75	0.15	4.00
223.00	0.21	4.00	0.24	4.25	0.27	4.25
223.50	0.33	4.25	0.31	4.25	0.29	4.50
224.00	0.35	4.50	0.35	4.50	0.30	4.50
224.50	0.27	5.00	0.27	4.50	0.27	4.50
225.00	0.16	3.00	0.17	3.00	0.22	4.50
225.50	0.17	4.50	0.18	4.25	0.21	4.25
226.00	0.32	5.00	0.28	4.25	0.23	4.25
226.50	0.30	4.25	0.34	5.00	0.31	5.00
227.00	0.29	5.00	0.29	5.00	0.26	5.00
227.50	0.20	5.25	0.21	5.50	0.20	5.00
228.00	0.15	3.00	0.13	3.25	0.14	5.25
228.50	0.17	3.50	0.18	3.50	0.18	3.50
229.00	0.22	3.50	0.21	3.50	0.23	3.75
229.50	0.29	3.75	0.26	3.75	0.23	3.75
230.00	0.25	4.00	0.21	3.75	0.20	3.75
230.50	0.09	3.50	0.17	3.75	0.17	3.75
231.00	0.07	3.00	0.07	7.50	0.08	7.50
231.50	0.11	7.50	0.09	7.50	0.12	4.50
232.00	0.19	4.50	0.22	4.50	0.20	4.50
232.50	0.30	4.50	0.24	4.50	0.22	4.50
233.00	0.23	4.50	0.30	4.50	0.31	4.50
233.50	0.34	4.25	0.28	4.25	0.33	4.50
234.00	0.41	4.25	0.46	4.25	0.43	4.75
234.50	0.48	4.75	0.44	4.75	0.46	4.75
235.00	0.51	4.75	0.47	4.75	0.44	4.75
235.50	0.41	4.75	0.50	4.75	0.52	4.75
236.00	0.54	4.75	0.56	4.50	0.53	4.50
236.50	0.60	4.50	0.51	4.50	0.44	4.50
237.00	0.38	4.50	0.36	4.50	0.38	4.50
237.50	0.11	7.00	0.14	5.25	0.23	4.50
238.00	0.07	3.00	0.12	4.50	0.15	4.50
238.50	0.22	4.00	0.21	4.25	0.19	4.25
239.00	0.34	4.25	0.29	4.25	0.28	4.50
239.50	0.38	4.50	0.35	4.50	0.35	4.50
240.00	0.38	4.50	0.30	4.50	0.06	3.00

Table VII.9.2b Output of "sliding" window semblance analysis for shear wave section. Caption otherwise as for a).

PRINTING OF APPARENT P-WAVE VELOCITY AND DIRECTION FOR
AZIMUTH OF MAXIMUM PROBABILITY WITHIN EACH TIMEWINDOW

TIME	PROBABILITY	AZIMUTH	VELOCITY
120.00	0.28		
120.50	0.01		
121.00	0.00		
121.50	0.58	0.00	10.473
122.00	0.98	14.00	8.399
122.50	0.34	0.00	6.000
123.00	0.45	164.00	6.000
123.50	0.00		
124.00	0.21		
124.50	0.79	24.00	8.281
125.00	0.92	10.00	8.632
125.50	0.20		
126.00	0.62	62.00	10.501
126.50	0.57	86.00	10.994
127.00	0.79	90.00	12.190
127.50	1.00	98.00	14.425
128.00	0.74	94.00	15.192
128.50	0.09		
129.00	0.90	36.00	19.155
129.50	0.56	44.00	17.023
130.00	0.77	74.00	9.902
130.50	0.87	62.00	11.351
131.00	0.76	76.00	28.976
131.50	0.55	172.00	100.000
132.00	0.02		
132.50	0.04		
133.00	0.63	116.00	6.000
133.50	0.52	66.00	6.000
134.00	0.95	70.00	6.151
134.50	0.97	158.00	11.394
135.00	0.41	132.00	10.515
135.50	0.09		
136.00	0.00		
136.50	0.00		
137.00	0.06		
137.50	0.05		
138.00	0.00		
138.50	0.00		
139.00	0.56	98.00	20.071
139.50	0.51	122.00	7.057
140.00	0.33	114.00	6.000
140.50	0.72	112.00	6.000
141.00	0.72	142.00	6.815
141.50	0.49	74.00	8.861
142.00	0.57	118.00	7.368
142.50	0.18		
143.00	0.68	92.00	7.063
143.50	0.84	164.00	18.327
144.00	0.71	162.00	6.573
144.50	0.71	92.00	14.904
145.00	0.18		
145.50	0.47	180.00	9.164
146.00	0.82	38.00	6.620
146.50	0.15		
147.00	0.07		
147.50	0.68	30.00	10.593
148.00	0.76	110.00	6.162
148.50	0.47	52.00	8.255
149.00	0.53	14.00	6.867
149.50	0.73	104.00	11.011
150.00	0.47	118.00	6.948

Table VII.9.3a Estimates of apparent P-wave velocity at site A₀ on the basis of the 3-comp. seismogram analysis. Window length 1.0 sec and traces 3.0-5.0 Hz bandpass filtered. For P-wave presences, probabilities less than 30 per cent (0.3), velocity estimates deleted due to lack of significance.

PRINTING OF APPARENT PHASE VELOCITY AND SLOWNESS FOR
AZIMUTHS OF MAXIMUM PROBABILITY WITHIN EACH TIMEWINDOW

TIME	PROBABILITY	AZIMUTH	VELOCITY	SLOWNESS
210.00	0.39	122.00	10.803	10.292
210.50	0.01			
211.00	0.01			
211.50	0.00			
212.00	0.00			
212.50	0.00			
213.00	0.00			
213.50	0.50	180.00	10.143	10.962
214.00	0.17			
214.50	0.15			
215.00	0.01			
215.50	0.04			
216.00	0.12			
216.50	0.63	180.00	3.464	32.098
217.00	1.00	180.00	3.613	30.775
217.50	0.04			
218.00	0.98	128.00	5.717	19.451
218.50	0.10			
219.00	0.03			
219.50	0.05			
220.00	0.12			
220.50	0.40	110.00	3.464	32.098
221.00	0.83	116.00	3.464	32.098
221.50	0.00			
222.00	0.00			
222.50	0.76	150.00	3.464	32.098
223.00	0.32	122.00	4.317	25.759
223.50	0.20			
224.00	0.00			
224.50	0.01			
225.00	0.00			
225.50	0.02			
226.00	0.48	146.00	3.671	30.292
226.50	0.23			
227.00	0.93	116.00	3.629	30.643
227.50	0.50	92.00	3.666	30.328
228.00	0.78	70.00	3.612	30.784
228.50	0.78	74.00	3.966	23.036
229.00	0.63	26.00	9.527	11.671
229.50	0.22			
230.00	0.00			
230.50	0.04			
231.00	0.55	0.00	3.464	32.098
231.50	0.02			
232.00	0.06			
232.50	0.04			
233.00	0.66	26.00	3.464	32.098
233.50	0.66	14.00	3.619	30.726
234.00	0.40	0.00	3.883	23.637
234.50	0.02			
235.00	0.14			
235.50	0.00			
236.00	0.00			
236.50	0.00			
237.00	0.00			
237.50	0.06			
238.00	0.84	64.00	3.543	31.333
238.50	0.59	72.00	5.546	20.050
239.00	0.16			
239.50	0.26			
240.00	0.56	30.00	3.464	32.098

Table VII.9.3b Estimate of apparent shear wave analysis for shear wave section; caption otherwise as for a).

Figure captions

Fig. VII.9.1: Filtered 3-comp. traces for station A0; the z-component is representative for the other NORESS stations.

a) P-wave section, filter 3.0-5.0 Hz; b) shear wave section, filter 2.0-4.0 Hz.

Fig. VII.9.2a): P-wave semblance estimates as a function of time and phase velocity for $T = 1.0$ sec.; azimuth 90° . b) Same as a) except that looping is over azimuth with $vel = 9.0 \text{ kms}^{-1}$. For details see Table VII.9.2a.

Fig. VII.9.3a): Shear wave semblance estimates as a function of time and phase velocity for $T = 1.0$ sec; azimuth 90° . b) Same as a) except that looping is over azimuth with $vel = 4.5 \text{ kms}^{-1}$. For details see Table VII.9.2b.

Fig. VII.9.4a): 3-component analysis, P-wave probabilities ($0.9 \equiv 90\%$) as a function of time and azimuth; window $T = 1.0$ sec.

b) Same as for a) except this time for the shear wave section.

For estimates of apparent velocities, see Table VII.9.3.

Fig. VII.9.5a): Probability filtered records; only that part of the seisaogram having probabilities of being P-wave motion within the azimuth sector $90 \pm 30^\circ$ is retained. b) Probability filtered shear wave section.

Fig. VII.9.6a-e): This sequence of figures demonstrates the viability of 3-comp. signal analysis under adverse conditions, i.e., SNR around 1 or less. a) Filtered P-wave section (3.0-5.0 Hz) for the beam formed on the basis of the 4 NORESS 3-comp. stations; b) The probability filtered variant of a); c) Unfiltered beam record; d) The probability filtered variant of c) (the original non-band pass record); e) Band pass filtering of the d)-records, which should be compared to b). Our remark is that this record sequence demonstrates convincingly that the 3-comp. analyzing technique works well for SNR around 1 or even smaller values. It should be added that we were unable to reproduce a counterpart to e) on the basis of a single station 3-comp. record.

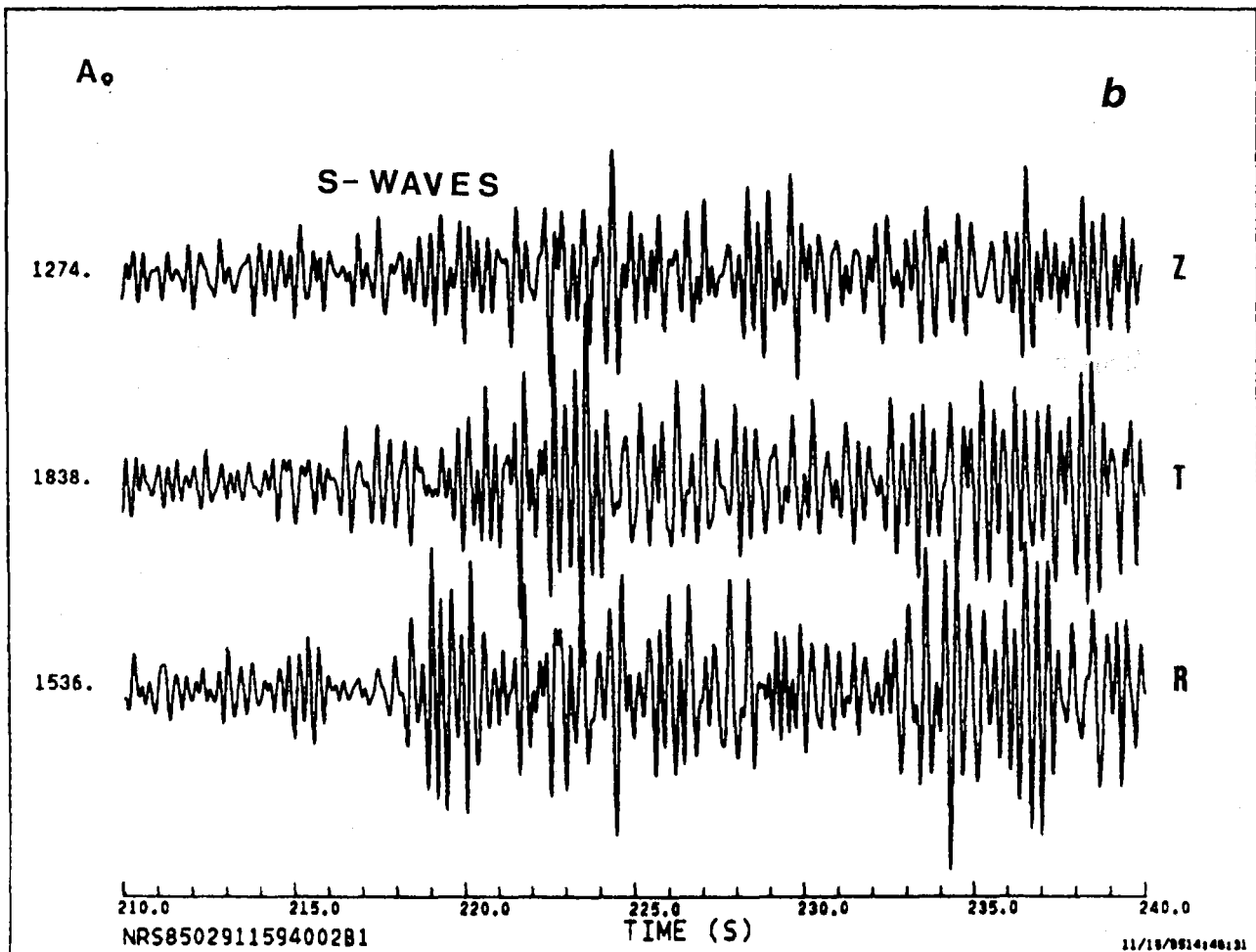
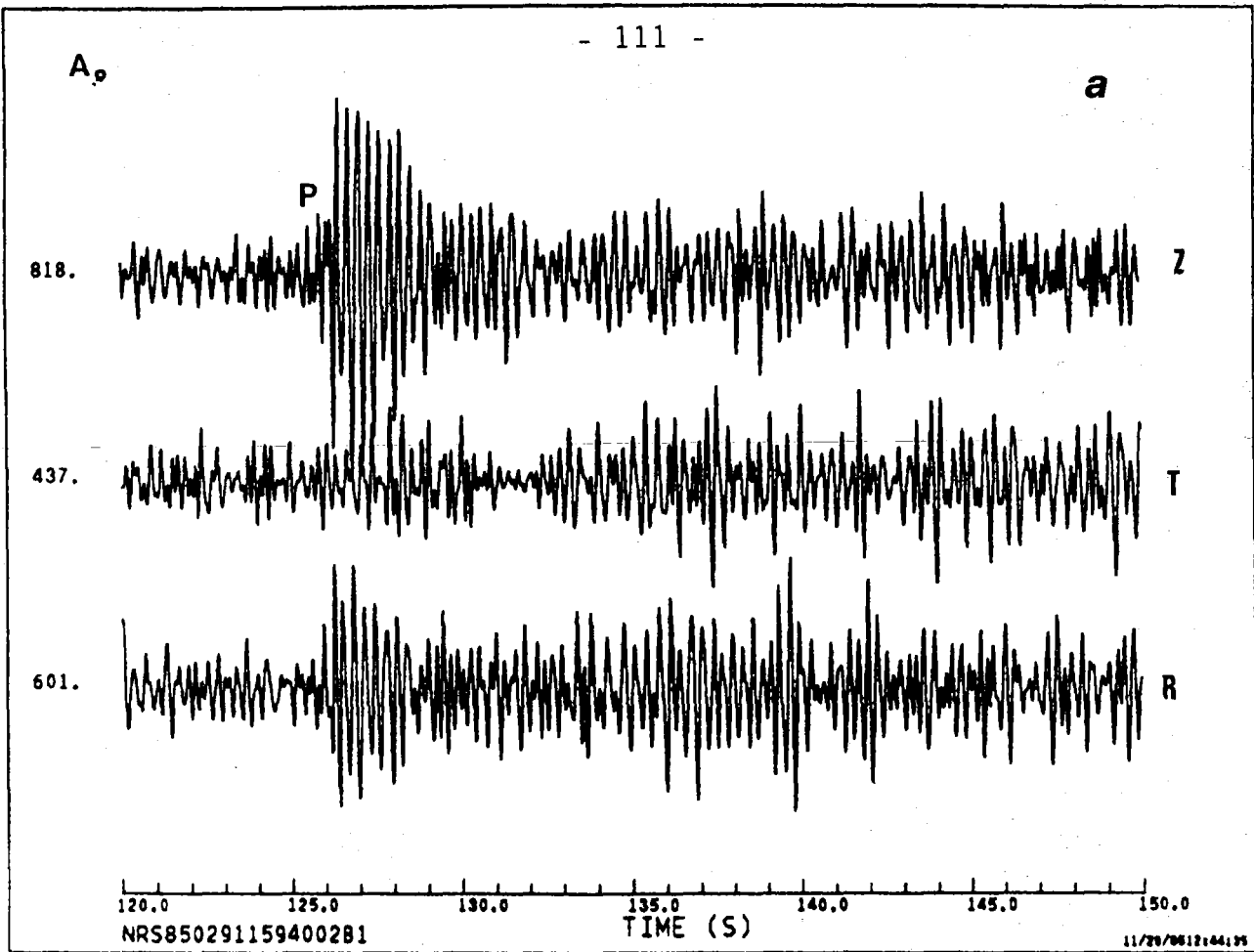


Fig. VII.9.1

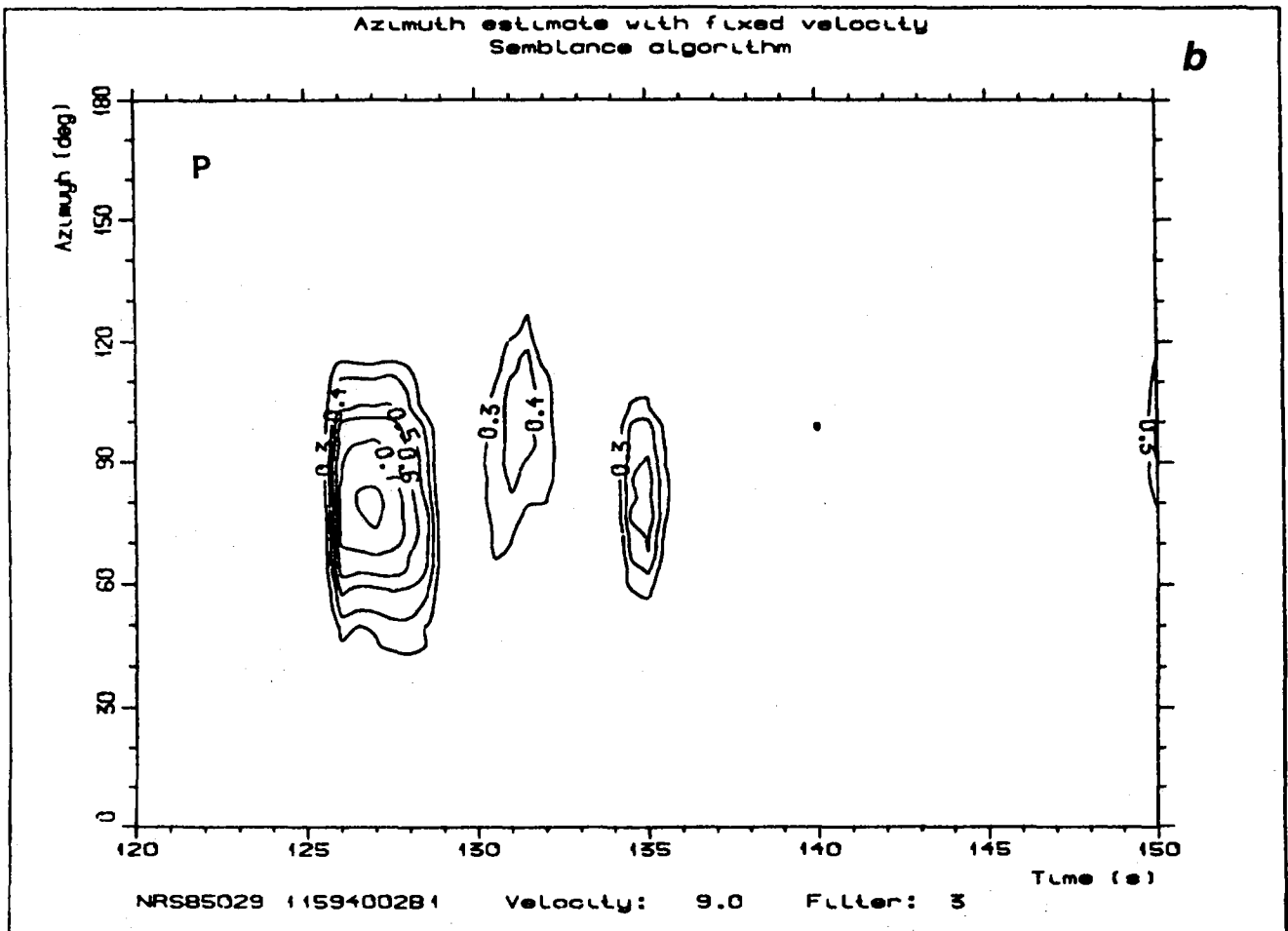
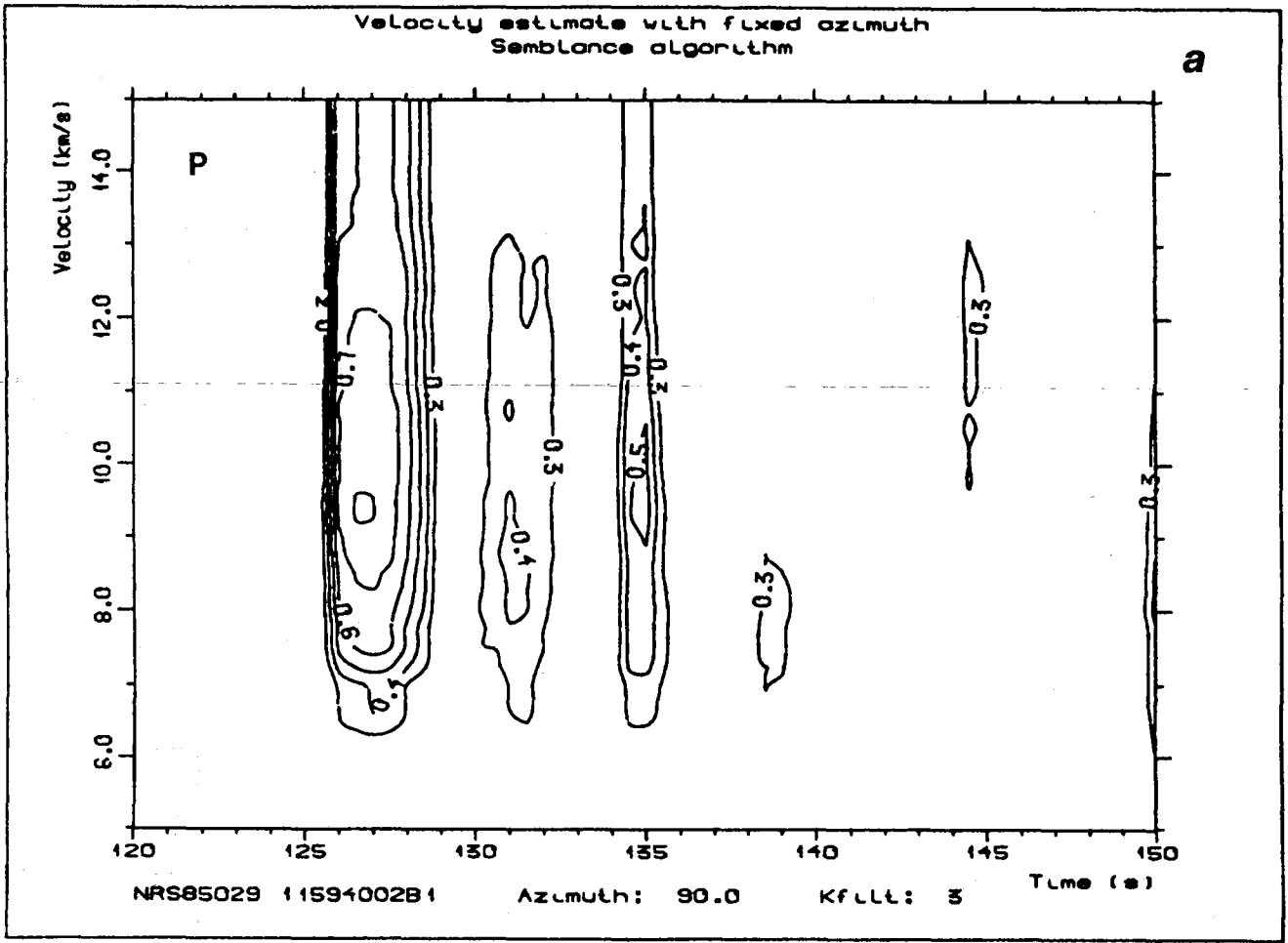


Fig. VII.9.2

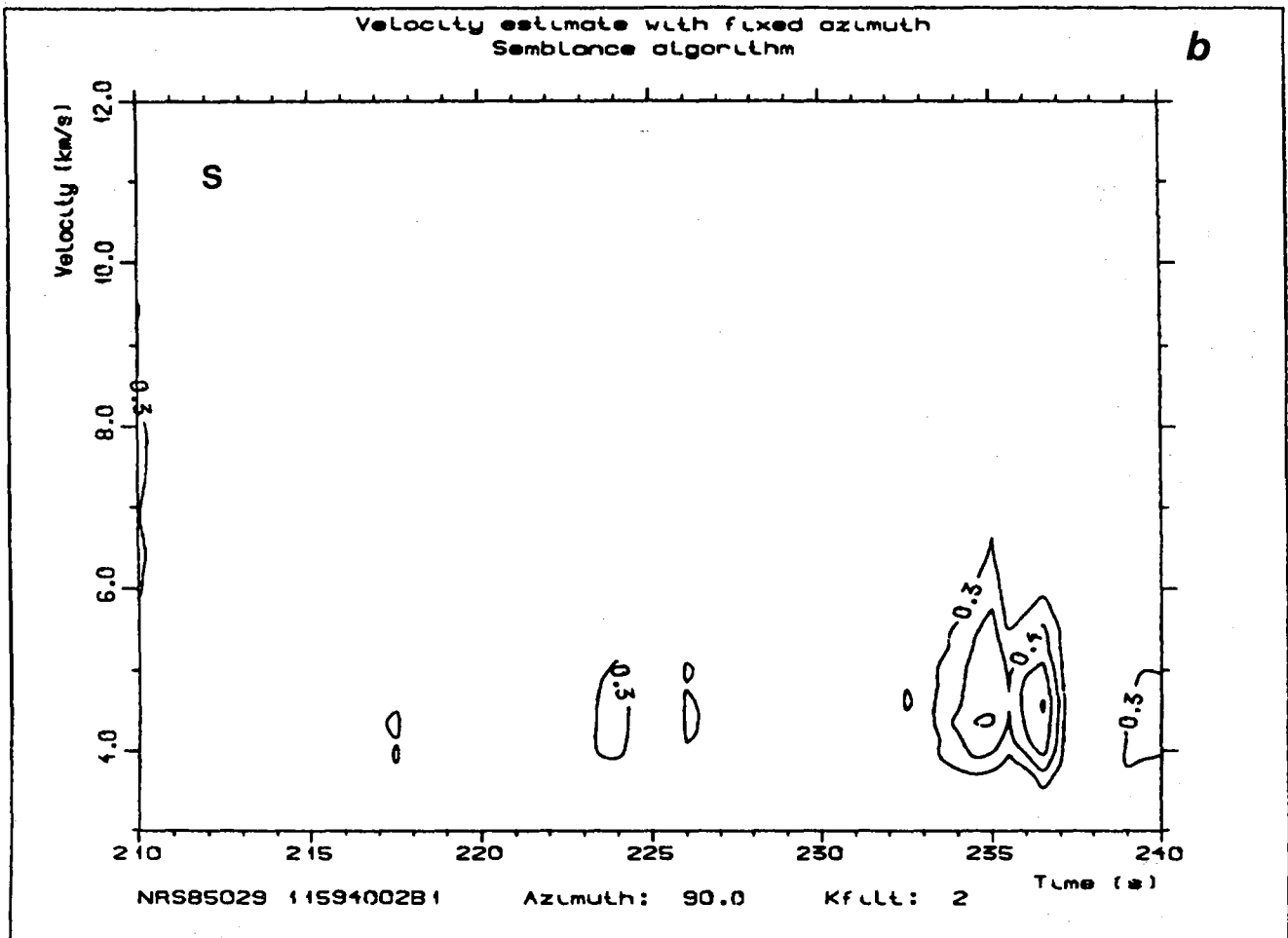
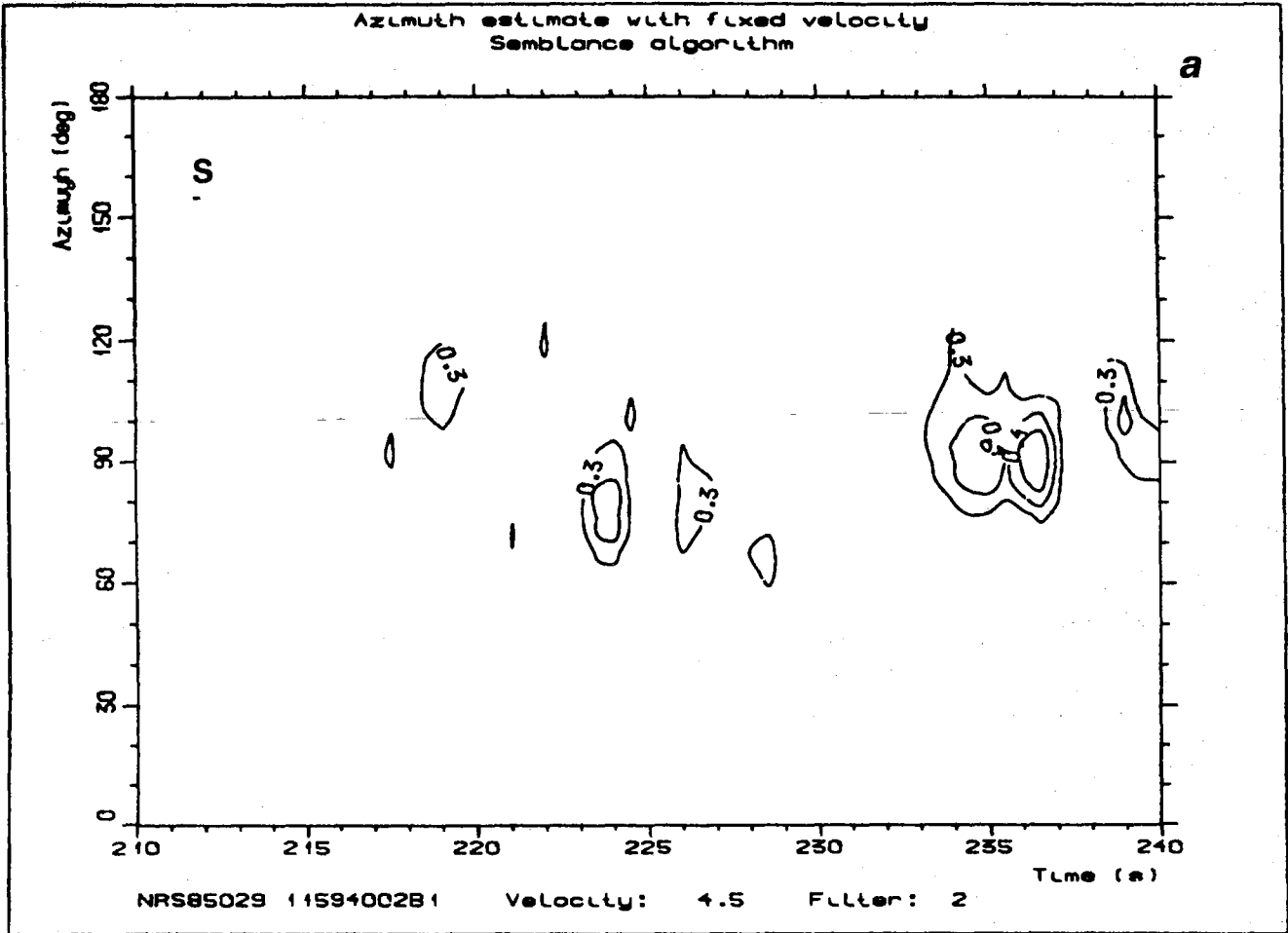


Fig. VII.9.3

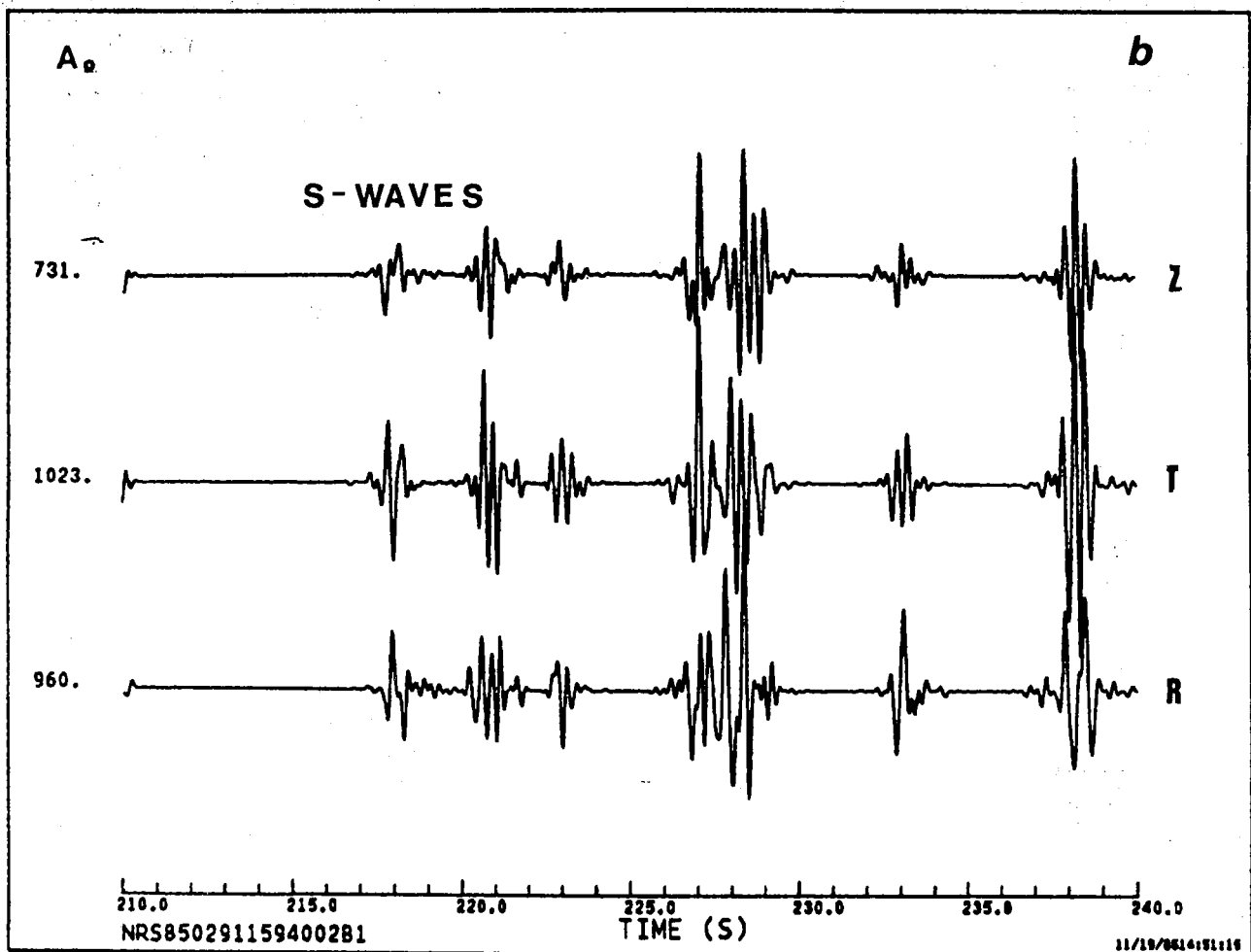
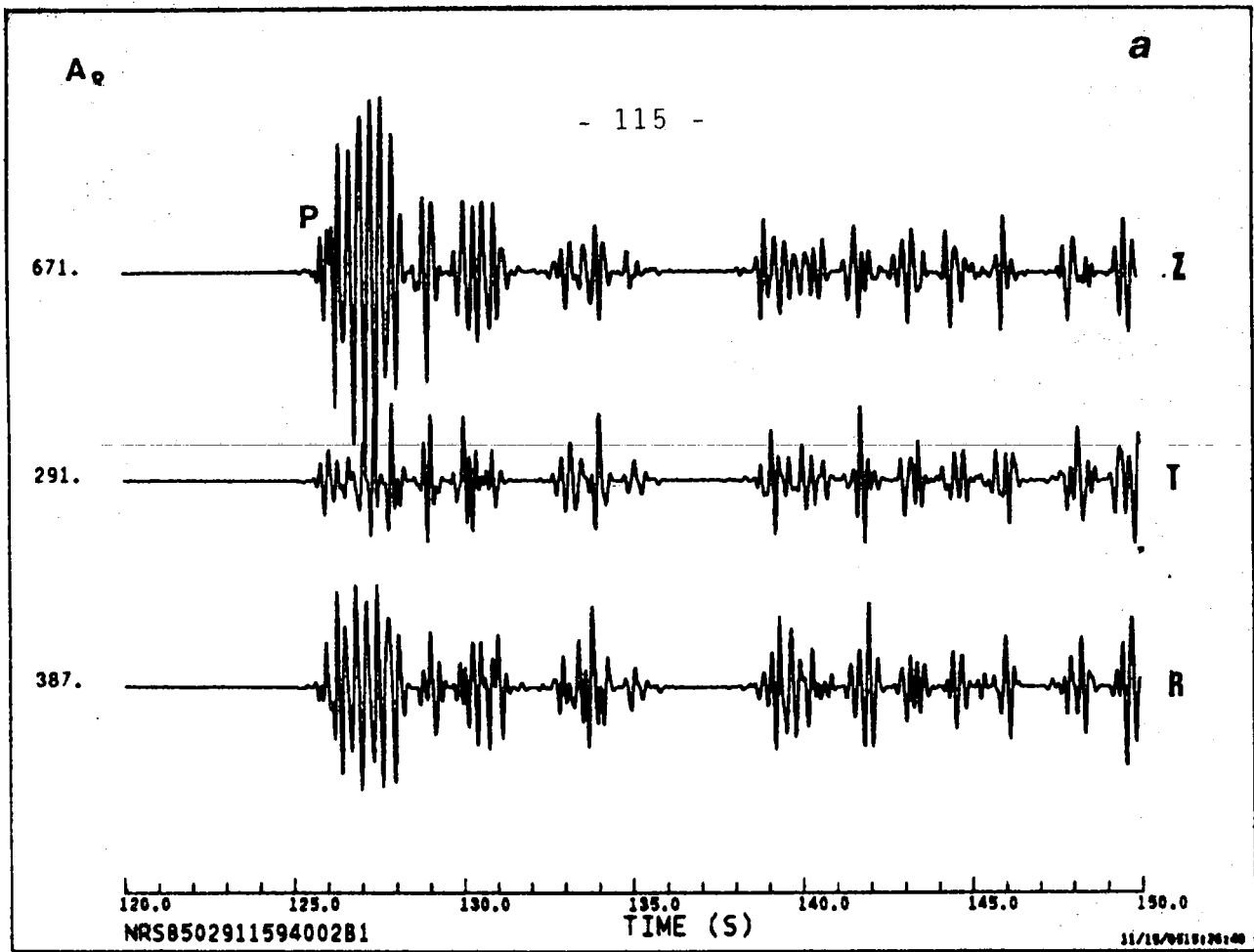


Fig. VII.9.5

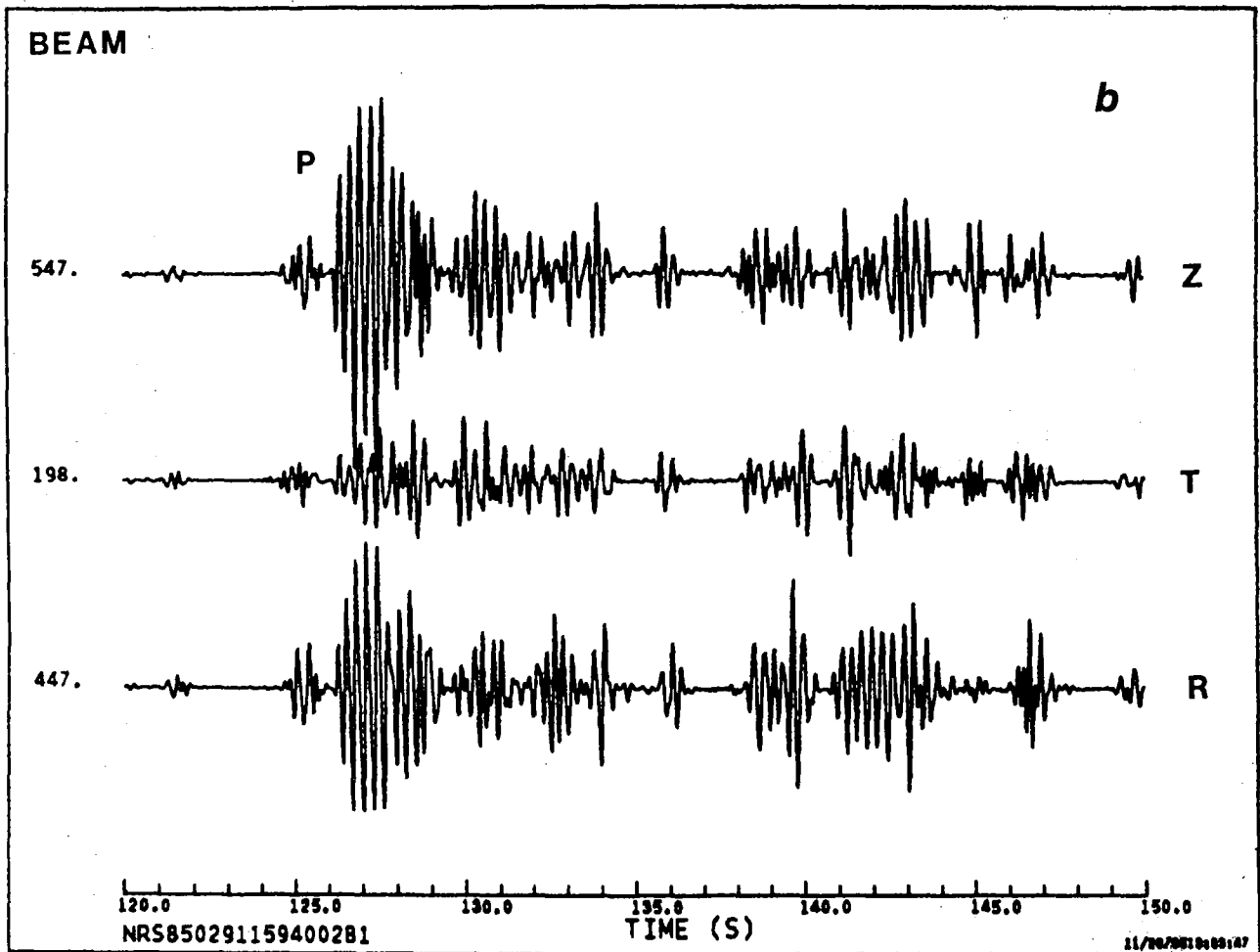
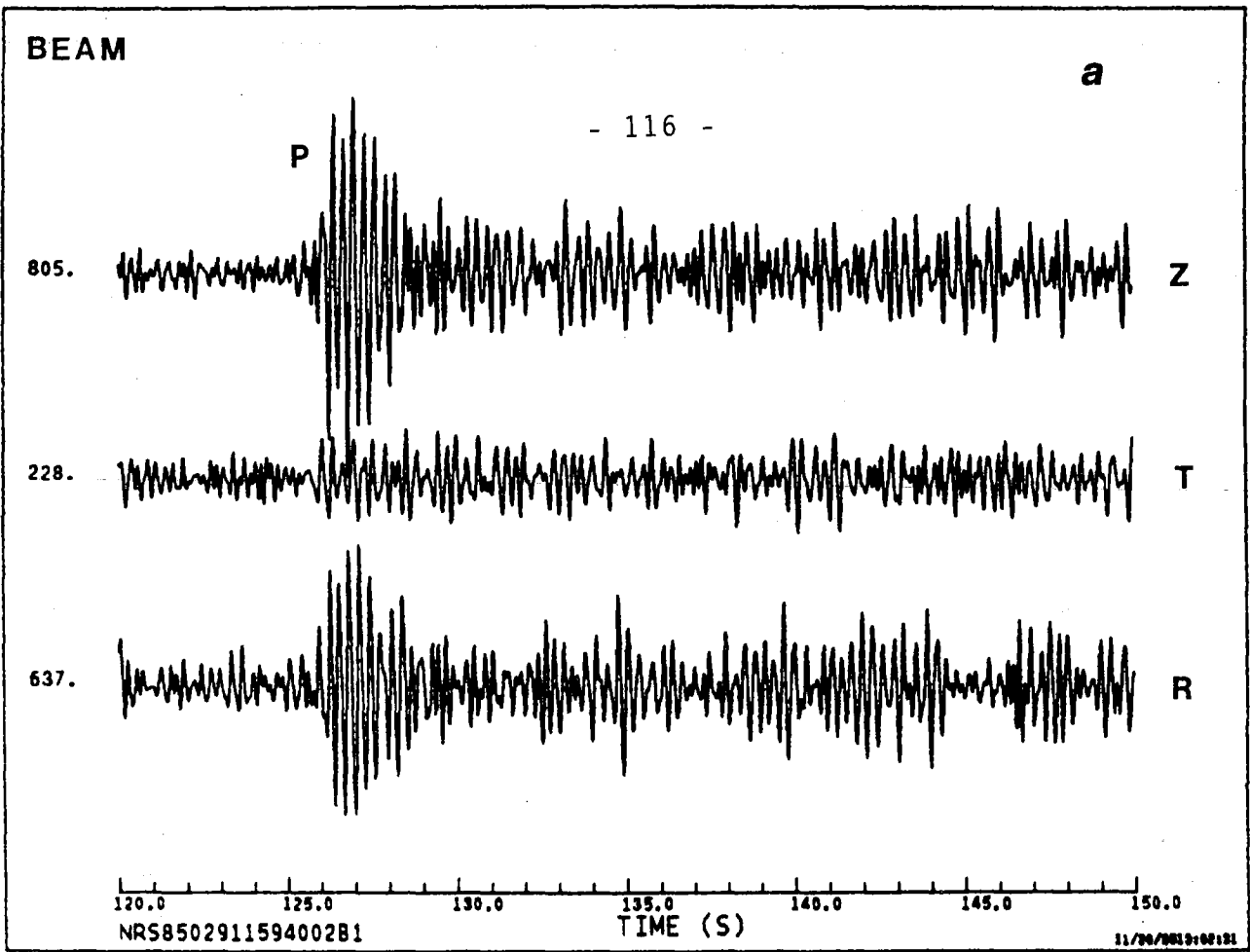


Fig. VII.9.6

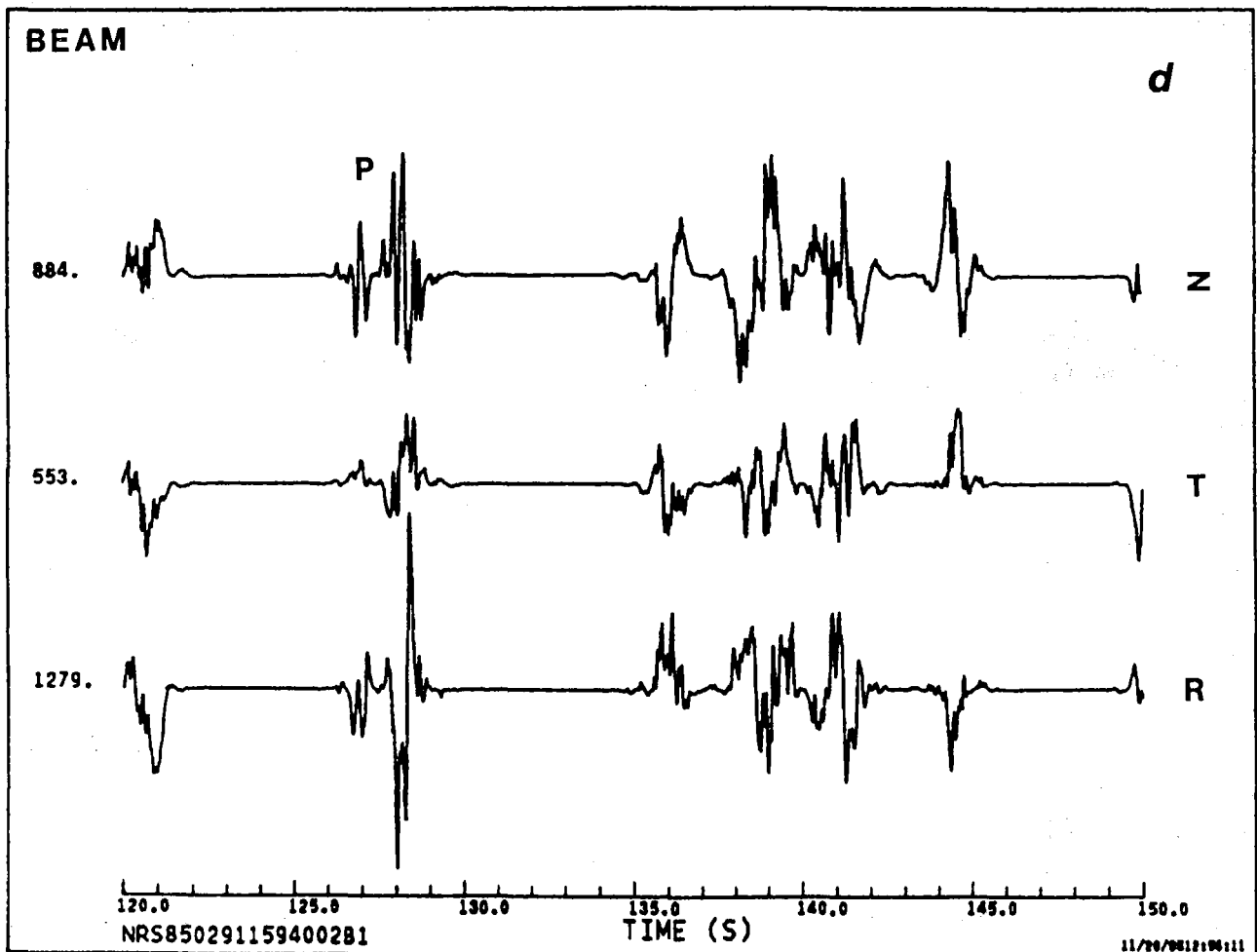
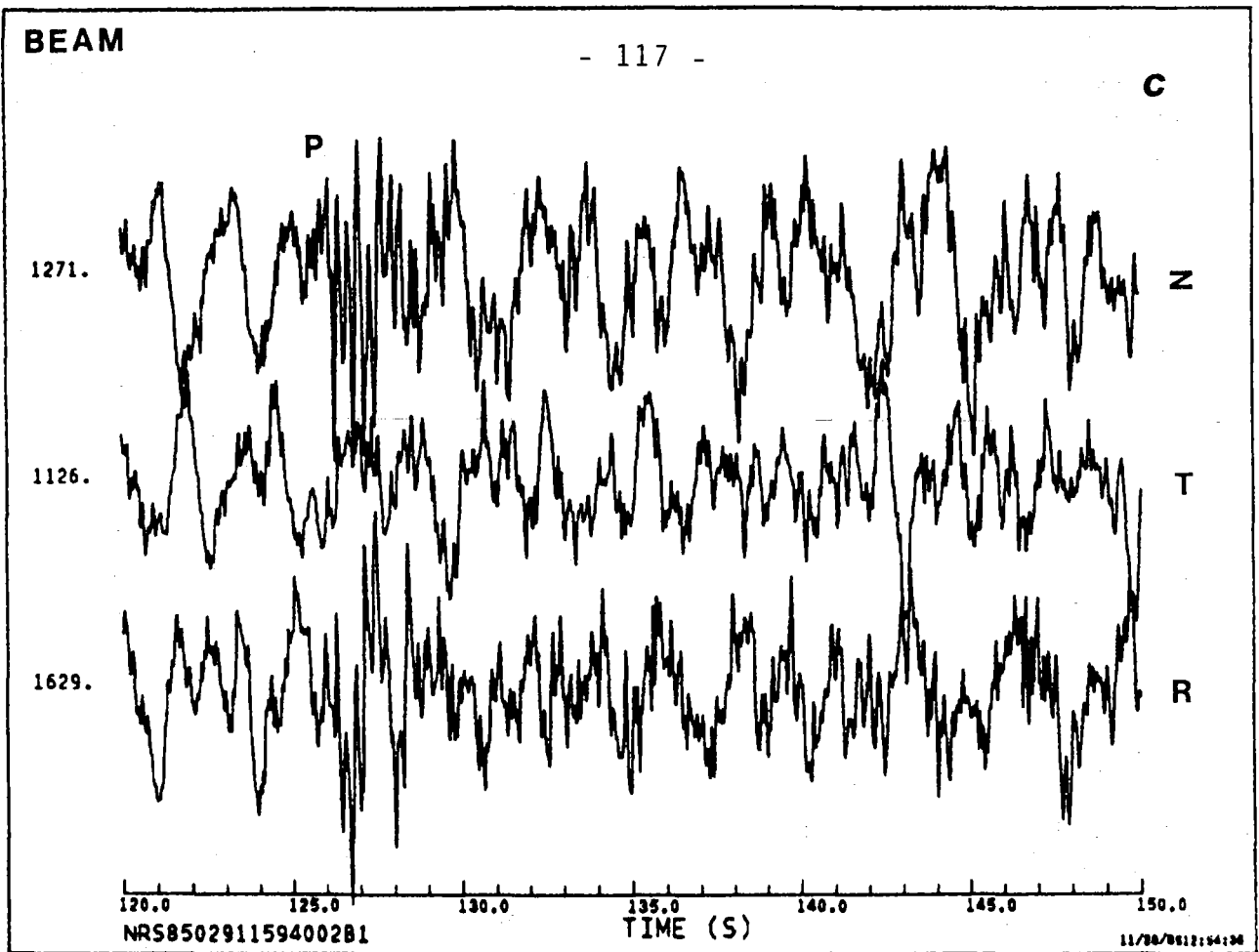


Fig. VII.9.6 (cont.)

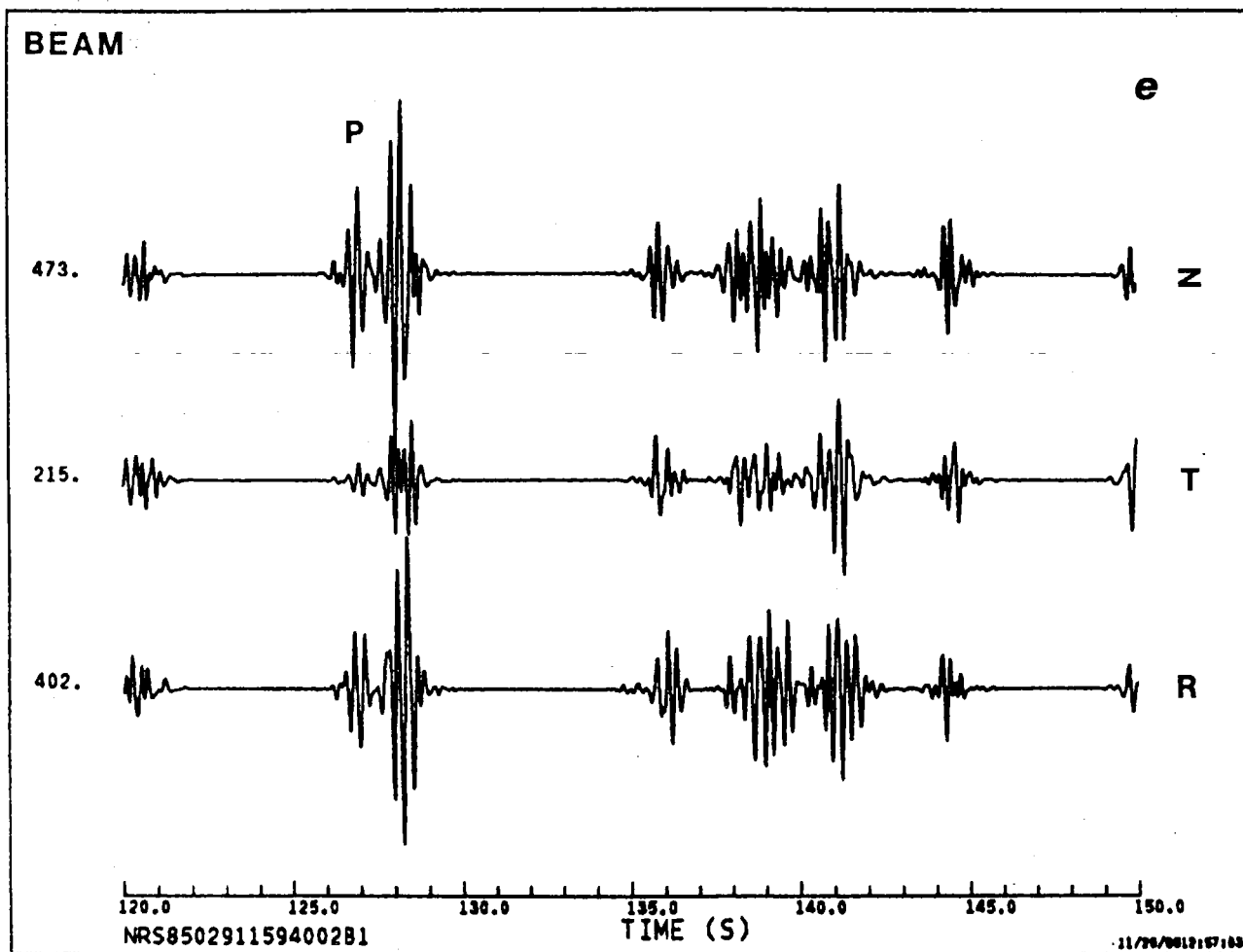


Fig. VII.9.6 (cont.)

VII.10 P-wave coda -- scattering research

The purpose of this study is an on-going effort to determine the nature of the teleseismic P coda seen on short period seismograms, and specifically to separate it into a contribution from scattering near the source, if the source is in the crust, and scattering near the receiver. To accomplish this, digital data from NORSAR and NORESS were used in the frequency range 1-7 Hz and covering a time span of 20-200 sec after first P. The variation of the coda power spectrum of various types of events with time was examined and found to fit a simple exponential decay for all events, although the amplitude of the coda relative to first P was quite different for different types of events, being large for crustal earthquakes and lower for deep-focus earthquakes and explosions. Data from NORESS were examined using frequency-wavenumber methods, particularly by determining the power as a function of wavenumber at a fixed frequency; this is equivalent to finding the power as a function of apparent velocity. Deep-focus events had a coda dominated by low apparent velocities (3.5-4.5 km/sec), explosions a coda with equal power in high (10 km/sec) and low apparent velocities, crustal earthquakes a coda dominated by high apparent velocities. These results indicate that the teleseismic P coda in the time and frequency range considered indeed consists of energy scattered near the source if the source is in the crust (the high apparent velocity component), and energy scattered near the receiver (low apparent velocity component), and energy scattered near the receiver (low apparent velocity component). The low velocities indicate that teleseismic P to Lg (trapped shear wave) is the dominant mode of scattering near the receiver; the differences between crustal earthquakes and explosions suggest Lg to teleseismic P near the source. Multiple scattering is probably occurring in the coda. These results indicate that coda magnitudes will depend on conditions in broad (~ 500 km) regions around the

source and receiver, perhaps explaining their stability. It may be possible to separate the coda from the source and receiver regions, leading to even greater stability. The difference between crustal earthquakes and explosions may be useful as a discriminant. These results are detailed in a recent report by Dainty (1985).

An interesting aspect of coda analysis is to what extent scatters can be separated into deterministic and random contributions. A first experiment here was to identify clear crustal scatters (P_g vel. $< 7 \text{ kms}^{-1}$, $7.0 < P_n < 10.0 \text{ kms}^{-1}$) by 3-comp. coda analysis, and then using differential travel times (re P-onset time) to actually locate these scatters. Preliminary results are displayed in Figs. VII.10.1 and VII.10.2 and the following comments apply. P_g -scattering sources are mainly concentrated to the north and east of NORESS, and the apparent clustering roughly coincides with major tectonic boundaries. Surprisingly, for events to the south hardly any crustal scatters were found (mainly non-shield areas). Roughly the same results are found for P_n -scatters, but the source locations here are more dispersed. The scatter locations in this case would be relatively less constrained, as the scattering mechanism may well be a "bumpy" Moho or asymmetric reflections from the surface (P_n -mode of propagation would be preferential beyond say 250 km).

A. Dainty (MIT)
E.S. Husebye

References

- Dainty, A. (1985): Coda observed at NORSAR and NORESS, Tech. Rep. School of Geophys. Science, Georgia Institute of Technology, Atlanta, GA, USA.

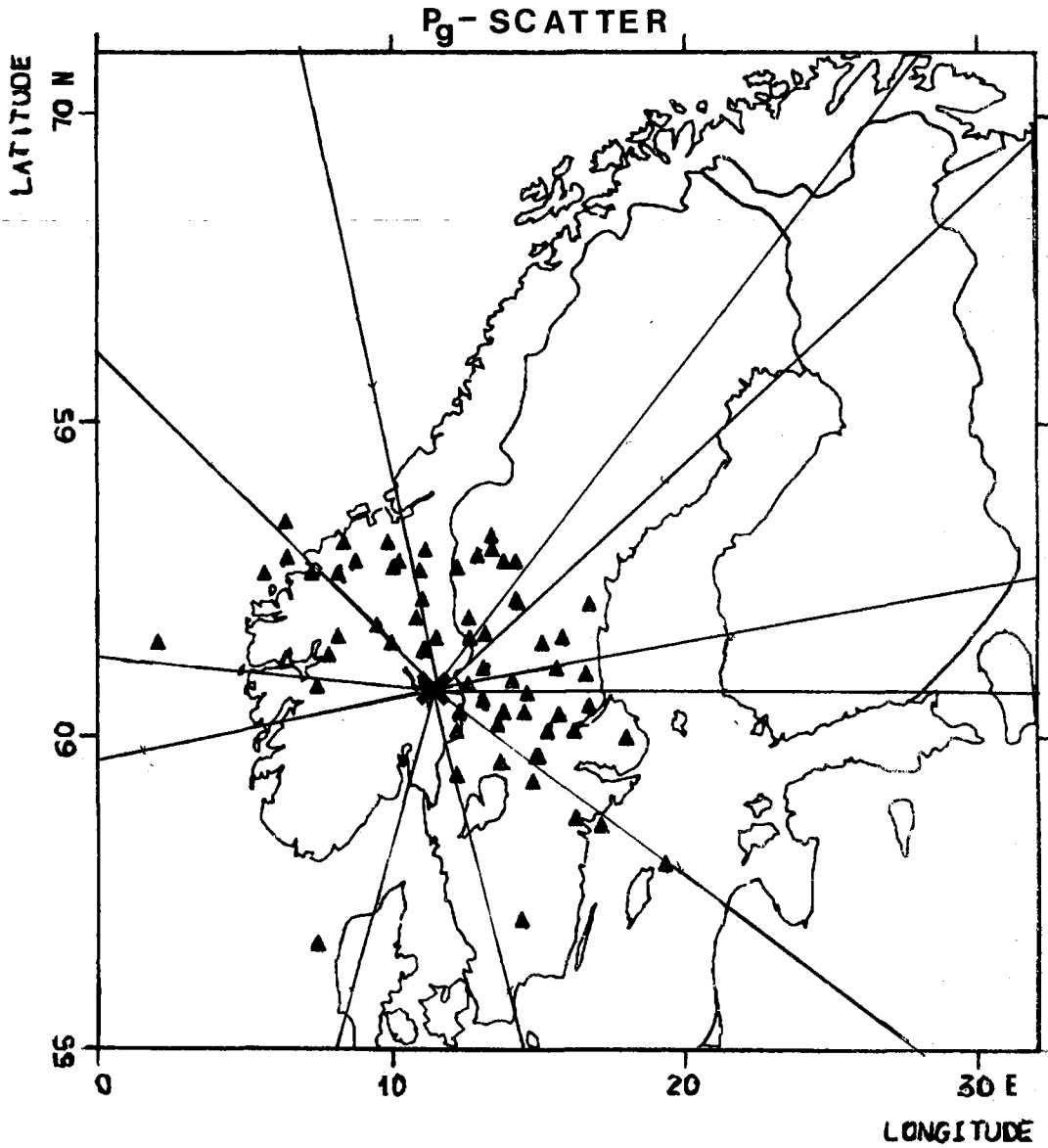


Fig. VII.10.1 Locations of secondary "sources" for coda phases of Pg wave type being subject to scattering at the receiver side. The thin lines represent azimuth of the events used in analysis. Note that the scattering efficiency appears to be relatively weak to the south and west.

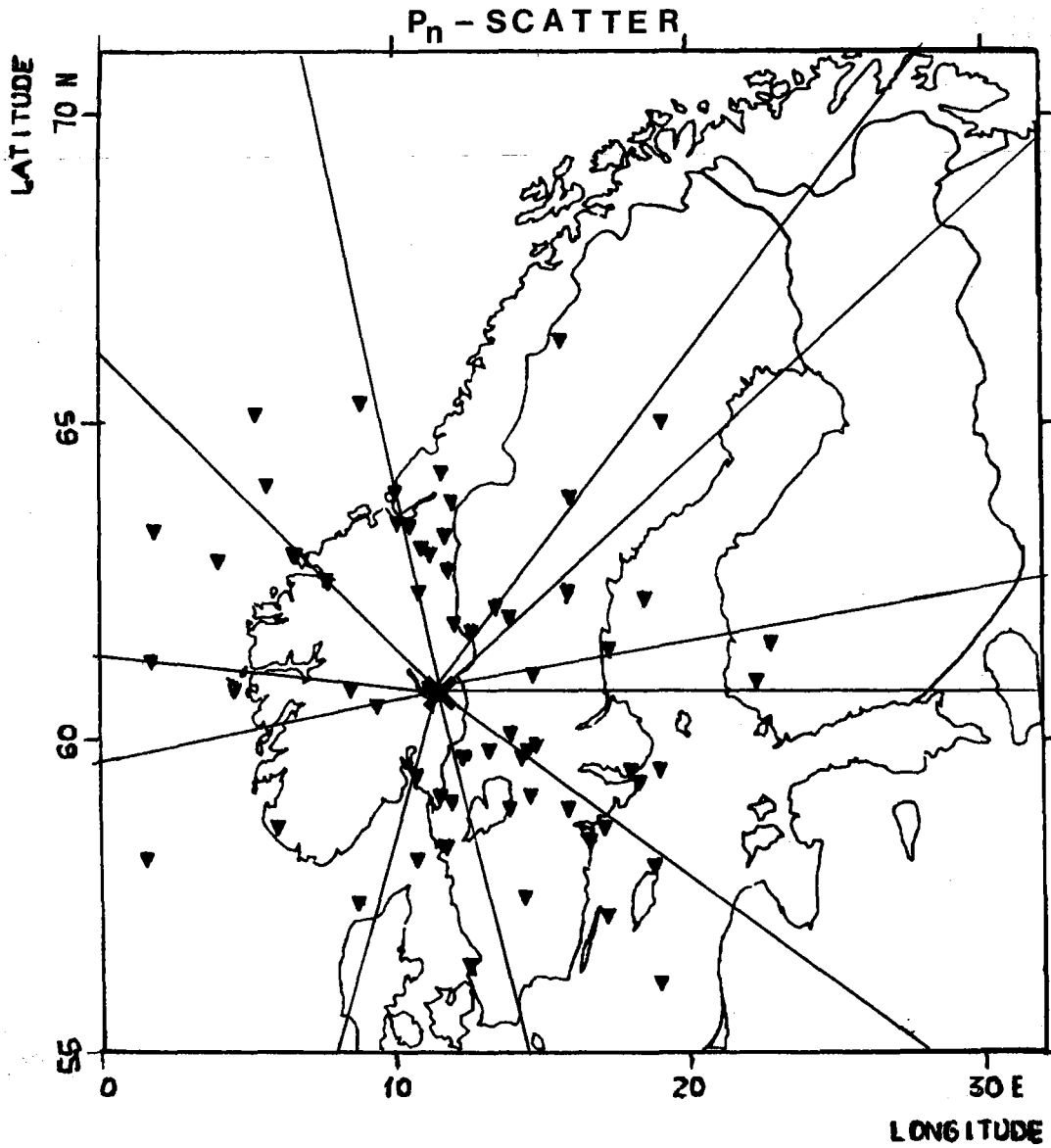


Fig. VII.10.2 Caption as for Fig. VII.10.1 except that now the wave type is P_n. Scattering sources are a bit dispersed and reflect poorer resolution in "secondary" source locations for P_n than P_g.

NORESS DATA TAPE FORMAT

The following tape format has been agreed between SANDIA, LIVERMORE and NOR SAR. On request, NOR SAR will provide NORESS data tapes with the following options:

- 1 sec. blocking (3540 bytes per record)
- 2 sec. blocking (7080 bytes per record)
- 10 sec. blocking (35400 bytes per record) (standard)
- 800/1600 or 6250 bpi, 9 track tapes (6250 bpi is standard)
- Array Geometry Record in EBCDIC (standard) or ASCII

A NORESS tape consists of 3 sections:

1. FILE HEADER (TAPE HEADER) 80 bytes
1 * EOF
2. ARRAY GEOMETRY (AG) RECORD 3600 bytes
IRG (INTER RECORD GAP)
3. DATA (35 FRAMES * 100 BYTES + RECORD HEADER 40 BYTES)
TOTALLY 3540 BYTES IN EACH 1 SEC. BLOCK.
IRG between each sec.

Last 1 sec. block is followed by EOF.

Note that the data record lengths will be different if 2 or 10 seconds blocking has been requested.

In some cases, it might be practical to include several data intervals on one magnetic tape. These intervals will then each comprise three sections (File header, AG record, Data), separated by EOF, unless otherwise specified in documentation accompanying the tape.

1. FILE HEADER:

Bytes 1-14: Fixed format as follows:

Bytes 1-2 :	2 byte binary....Type	00 - AG record in EBCDIC
		01 - AG record in ASCII
Bytes 3-4 :	2 byte binary....Month	} This time corresponds to the first data on the file
Bytes 5-6 :	2 byte binary....Day	
Bytes 7-8 :	2 byte binary....Year	
Bytes 9-10:	2 byte binary....Hour	
Bytes 11-12:	2 byte binary....Min.	
Bytes 13-14:	2 byte binary....Sec.	

Bytes 15-80: Variable format. Tapes generated at NORSAR will contain:

byte 15,16,17,18,19,20	EBCDIC	tape number
byte 21,22	EBCDIC	Creation month
byte 23,24	EBCDIC	Creation day
byte 25-28	EBCDIC	Creation year
byte 29-32	EBCDIC	Array Geometry version no.
byte 38-80	EBCDIC	comments.

2. ARRAY GEOMETRY: (EBCDIC or ASCII)

2.1 General layout

byte	1 -	80	Text (free field) specifying date and time for last change in array geometry. See Table A-1, first line.
byte	81 -	160	Text (Table A-1, second line)
byte	161 -	240	Text (Table A-1, third line) Note: Latitude of center (degrees) in bytes 172-179; Longitude of center (degrees) in bytes 189-196
byte	241 -	320	Blanks
byte	321 -	400	Text
byte	401 -	480	Blanks
byte	481 -	560	specification of first data channel (see 2.2)
	.		
	.		
	.		
byte	3521 -	3600	specification of 39th data channel

2.2 Contents of specification field

Each specification field mentioned above is 80 bytes in length, and describes one data channel. The format is currently as follows:

byte 2-3	:	channel identification (e.g., 21)
byte 7-8	:	site name (e.g., F0)
byte 13-15:	:	component (e.g., SPZ)
byte 16-23:	:	position relative to center of array (NS), in meters
byte 24-31:	:	position relative to center of array (ES), in meters
byte 32-40:	:	elevation (meters above sea level)
byte 41-60:	:	instrument type (e.g., GS-13)
byte 61-80:	:	comments

The ARRAY GEOMETRY RECORD is distributed on all tapes in either ASCII or EBCDIC. The record gives the array configuration corresponding to the actual data on tape. An example is given in Table A-1.

3. DATA:

Each one second data block is 3540 bytes in length and consists of:

RECORD HEADER	40 bytes
1 status frame	100 bytes
34 data frames	34*100 bytes

RECORD HEADER:

byte 1 - 2 EBCDIC: data identification EBCDIC 'NO',
(CFD0) Hexadecimal X'CFD0'
byte 3 - 4 Binary: sampling delay (LP) in tenths of ms
(currently 1008, i.e., 100.8 ms)
byte 5 - 6 Binary: sampling delay (IP) in tenths of ms
(currently 508, i.e., 50.8 ms)
byte 7 - 8 Binary: sampling delay (LP) in tenths of ms
(currently 60, i.e., 6.0 ms)
byte 9 - 10 Binary: correction in milliseconds (fixed)
for UTC. Current value is 1000, i.e.,
1000 ms should be subtracted from
all data times
byte 11 - 40 Binary: spare

DATA:

35 frames (1 status frame, 34 data frames) as described in
HUB documentation. (Table A-2)

STATUS FRAME: word 50 of this frame contains the total
number of frames in this record (1-35).

Note that many conventions used for NORESS status information
and data follow those established for the RSTN network.
Reference is made to Breiding (1983) for additional detail.

Reference:

Breiding, D. (1983): Data users' guide for the Regional
Seismic Test Network (RSTN), Sandia report SAND82-2935.

Table A-1

Example of an Array Geometry Record.
Each line corresponds to 80 bytes.

AG - ARRAY GEOMETRY RECORD 09/27/85 13:30 GMT
NO - NORESS DATA 40.OHZ , 10.OHZ AND 1.OHZ
FO - LAT(D) 60.7353 LON(D) 11.5414

CID	SITE	COMP	NS(M)	EW(M)	ELEV(M)	INSTRUMENT	COMMENTS
21	FO	SPZ	0	0	247	S-3	
61	FO	SPN	0	0	247	S-3	
A1	FO	SPE	0	0	247	S-3	
22	A0	SPZ	3	4	302	GS-13	TEMP. POSITION
62	A0	SPN	3	4	302	GS-13	TEMP. POSITION
A2	A0	SPE	3	4	302	GS-13	TEMP. POSITION
OD	A1	SPZ	146	49	291	GS-13	
OE	A2	SPZ	- 103	108	311	GS-13	
17	B1	SPZ	321	70	299	GS-13	
18	B2	SPZ	30	334	315	GS-13	
0A	B3	SPZ	- 298	143	314	GS-13	
0B	B4	SPZ	- 217	- 228	299	GS-13	
0C	B5	SPZ	163	- 272	289	GS-13	
13	C1	SPZ	687	109	299	GS-13	
0F	C2	SPZ	341	603	339	GS-13	TEMP.CID
14	C3	SPZ	- 238	647	352	GS-13	
23	C4	SPZ	- 657	208	311	GS-13	
63	C4	SPN	- 657	208	311	GS-13	
A3	C4	SPE	- 657	208	311	GS-13	
15	C5	SPZ	- 569	- 396	299	GS-13	
16	C6	SPZ	- 48	- 687	303	GS-13	
24	C7	SPZ	548	- 447	275	GS-13	
64	C7	SPN	548	- 447	275	GS-13	
A4	C7	SPE	548	- 447	275	GS-13	
04	D1	SPZ	1480	192	305	GS-13	
05	D2	SPZ	1015	1098	372	GS-13	
06	D3	SPZ	76	1493	453	GS-13	
07	D4	SPZ	- 901	1189	379	GS-13	
08	D5	SPZ	-1451	335	348	GS-13	
09	D6	SPZ	-1326	- 681	352	GS-13	
10	D7	SPZ	- 566	-1368	337	GS-13	
11	D8	SPZ	414	-1336	301	GS-13	
12	D9	SPZ	1257	- 802	278	GS-13	
C1	E0	IPZ	- 2	3	247	KS-36000-04	
C1	E0	IPN	- 2	3	247	KS-36000-04	
C1	E0	IPE	- 2	3	247	KS-36000-04	
C1	E0	LPZ	- 2	3	247	KS-36000-04	
C1	E0	LPN	- 2	3	247	KS-36000-04	
C1	E0	LPE	- 2	3	247	KS-36000-04	

Table A-2

HUB/Element Data Link Interface

HUB is equipped with 26 synchronous 2400 bit/sec ports for element frame acquisition. Each element uses the HUB transmitter (element receiver) clock as its data frame transmitter clock. At initialization each element will enable output starting when the last byte of a command frame is received from HUB. This method of data frame synchronization, which applies to all elements, defines a single sampling interval throughout the array, so time correlation of individual element data is simple. RSAS elements generate 50 word Short Period (SP) or Broad Band (BB) frames. Three axis elements generate 3 SP frames/sec, one for each axis. Formats and data definitions for the 2 frame types are given in the article below.

SP Frame Format

15	14	13	12	11	10	09	08	07	06	05	04	03	02	01	00
FRAME SYNC WORD 1 (F325 HEX)															
FRAME SYNC WORD 2 (0CDA HEX)															
0	TIME WORD 1														15
2															2
16	TIME WORD 1				23	07	CHANNEL STATUS (CS)						0		
2					2	2							2		
40 WORDS OF SHORT PERIOD DATA															
CHANNEL SOH															
15	COMMAND														0
2															2
COMMAND	AID		TIME WORD 2												
19	16	03	0	27	26	25	24	19	18	17	16				
2	2	2	2	2	2	2	2	2	2	2	2				
15	TIME WORD 2														00
2															2
CID								FA HEX							
6 BITS UNDEFINED (*)						10 BIT AUTHENTICATION NUMBER									

* The upper 6 bits of any authentication word must be set to 0 before authentication comparison is performed.

SP frame channel status format

Each Z, E or N SP frame contains one Channel Status (CS) byte containing digital status for the axis as defined in the table below.

<u>Bit</u>	<u>Function</u>
0	unused
1	CAL flag
2	Clip flag
3	mass motor busy
4	period motor busy
5	mass position motor busy
6	motor direction
7	unused

SP, BB frame channel, frame ID (CID) format

Each SP or BB frame CID byte contains a 6-bit channel and a 2-bit frame type identification field as shown below. The CID byte is a constant programmed by a strap port in each element. For SP and BB elements only 1 CID byte is required. A TSP element generates 3 CID bytes and the strap value will be assigned to the Z axis SP frame. The element processor will add 40 hex or 80 hex to the Z axis CHANNEL ID for the N and E axis SP frame CID byte, respectively.

SP, BB frame time word formats

A 28-bit frame count incremented once per second and used for authentication variable selection by the element processor is the source of TIME WORD 1 and 2 for all SP and BB frames. The integrity of the 24 most significant bits of frame count is supported by three 8-bit ports which have battery backup for power. TIME WORD 1 contains bits $2^{**}0$ through $2^{**}23$ of frame count in reverse order. TIME WORD 2 contains frame count bits $2^{**}27$ through $2^{**}24$ and bits $2^{**}19$ through $2^{**}0$.

Seismic data format

The least significant 14 bits of any seismic data word are the digitized representation of the sensor analog data signal and the 1 most significant bits of the word are encoded by the element processor to indicate the GAIN SELECT value as follows:

BIT 15 14

0	0	GAIN SELECT = 128
0	1	GAIN SELECT = 32
1	0	GAIN SELECT = 8
1	1	GAIN SELECT = 1

BB frame format

15	14	13	12	11	10	09	08	07	06	05	04	03	02	01	00
FRAME SYNC WORD 1 (F325 HEX)															
FRAME SYNC WORD 2 (OCDA HEX)															
0	TIME WORD 1														15
2															2
16	TIME WORD 1				23	07	BB CHANNEL STATUS						0		
2					2	2							2		
10 WORDS OF IPZ DATA APPEARING IN ORDER COLLECTED															
10 WORDS OF IPN DATA APPEARING IN ORDER COLLECTED															
10 WORDS OF IPE DATA APPEARING IN ORDER COLLECTED															
LPZ DATA WORD															
LPN DATA WORD															
LPE DATA WORD															
GTSOH STATUS															
DH SOH STATUS WORD															
DH SOH STATUS WORD															
DH SOH STATUS WORD															
4 UNUSED WORDS, ALL = 0															
15	COMMAND														0
2															2
COMMAND	AID		TIME WORD 2												
19	16	03	0	27	26	25	24	19	18	17	16				
2	2	2	2	2	2	2	2	2	2	2	2				
15	TIME WORD 2														00
2															2
CID								FA HEX							
6 BITS UNDEFINED								10 BIT AUTHENTICATION NUMBER							

HUB status frame format

15	14	13	12	11	10	09	08	07	06	05	04	03	02	01	00	
FRAME SYNC WORD 1 = F325 HEX																
FRAME SYNC WORD 2 = OCDA HEX																
0		0		MASTER FRAME NUMBER												
GMT WORDS 1, 2, 3, 4, 5																
HUB ANALOG STATUS WORD 1 THRU 10																
HUB DIGITAL STATUS WORD																
PORT 1 STATUS BYTE									PORT 0 STATUS BYTE							
PORT 3 STATUS BYTE									PORT 2 STATUS BYTE							
PORT 5 STATUS BYTE									PORT 4 STATUS BYE							
PORT 7 STATUS BYTE									PORT 6 STATUS BYTE							
PORT 9 STATUS BYTE									PORT 8 STATUS BYTE							
PORT 11 STATUS BYTE									PORT 10 STATUS BYTE							
PORT 13 STATUS BYTE									PORT 12 STATUS BYTE							
PORT 15 STATUS BYTE									PORT 14 STATUS BYTE							
PORT 17 STATUS BYTE									PORT 16 STATUS BYTE							
PORT 19 STATUS BYTE									PORT 18 STATUS BYTE							
PORT 21 STATUS BYTE									PORT 20 STATUS BYTE							
PORT 23 STATUS BYTE									PORT 22 STATUS BYTE							
PORT 25 STATUS BYTE									PORT 24 STATUS BYTE							
GENERAL STATUS WORD																
UPLINK TIME POSITION WORD																
LAST HUB COMMAND WORD																
LAST COMMAND BYTE									LAST COMMAND ELEMENT							
13 WORDS OF MULTIPLEXED DIGITAL STATUS																
1 WORD, CONTENT UNDEFINED THIS WORD IS RESERVED FOR SCARS USE AND CANNOT BE USED BY HUB																

GMT TIME CODE INTERFACE

This interface consists of three 16-bit ports which provide time of year (GMT) to the millisecond which is inserted into HUB status frame GMT words 1 through 5. Format of each word is shown in the following.

GMT word formats

<u>Bit</u>	<u>Word 1</u>	<u>Word 2</u>	<u>Word 3</u>
0	Units of millisecc. 1	Units of sec. 1	Units of min. 1
1	Units of millisecc. 2	Units of sec. 2	Units of min. 2
2	Units of millisecc. 4	Units of sec. 4	Units of min. 4
3	Units of millisecc. 8	Units of sec. 8	Units of min. 8
4	Tens of millisecc. 1	Tens of sec. 1	Tens of min. 1
5	Tens of millisecc. 2	Tens of sec. 2	Tens of min. 2
6	Tens of millisecc. 4	Tens of sec. 4	Tens of min. 4
7	Tens of millisecc. 8	0	0
8	Hund. of millisecc. 1	0	0
9	Hund. of millisecc. 2	0	0
10	Hund. of millisecc. 4	0	0
11	Hund. of millisecc. 8	0	0
12	0	0	0
13	0	0	0
14	0	0	0
15	0	0	0

<u>Bit</u>	<u>Word 4</u>	<u>Word 5</u>
0	Units of hours 1	Units of days 1
1	Units of hours 2	Units of days 2
2	Units of hours 4	Units of days 4
3	Units of hours 8	Units of days 8
4	Tens of hours 1	Tens of days 1
5	Tens of hours 2	Tens of days 2
6	0	Tens of days 4
7	0	Tens of days 8
8	0	Hund. of days 1
9	0	Hund. of days 2
10	0	0
11	0	0
12	0	± 1 millisecond accuracy
13	0	± 5 millisecond accuracy
14	0	± 50 millisecond accuracy
15	0	± 500 millisecond accuracy

